NOVEL APPLICATIONS OF COMPRESSED SENSING TO MAGNETIC RESONANCE IMAGING & SPECTROSCOPY

by

SAIRAM GEETHANATH

Presented to the Faculty of the Graduate School of

The University of Texas at Arlington in Partial Fulfillment

of the Requirements

for the Degree of

DOCTOR OF PHILOSOPHY

THE UNIVERSITY OF TEXAS AT ARLINGTON

December 2011

ACKNOWLEDGEMENTS

My research and scientific thinking have been shaped by influences from a significant number of peers and tutors over the past three years. I would like to express my deepest gratitude to all of them. Firstly, I would like to thank my mentor Dr. Vikram D. Kodibagkar, who has given me the courage to accept ignorance and the determination to gain knowledge that would overcome that ignorance. I would like to express my sincere thanks to him for the freedom he gave me to pursue the research of my interest. His qualities of being a logical, passionate problem solver with diligence are motivations for me to pursue an academic career. I would also like to thank him and Dr. Matthew Lewis for the special journal club sessions that really helped me learn about magnetic resonance imaging. I would like to thank the members of my committee: Dr. Khosrow Behbehani, Dr. Ralph P. Mason, Dr. Matthew A. Lewis, Dr. Changho Choi and Dr. Roderick W. McColl for their valuable inputs and guidance during the course of the degree. I am hugely indebted to my previous lab mate, Dr. Praveen K. Gulaka, who has had a deep impact on my approach to scientific endeavors and set high standards in the lab for me to follow and accomplish. I would also like to thank other members of my lab, fellow biomedical engineering and radiological sciences graduate students and the research staff for providing me with a stimulating environment and an enjoyable experience. I am also extremely grateful to the administrative assistants at UTA & UTSW (BME& RDS) for their helpful nature and assistance. Most importantly, I would like to thank my wife, for her patience and inspiration, my parents for their unconditional support during these years and my friend Yogeesh for his humor on graduate student life and constant encouragement.

November 18, 2011

ABSTRACT

NOVEL APPLICATIONS OF COMPRESSED SENSING
TO MAGNETIC RESONANCE IMAGING
AND SPECTROSCOPY

Sairam Geethanath, Ph.D

The University of Texas at Arlington, 2011

Supervising Professor: Vikram D. Kodibagkar, Ph.D.

In this work, three novel applications of compressed sensing to MRI have been developed and implemented which accomplish reduction in acquisition time, thereby also enabling increased spatial and/or temporal resolution. The first application is for reducing the acquisition time of conventional ^{1}H magnetic resonance spectroscopic imaging (MRSI), which requires alongeracquisition time than conventional MRI. The implementation involved exploiting the inherent sparsity of the MRSI data in the wavelet domain by the use of Daubechies wavelet. This was demonstrated on an *in vitro* phantom, 6 healthy human brain MRSI data sets, 2 brain and prostate cancer data sets. The reconstructions were quantified by the use of the root-mean-square-error metric and subsequent statistical comparison of the metabolite intensities based on one-way ANOVA followed by Bonferroni's multiple comparison test. It was found that the

implementation resulted in statistically significant differences at an acceleration of 10X and was considered the limit of the implementation. The implementation showed no significant differences until 5X. This indicates that CS has a potential to reduce conventional MRSI acquisition time by ~80%. This reduction in time could be used to increase the spatial resolution of the scan or acquire harder-to-detect metabolites through increased averaging.

Dynamic contrast enhanced MRI (DCE-MRI) is a MRI method that involves serial acquisition of images before and after the injection of a contrast agent. Therefore, it requires both high spatial and temporal resolution. The second application aims at accomplishing these requirements through the use of CS and comparing it with the widely-used method of key-hole imaging with respect to the choice of sampling masks and acceleration. Three sampling masks were designed for both approaches and reconstructions were performed at 2X, 3X, 4X and 5X. A semi-automatic segmentation procedure was followed to obtain regions of well and poorly perfused tissue and the results were compared using the RMSE metric and a voxel-wise paired t-test. The results of these tests showed that CS based masks performed better as compared to their key-hole counterparts and the sampling mask based on data thresholding performed the best. However, the exact implementation of this mask is impractical but an approximate solution was implemented for accelerating 3D gradient echo imaging.

The third application that has been developed in this work relates to the acceleration of sweep imaging with Fourier transform (SWIFT) which is a novel MR method facilitating the visualization of short T_2 species, which can yield important information about certain tissuessuch as cartilage. In this project, CS was applied to a resolution phantom and 5 human knee data sets acquired using SWIFT based imaging and accelerated up to 5X. The errors of reconstruction were quantified by RMSE and it was found that reconstructions at 5X maintained fidelity. A semi-automatic segmentation procedure was followed to segment the ligaments and adjoining structures and the number of segmented voxels was compared for the full data

reconstruction and the accelerated cases. The 5X reconstruction showed a percentage difference of approximately 17% and was considered the limit of the implementation.

TABLE OF CONTENTS

ACKNOWLEDGEMENTS iii

ABSTRACT iv

LIST OF ILLUSTRATIONS xi

LIST OF TABLES xv

Chapter Page

1. GENERATION OF MAGNETIC RESONANCE IMAGES 1

1.1 Introduction 1

1.1.1 Principle of MRI 1

1.1.2 Types of relaxation times and contrast 2

1.2 MRI acquisition and reconstruction 4

1.2.1 Spatial encoding and slice selection using gradients 4

1.2.2 MR pulse sequence 6

1.2.3 Cartesian and non-Cartesian trajectories 11

1.2.4 Reconstruction of MRI data 13

1.2.5 Iterative reconstruction 15

2. COMPRESSED SENSING AND MRI 16

2.1 Introduction 16

2.1.1 Sparsity 16

2.1.2 CS: the idea 18

2.1.3 The L_0, L_1 and L_2 norms 19

2.2 Requirements for application of CS to MRI 20
2.2.1 Transform sparsity 20
2.2.2 Pseudo-random undersampling 21
2.2.3 Non-linear reconstruction 22
3. CS MRSI 24
3.1 MRSI 24
3.1.1 Introduction 24
3.1.2 Simplified clinical MRSI pulse sequence 25
3.1.3 Speed-up in MRSI acquisition 27
3.2 CS for MRSI 28
3.2.1 Utility of CS for MRSI 28
3.2.2 Requirements for implementation of CS MRSI 29
3.2.3 Sampling of MRSI data 29
3.3 Methods 30
3.3.1 MRSI data and undersampling 30
3.3.2 Reconstruction 31
3.3.3 Acceleration factors and error metrics 34
3.3.4 Post-processing of MRSI data 34
3.3.5 Statistical Analyses 36
3.4 Results 36
3.4.1 Phantom data 36
3.4.2 Normal brain data 40
3.4.3 Brain tumor and prostate cancer 40
3.4.4 Error quantification and statistics 49
3.5 Conclusions 55

4. CS DCE-MRI 58
4.1 DCE-MRI 58
4.1.1 Introduction 58
4.1.2 Significance of pharmacokinetic parameters 59
4.1.3 Role of spatial and temporal resolution in DCE-MRI 59
4.1.4 Techniques available to accelerate DCE-MRI 60
4.1.5 Keyhole imaging 60
4.2 CS for DCE-MRI 61
4.2.1 Feasibility of CS for DCE-MRI 61
4.3 Methods 62
4.3.1 Key-hole methods 62
4.3.2 CS methods 64
4.3.3 Segmentation of region(s) of interest (ROI) 65
4.3.4 Pharmacokinetic analyses 65
4.3.5 Statistical analyses 66
4.3.6 Prospective study 67
4.4 Results 69
4.4.1 Data quality of reconstructions 69
4.4.2 Pharmacokinetic and statistical analyses 73
4.4.3 Prospective study 77
4.5 Conclusions 81

5. CS SWIFT 83
5.1 SWIFT-MRI 83
5.1.1 Introduction 83
5.1.2 SWIFT pulse sequence and reconstruction 84
5.2 CS for SWIFT MRI 86

5.2.1 Feasibility of CS for SWIFT MRI 86
5.2.2 CS SWIFT MRI reconstruction 86
5.3 Methods 87
5.4 Results 89
5.4.1 Resolution phantom 89
5.4.2 *In vivo* knee data 94
5.4.3 Error quantification 100
5.4.4 Volume segmentation 101
5.5 Conclusions 103

6. CONCLUSIONS AND RECOMMENDATIONS 104
6.1. CS MRSI 104
6.2. CS DCE-MRI 106
6.3 CS SWIFT 107

APPENDIX

A. TOP LEVEL MATLAB SCRIPTS FOR THE THREE PROJECTS 109
B. WAVELET ANALYSES 120
C. LIST OF PUBLICATIONS AND CONFERENCE ABSTRACTS 123

REFERENCES 126
BIOGRAPHICAL INFORMATION 133

LIST OF ILLUSTRATIONS

Figure Page

1.1 Time evolution of M_0 under the influence of (a) T_1 and (b) T_2 relaxations 3

1.2 Cartoon depicting the process of spatial encoding in a simplified 2D MRI experiment 5

1.3 Cartoon depicting a simplified spin-echo pulse sequence 8

1.4 Cartoon depicting a simplified gradient recalled echo pulse sequence 9

1.5 Acquisition of a line of k-space in a SE sequence. 10

1.6 Three k-space trajectories 13

2.1 Transform sparsity… 18

2.2 Random sampling …..... 22

2.3 Nonlinear reconstruction..... 23

3.1 A volume selective 2D PRESS based MRSI pulse sequence 26

3.2 Metabolites present in the GE braino phantom 30

3.3 Cartoon depicting the workflow of the reconstruction for CS MRSI implementation 33

3.4 Screen capture of the QUEST fitting in jMRUI for a voxel from the normal brain data 35

3.5 Reconstruction of the data grid for the braino phantom for the acceleration factors of 1, 2, 5 and 10 37

3.6 Spectra from 2 selected voxels (red and green voxels from figure 1) for the braino MRSI phantom data set for the acceleration factors of 1, 2, 5 and 10X. 38

3.7 Comparative metabolite maps of NAA, Cr, Cho, Lac and CNI
for a normal brain data set for the acceleration factors of
1, 2, 3, 4, 5 and 10X 39

3.8 Reconstruction of the data grid for a representative brain
MRSI data set for the acceleration factors of 1, 2, 5 and 10. 41

3.9 Spectra from 2 selected voxels (red and green voxels from figure 1)
for a representative brain MRSI data set for the
acceleration factors of 1, 2, 5 and 10X. 42

3.10 Comparative metabolite maps of NAA, Cr, Cho and CNI
for a normal brain data set for the acceleration factors of 1, 2, 5 and 10X. 43

3.11 Reconstruction of the data grid for a representative brain cancer
MRSI data set for the acceleration factors of 1, 2, 3, 4, 5 and 10X. 44

3.12 Reconstruction of the data grid for a representative prostate cancer
MRSI data set for the acceleration factors of 1, 2, 3, 4, 5 and 10X 45

3.13 Spectra from 2 selected voxels for representative
(a) brain tumor and (b) prostate cancer MRSI data set
for the acceleration factors of 1, 2, 5 and 10X 46

3.14 Comparative metabolite and ratio maps for
(a) brain tumor (NAA, Cr, Cho) and (b) prostate cancer (Cit, Cr, Cho)
MRSI data set for the acceleration factors of 1, 2, 5 and 10X. 47

3.15 Graph of Root mean square error (RMSE) values for the different
MRSI data for the acceleration factors of 2, 3, 4, 5 and 10X in comparison
with the original data (1X) 50

4.1 Representation of the sampling masks used for acceleration.
White pixels represent a sampled location and black pixels
represent an un-sampled location.. 63

4.2 Image segmentation for a representative data set. 66

4.3 Undersampling mask used for the
modified ge3d sequence implemented on the Varian 4.7T scanner. 68

4.4 Reconstruction of DCE data sets using the 6 acceleration
approaches described. 70

4.5 A new, image-based representation of RMSE values for
the 6 acceleration approaches described. 71

4.6 Calculated K^{trans} maps using the data reconstructed
from the six acceleration approaches described. 74

4.7 Calculated v_e maps using the data reconstructed
from the six acceleration approaches described.. 75

4.8 (a) The minimum energy reconstruction resulting from the undersampling scheme employed in the current study and (b) the results of the iterative reconstruction for the central slices in the 3 orientations. 78

4.9 Time-course of the experiment depicted by the temporal frames of the central slice at baseline (frame 5), immediately post-contrast (frames 6,7, 8), an intermediate time point (frame 20) and the last time point (frame 65).. 79

4.10 (a) The result of the segmentation procedure on the central slice showing the muscle (green), well-perfused (orange) and poorly-perfused (red) regions. (b) Intensity-time course for the three regions as a function of the temporal frames 80

5.1 Cartoon depicting the (a) SWIFT pulse sequence, (b) magnified RF pulse and (c) closer look at the individual pulses to show the dwell time (dw) 84

5.2 The resulting k-space trajectory of the shown SWIFT pulse sequence 85

5.3 Photograph of the resolution phantom used in the project 88

5.4 Segmentation procedure (a) ROI drawn on the center sagittal slice shown in orange overlay on the MRI (b) the resulting segmentation on the corresponding slice. 89

5.5 Line intensity profile of a symmetrical feature in the resolution phantom shown in the top panel (a) the zfwdc images for the accelerations shown and (b) the corresponding reconstructions and the plot of line intensities adjacent to the images. 91

5.6 Slices through the center of the resolution phantom as seen in coronal orientation 92

5.7 Slices through the center of the resolution phantom as seen in axial orientation 93

5.8 Slices through the center of the resolution phantom as seen in sagittal orientation 94

5.9 Line intensity profile of a symmetrical feature in the representative knee data shown in the top panel (a) the zfwdc images for the accelerations shown and (b) the corresponding reconstructions and the plot of line intensities adjacent to the images. 95

5.10 Slices through the center of the representative human knee (with each slice separated from the other by 3 slices) as seen in coronal orientation 96

5.11 Slices through the center of the representative human knee (with each slice separated from the other by 3 slices) as seen in sagittal orientation 97

5.12 Slices through the center of the representative human knee (with each slice separated from the other by 3 slices) as seen in axial orientation 98

5.13 (a) Sagittal view of the center slice of the representative data set showing the ligaments (b) Magnified images at 1, 2, 3, 4, and 5X for the area showed by the red box in (a) 99

5.14 RMSE values for the reconstructions of phantom and knee data sets over acceleration factors of 2, 3, 4 and 5X as compared to 1X 100

5.15 Segmentation results (a) Number of segmented voxels for each data set in comparison with the corresponding accelerated reconstructions (b) The pooled resulting difference in percentages for all the 5 data sets for the 4 acceleration factors with respect to the original data. 102

LIST OF TABLES

Table Page

3.1 Acquisition parameters for the MRSI data 31

3.2 Mean metabolite intensities (arbitrary units) and ratios (± standard deviation) for the pooled voxel data for four data types. 48

3.3 P-values resulting from the one-way ANOVA followed by Bonferroni's comparison test forthe *in vitro* phantom. 51

3.4 P-values resulting from the one-way ANOVA followed by Bonferroni's comparison test for thehealthy brain MRSI data. 52

3.5 P-values resulting from the one-way ANOVA followed by Bonferroni's comparison test forthe brain cancer MRSI data. 53

3.6 P-values resulting from the one-way ANOVA followed by Bonferroni's comparison test for prostate cancer MRSI data. 54

4.1 Comparisons of the K^{trans} maps between the six reconstruction methods at 4 different undersampling factors with the maps obtained using complete k-space reconstruction. 76

4.2 Comparisons of the v_e maps between the six reconstruction methods at 4 different undersampling factors with the maps obtained using complete k-space reconstruction. 77

CHAPTER 1

GENERATION OF MAGNETIC RESONANCE IMAGES

1.1 Introduction

Magnetic resonance imaging (MRI) is a widely used modality to obtain structural, functional and metabolic information about the physiology of interest. Various methods have been developed in MRI such as MR spectroscopic imaging, diffusion tensor imaging, etc. which are sensitive to certain aspect(s) of biological processes that yield complimentary information aiding in prognosis and diagnosis of pathology (1).

1.1.1 Principle of MRI

MRI measures the magnetization associated with an ensemble of 'spins' of a chosen nucleus in a volume under investigation. The nucleus most commonly looked at it is the water proton due to high concentration of water in the human body. A typical MRI experiment involves the perturbing of the magnetization that is aligned along a static magnetic field by the application of a radio-frequency (RF) field perpendicular to the static magnetic field (say, along the longitudinal direction). This causes the magnetization to spiral downward while precessing around the static field and results in a transverse component, which is critical for signal detection. The signal in a MRI experiment is produced through the electromotive force (emf) associated with the precessing magnetization of the nucleus under investigation, which is detected using a stationary radio-frequency coil using concepts from Faraday's laws of induction. Images of magnetization are produced by using magnetic gradients, which can then

be used to spatially encode the net magnetization in a volume. This spatial encoding is performed by modulating the frequency and phase of the spins in a manner such that each pixel in the resulting data has a unique frequency and phase combination that can later be deciphered using Fourier transform of suitable dimensionality. Thus, MR images are generated.

1.1.2 Types of relaxation times and contrast

1.1.2.1 Laboratory and rotating reference frames

Two reference frames are typically used to describe the magnetic resonance phenomenon in a vector representation: i) the laboratory reference frame ii) rotating reference frame. The laboratory reference frame is described with respect to the scanner axes. However, the rotating reference frame by convention assumes the z-axis to be along the direction of the static magnetic field (B_0). This reference frame is relative to the difference of the frequencies of the spin packetswith respect to the Larmor frequency of the nucleus. These co-ordinate systems follow the right hand rule and aid in the understanding of the time evolution of magnetization due to external fields, relaxation times and diffusion. This phenomenon is mathematically described by a set of equations called Bloch equations (2).

1.1.2.2 T_1, T_2 and T_2

At equilibrium the net magnetization is along the direction of the B_0 (assumed to be in the longitudinal direction) and is called the equilibrium magnetization (M_0) and hence at this time, there are no transverse magnetization components (M_T). This equilibrium can be disturbed by depositing energy equal to the energy difference between the spin states at the precession frequency of the spins. This can reduce the net longitudinal magnetization (M_L) to zero. The time constant with which the longitudinal magnetization recovers to its equilibrium value through

spin lattice relaxation is known as T_1 as described in equation [1.1] and the time dynamics of this process is shown in figure 1.1(a).

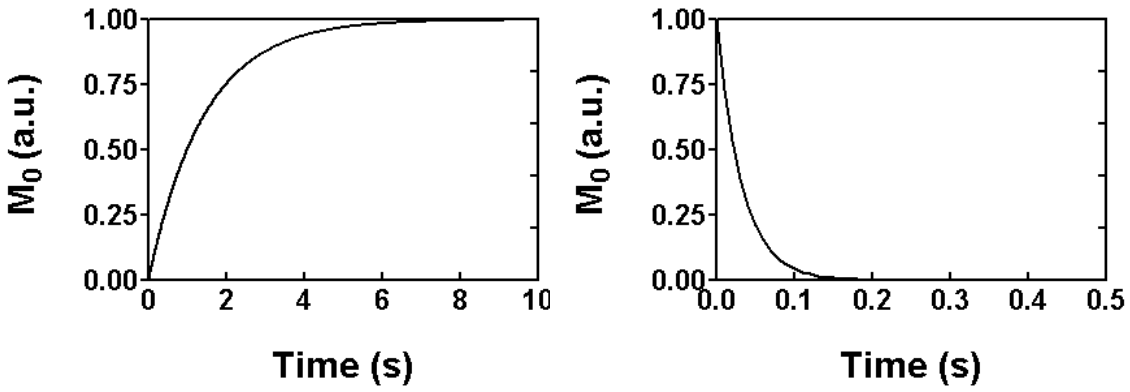

(a) (b)

Figure 1.1 Time evolution of M_0 under the influence of (a) T_1 and (b) T_2 relaxations (for muscle at 3.0T (3))

$$M_L = M_0\left(1 - e^{-t/T_1}\right) \qquad [1.1]$$

The transverse component of the magnetization present post-excitation (M_{T0}) starts to dephase due to different spin pockets precessing at slightly different precession frequencies. This difference is frequencies result in phase difference accumulation over time. The time constant that describes the return of the transverse magnetization to equilibrium is called T_2, which is called spin-spin relaxation time mathematically expressed as [1.2]. The decay is depicted in figure 1.1(b).

$$M_T = M_{T0}\left(e^{-t/T_2}\right) \qquad [1.2]$$

The decay of the transverse magnetization can be contributed mainly due to the molecular interactions (characterized by T_2) and the inhomogeneity in the static magnetic field

(characterized by say, T_2'). The combined effect of these two phenomena result in a relaxation time called "apparent T_2" or T_2^* and are related as shown below

$$\frac{1}{T_2^*} = \frac{1}{T_2} + \frac{1}{T_2'} \qquad [1.3]$$

Based on the type of relaxation mechanism that one desires to visualize i.e. spin-lattice, spin-spin only or spin-spin and inhomogeneity, the contrast of the MR image correspondingly is said to be T_1, T_2 and T_2^* weighted.

1.2 MRI acquisition and reconstruction

A typical present day MRI scan involves the usage of magnetic field gradients to encode spatial information as alluded to in section 1.1.1. The acquisition process is followed by the reconstruction of the encoded information to images depicting localized intensities of magnetization.

1.2.1 Spatial encoding and slice selection using gradients

An MR imaging gradient is a magnetic field of varying strength relative to position. A gradient that is used to achieve excitation of a particular plane is applied concurrently with an excitation RF pulse. The RF pulse tips the magnetization in the volume whose location and thickness are determined by the gradient strength and the RF pulse bandwidth. Since this chosen plane represents the slice of imaging, the gradient is called the slice select gradient. Figure 1.2(a) represents the slice selection in a simple 2D MRI experiment. The triangle represents the gradient with the increase in the shade corresponding to increasing magnetic field. The excited slice is shown by the red slab. The goal in using a position dependent magnetic field gradient is to be able to encode each voxel of spins with a unique combination of frequency and phase. To encode 2 dimensional (2D) information, a gradient along each dimension is required. To demonstrate the process of encoding, the cartoon in figure 1.2(b) depicts 4 voxels with spins along the direction of B_0. One of the gradients causes a small

variation in precession frequency of the spins along the direction it is applied (figure 1.2(c)). The second gradient applied in the other direction adds a linear phase variation to the spins along the second direction to the already existing frequency variation along the first direction (figure 1.2(d)). Hence every voxel is characterized by unique frequency and phase combination and the corresponding gradients called frequency encoding gradients and phase encoding gradients.The matrix of the resulting MR signals for the different combinations of phase and frequency is called the k-space.

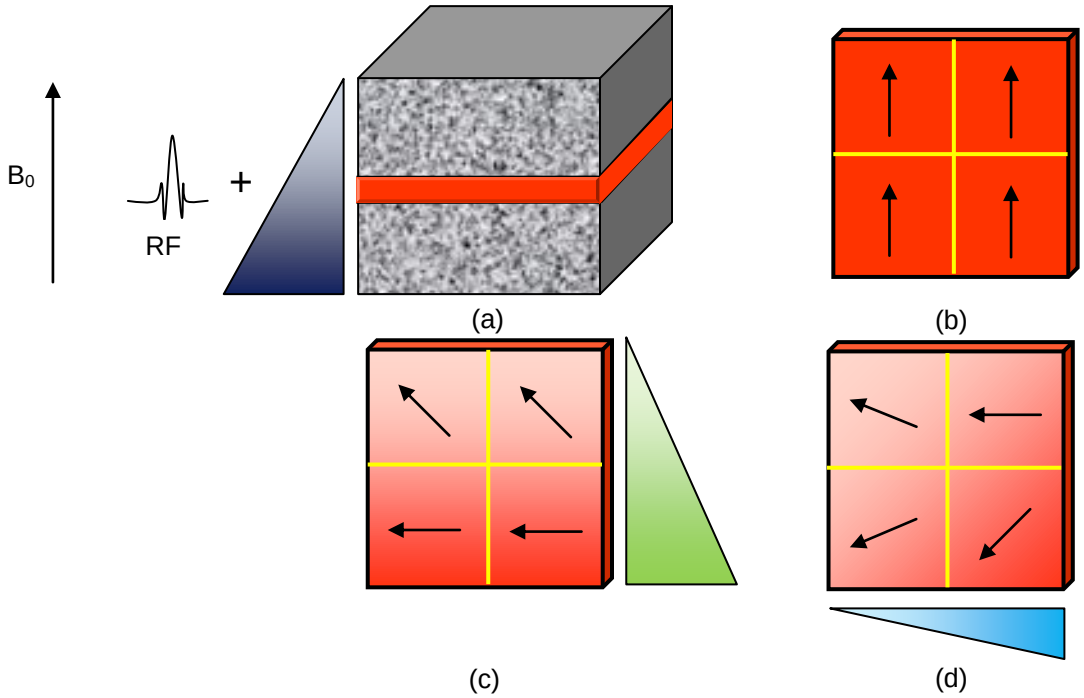

Figure 1.2 Cartoon depicting the process of spatial encoding in a simplified 2D MRI experiment (a) slice selection (b) selected slice with 4 spin pockets (c) effect of first gradient and (d) the second gradient

1.2.2 MR pulse sequence

The process of acquiring the magnetization profile of the chosen volume of interest is achieved through the application of excitation RF pulses, gradients and the recording of the resulting MR signal using analog to digital converters (ADC). The time sequence of playing out these components to achieve imaging of the desired volume along with a chosen contrast scheme is called a MR pulse sequence.A typical spin-echo pulse sequence records the echo formed due to the rephasing of the spins due to a sequence of 90_x - τ - 180_y RF pulses where τ is the inter-pulse delay (90_x represents a 90^o RF pulse played along the x-axis). A simplified cartoon of such a sequence is shown in figure 1.3. The sequence begins with a 90_x RF pulse excitation played along with a slice select gradient (G_{SS}) to excite the volume of interest. The RF pulse flips the spins from longitudinal axis to the transverse plane. A phase encode gradient (G_{PE}) of a certain magnetic field strength is applied to encode the voxels in one direction along with a frequency gradient (G_{RO}) to encode in the other direction. During this time, the spins in each voxel undergo a M_T decay due to T_2^* phenomenon. The signal generated at this time is shown on the signal axis in figure 1.3. The signal is called free induction decay (FID). At the end of time τ, a 180_y RF pulse is applied which flips the spins by 180^o around the axis (y-axis in this example) which is applied (the direction of precession does not change) to produce an echo due to the rephasing of the spins at time 2τ.

The frequency gradient that is twice the strength of the frequency gradient applied after the 90_x is turned on during the formation of the echo. Simultaneously, the ADC is turned on to read-out the formed echo due to record a line of k-space. Since the frequency encode gradient is turned on during the reading out process, it is also called read-out gradient. The time taken to form the echo is called the echo time (T_E). The time between 2 consecutive acquisition read-outs for the same volume or slice is called repetition time (T_R). The k-space interpretation can be visualized in figure 1.5(a). For a chosen value of PE gradient (0 in the figure 1.5(a)), the k-space traversal begins at the center (position 1 in figure 1.5(a)) and the application of the RO

gradient traverses to the end of the k_x-axis (position 2). However, during this time the FID is not recorded. The 180^0 RF pulse then flips the spins and also the point in k-space, which is now at the start of the kx-axis (position 3). The RO gradient of twice the strength of the initial RO gradient is applied at the appropriate time of echo formation. During this time the k-space is traversed from position 3 to position 4 while the echo is also recorded using the ADC.

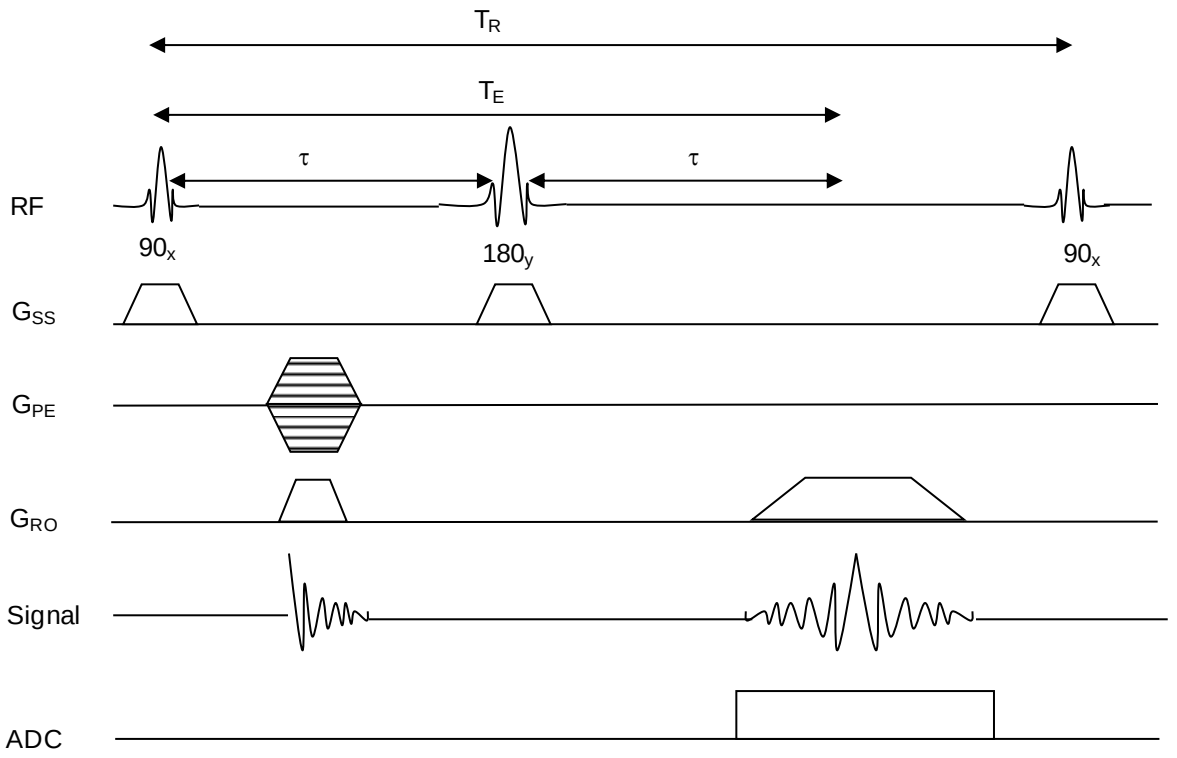

Figure 1.3 Cartoon depicting a simplified spin-echo pulse sequence

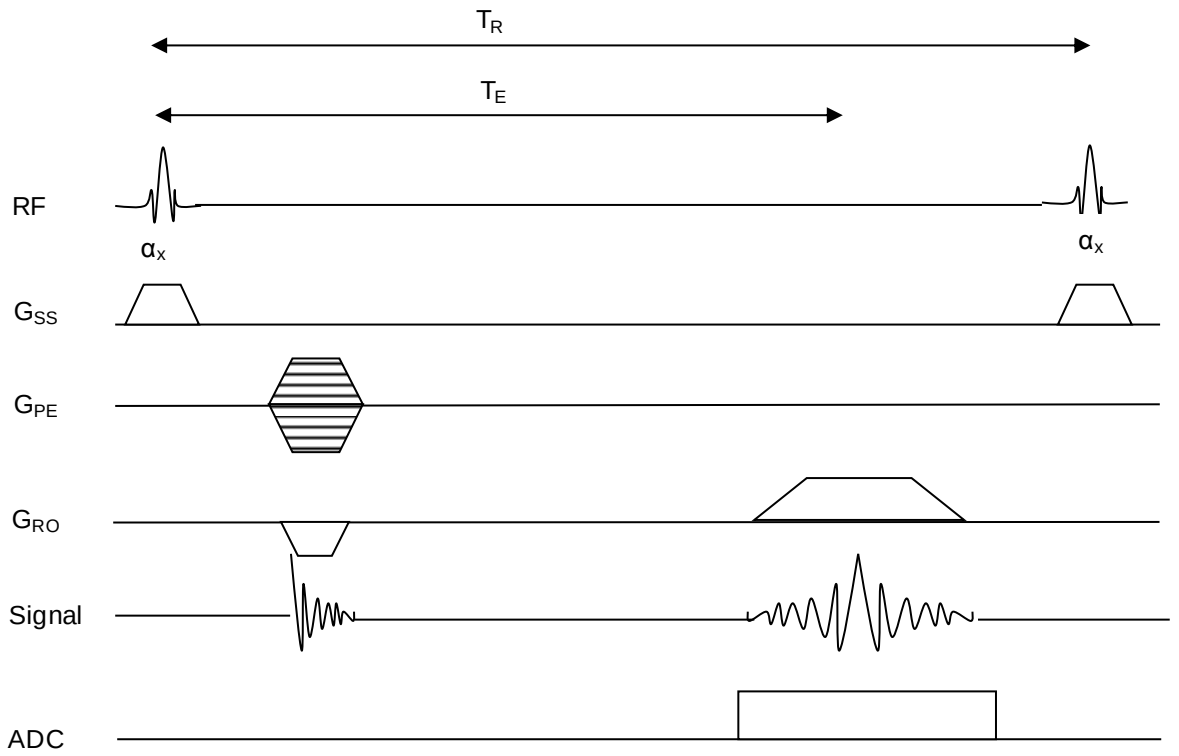

Figure 1.4 Cartoon depicting a simplified gradient recalled echo pulse sequence

The other mechanism for echo formation is known as the gradient echo or gradient recalled echo (GRE) pulse sequence where a gradient with opposite polarities is used to dephase and then rephase the spins to obtain an echo like the 90-180 RF pulse combination in case of a SE. The k-space traversal can be traced similar to the SE case and is shown in figure 1.5 (b) with the difference that the gradient reversal causes the trajectory to move from position 2 to position 3 during the read-out and hence avoids the extra step required in SE.

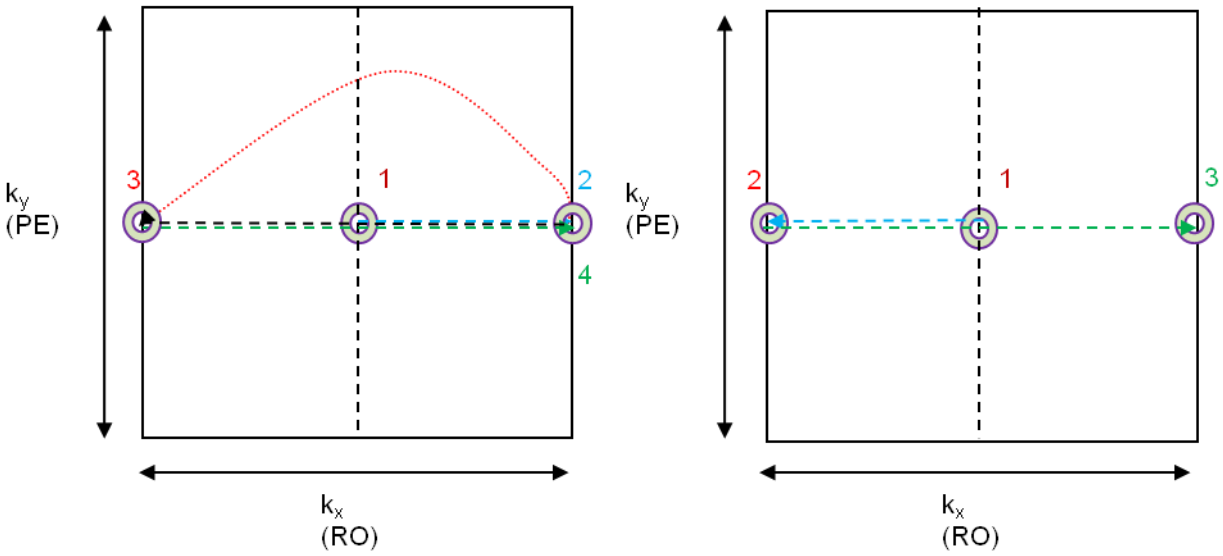

Figure 1.5 (a) Acquisition of a line of k-space in a SE sequence. 1) Before the application of gradients 2) After the application of PE gradient of value 0 and RO gradient after the 90_X 3) The 180_Y pulse flips the spins and the k-space is 'rewinded' 4) The RO gradient is applied with twice the strength of the first to traverse the span of k_x
(b) Acquisition of a line of k-space in a GRE sequence. 1) Before the application of gradients 2) After the application of PE gradient of value 0 and RO gradient after the α_x3) The RO gradient is applied with twice the strength of the first to traverse the span of k_x

Hence a GRE sequence needs only 1 RF pulse (for excitation only) of an arbitrary angle (α) as shown in figure 1.4. Since a GRE sequence does not require 2 pulses to form the echo separated by τ, the resulting T_R is very short and hence this sequence is ideal for T_1 weighted imaging. On the other hand, a SE sequence by design requires longer T_R and hence is more suited to T_2 weighted imaging. GRE has a lower specific absorption rate as compared to SE due to the use of a single and typically lower flip angle pulse but is more sensitive to field inhomogeneities.

1.2.3 Cartesian and non-Cartesian trajectories

The time-course of filling up the lines in k-space is called the k-space trajectory. The simplest and the most commonly used trajectory is the Cartesian trajectory (figure 1.6 (a)) where lines of k-space are collected in a raster-scan method like the pulse sequences shown above in figures 1.3 and 1.4. This method is robust in data collection while also simplifying image reconstruction, as it requires the use of conventional Fourier transforms(discussed in section 1.2.4).

However, there are certain medical imaging applications that require high spatial and/or temporal resolutions. Cartesian imaging does not provide the adequate solution to such necessities since it gathers the data with a uniform weighting throughout the Cartesian grid. The non-Cartesian approaches can be used to gain higher signal to noise ratio (SNR) since the sampling of the center of k-space typically determines the SNR. The density of k-space is however non-uniform as most of the information is typically contained in the low frequency components which are in the center of k-space rather than the high frequency components which lie towards the edges of the grid. This has given rise to research on non-Cartesian trajectories like radial (figure 1.6 (b)), spiral, variable density spiral (figure 1.6 (c)), stack of spirals, koosh-ball, etc. which exploit the variable density of k-space (4-6). The direction of the k-space traversal is shown with blue lines. This approach of utilizing trajectories suited to

the density of k-space aids in quicker sampling of the more important data points and hence reduces acquisition time (4-6). The reduction in acquisition time can be used to increase spatial and/or temporal resolution. These trajectories are also extensively used in case of MRI of other nuclei like Sodium which has a very quick T_2^* relaxation or to reduce motion artifacts.

The prospective implementation of the pulse sequences for these non-Cartesian trajectories often times require time-varying gradient forms which could allow for smoother transition between phase encode values but could also result in smearing artifacts across the acquired image (in case of a spiral). However, the reconstruction of non-Cartesian trajectory involves more computation when compared to the conventional acquisition due to density compensation (discussed in section 1.2.4) and the use of Fourier transforms. Therefore, MRI provides multiple options for acquisition strategies with respect to various parameters such as T_R, T_E, flip angle while also aiding in tailoring it to particular applications through the use of the different k-space trajectories and optimize it to the requirement of SNR, acquisition time and ease of implementation.

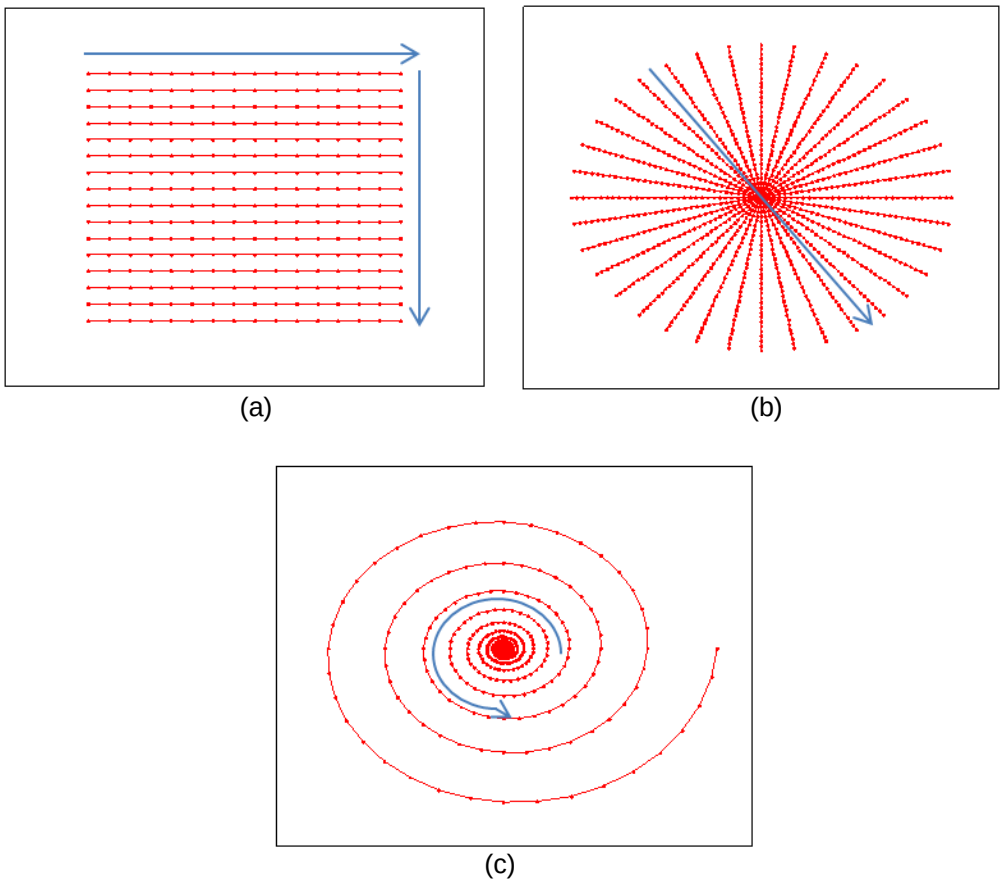

Figure 1.6 Three k-space trajectories: (a) Cartesian (b) Radial (c) Variable density spiral with increased sampling in the center with the blue lines showing the direction of the traversal.

1.2.4 Reconstruction of MRI data

The data or k-space, collected from a MR scanner for a 2D experiment is a matrix of the size M X N where M and N are number of elements in each of the two directions. The result of the spatial encoding using 2 gradients results in a matrix, which represents a unique frequency and phase combination. This matrix represents the result of 2D spatial discrete Fourier transform (DFT). Hence it is very convenient to reconstruct the image by using a 2D inverse

DFT (7). The forward (analysis equation) [4a] and inverse (synthesis equation) DFT [4b] pair is mathematically described below:

$$F(k,l) = \frac{1}{\sqrt{MN}} \sum_{n=0}^{N-1} \sum_{m=0}^{M-1} f(m,n)\, e^{-j\,2\pi\left(\frac{mk}{M}+\frac{nl}{N}\right)} \qquad [1.4a]$$

$$f(m,n) = \frac{1}{\sqrt{MN}} \sum_{l=0}^{N-1} \sum_{k=0}^{M-1} F(k,l)\, e^{j\,2\pi\left(\frac{mk}{M}+\frac{nl}{N}\right)} \qquad [1.4b]$$

$$(0 \le m,k \le M-1, \qquad 0 \le n,l \le N-1)$$

where,

M, N are the number of pixels in corresponding directions

$F(k,l)$*is the 2D DFT of* $f(m,n)$

This approach is suitable for acquisition with a Cartesian trajectory. However, it cannot be applied to data acquired on a non-Cartesian grid. Two major approaches exist to reconstruct data of this nature. The first approach consists of gridding the non-Cartesian trajectory onto a Cartesian grid followed by the conventional DFT approach (8). This method involves compensating for the increased sampling density in the center resulting from the trajectories to ensure uniform weighting of data samples on the Cartesian grid (9). The output of this process is dependent on the convolution kernel chosen for gridding and the k-space trajectory. The other method involves using a modified Fourier transform called the non-uniform Fourier transform (NUFT) which evaluates the transform at the co-ordinate of the k-space trajectory as opposed to following the gridding approach described above (10). The NUFT approach is more computationally intensive but can aid in removal of certain artifacts due to gridding. For some specific case of radial sampling, a well-studied reconstruction approach in computed tomography called backprojection imaging can be employed.

1.2.5 Iterative reconstruction

MR reconstruction approaches also include iterative methods using one or more of the above 3 methods to optimize a certain reconstruction with desired criteria such as obtaining an image with reduced streak artifacts for an undersampled data acquisition (11) or iterative local area phase estimation to improve quality of MR images from undersampled data (12). These reconstructions are typically cast as problems of convex optimization and the value of a desired criterion or the error produced due to the lack of conforming to the criterion is evaluated at each step. This value provides a feedback for the algorithm to decide on the direction of the next step, which would reduce the error or increase the desired criterion. The reconstruction is stopped when the criterion value converges i.e. the difference between successive criterion values is less than or equal to a pre-defined tolerance range. An example of such a reconstruction approach is shown in ref. (13) where the tools of NUFT and iterative reconstruction have been used to achieve better quality reconstructions in the presence of field inhomogeneity. Such approaches can be computationally intensive if the reconstruction involves the use of a non-Cartesian trajectory due to the gridding and regridding (or NUFT) approach that has to be used iteratively.

CHAPTER 2

COMPRESSED SENSING AND MRI

2.1 Introduction

MRI provides images with excellent contrast and can be used to image detailed structure, function and metabolism of the organ of interest. However, the reduction of acquisition time of MRI is an ongoing challenge in the field to enable imaging of certain biological processes that demand high spatial and/or spectral resolutions. To this end, techniques like parallel imaging(14) and other undersampling strategies have been innovated. These techniques are however mostly governed by the Nyquist sampling rate and hence cannot yield acceleration beyond the Nyquist limit due to the resulting aliasing artifacts. A recently developed mathematical framework called compressed sensing (CS) provides for reconstruction of data from highly undersampled measurements (15-16). This has been used in MRI to gain acceleration in acquisition time and has been demonstrated on some MRI methods. Compressed sensing has also been recently used in clinical applications for pediatric imaging where reduction in acquisition time is critical for diagnosis (17).

2.1.1. Sparsity

A vector that has a significant majority of its coefficients equal to zero and a few coefficients that contain all the information is said to be ‘sparse’. In cases where a large number of these coefficients are exactly zeros, the sparsity is said to be ‘strong’. However, in most practical situations there exists a transition band from the few high valued coefficients to the many zero valued coefficients. This case is called ‘weak sparsity’ and is more commonly

encountered. From a signal processing standpoint, a sparse signal has most of its energy contained in a few measurements while the rest of the measurements are zero or negligible.

2.1.1.1 Transform sparsity and compression

A vector, which becomes sparse upon the use of a mathematical transform is said to exhibit transform sparsity. For example, a voltage depicting a sinusoidal characteristic of a particular frequency when recorded over time does not exhibit sparsity. However, on the use of Fourier transform, the transformed vector has all of its information in 2 peaks. Now the sine wave is said to be sparse in the Fourier domain. Most MR images are sparse in some transform domain. Angiography images are sparse in the finite differences domain and cardiac cine images are sparse in the spatio-temporal Fourier domain.

Sparsity also extends to compressibility where retention of only the important coefficients could be used for reconstruction of the original signal. The number of coefficients to be used to reconstruct is decided by a threshold typically applied in the region where there is a sharp decrease in the amplitude of the coefficients when they are sorted in a descending fashion. The threshold indicates the cut-off for the important coefficients from the less important ones (analogous to the cut-off frequency for impulse response filters in signal processing). A general mathematical tool that has been used to compress images is the wavelet transform. An image is said to be compressed with no losses if the reconstruction from the sparse coefficients is exact i.e. the difference between the original and reconstructed images from compressed data is zero. If this is not the case, the compression is said to be ‘lossy’. Lossy compression results in reconstruction similar to the original but cannot recover some information that is typically not perceivable to the human eye. This information corresponds to the coefficients closer to the zeros and is not used for reconstruction. This is applicable to MR images as well. However, it should be noted that lossy compression in certain medical imaging applications involving detection problems might not be tolerable and have to be evaluated by radiologists.

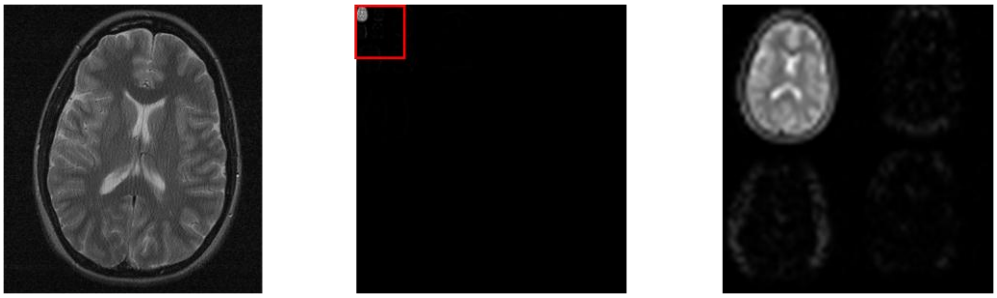

(a) (b) (c)

Figure 2.1 Transform sparsity: (a) A 2D MR image of the human brain (b) Representation of the object in 2D Daubechies wavelet transform domain (c) A magnified view of the wavelet coefficients shown in the red square in (b)

2.1.2. CS: the idea

Conventionally, the compression of images is performed *after* the acquisition of the entire image. This involves wavelet transforming the image and thresholding the important coefficients for storage. This is typically done to accomplish saving in data storage and also to facilitate the transfer of such data. Therefore, the saved data consists of the most important coefficients, which enable near-perfect reconstruction of the original data.

The philosophy of CS is to be able to compress and acquire only these important coefficients of the signal during the acquisition by using the concept of transform sparsity. The implementation of an ideal CS solution is given by the answer to a simple question: What is the minimum number of coefficients required to acquire data with acceptable SNR and high data fidelity to represent the object of interest?

2.1.3. The L_0, L_1 and L_2 norms

The question above can be mathematically cast as an optimization problem. The first half of the question is to solve for the minimum number of coefficients in the transform domain required. The 'norm' function in linear algebra can be used to evaluate this criterion. The L_p-norm of a vector *x* of length *n* is given by the equation [2.1].

$$||x||_p = \left(\sum_{i=1}^{n} |x_i|^p\right)^{1/p} \qquad [2.1]$$

When p=0, it is called the L_0 norm which simplifies to the number of non-zero elements in the vector (*n* in the case of a vector consisting of ones) which is the required solution. However, this norm needs to make the mathematically improper assumption that $0^0=0$. The L_0 norm is not convex in nature, computationally intractable and results in difficulty in its usage in optimization problems (18). However, L_0 based CS reconstruction has been reported recently which involve non-convex optimization schemes (19). Mathematically, solution to a convex problem is more stable than a non-convex optimization scheme due to reliability in convergence. Hence, the next integer (p =1) norm L_1 is generally used which is the closest convex approximation for L_0 norm and provides the absolute sum of the elements of the vector. It must be also mentioned that reconstructions using $L_{1/2}$and other non-integer norms utilized in a non-convex framework have also been explored recently (20). The L_1 norm penalizes the presence of a large number of components which ensures sparsity. In other words, L_1 norm prefers the presence of a few coefficients which contain the total energy of the signal. The second part of the question is to ensure data fidelity. The L_2 norm is an ideal tool for ensuring consistency since the norm penalizes small errors less and the large errors more significantly due to the quadratic nature of the norm. Hence the solution consists of a L_1 norm of the transform coefficients to ensure

sparsity and L_2 norm of the measured data and its iterative approximation to account for data consistency.

2.2 Requirements for application of CS to MRI

The implementation of CS to MRI is straightforward given that one has prior knowledge of the type of MR images one is going to acquire so that certain unique properties of that particular class of images can be utilized optimally. Practically, this is not a challenge as this information is always known. For instance, one always has the knowledge that images resulting from MR angiography (MRA) will also be sparse in its native representation. This provides an idea to the CS implementer about the utility of application of CS to that MR method. As mentioned before, MRA is sparser in the finite difference domain or the total variation (TV) norm.

2.2.1. Transform sparsity

The fundamentals of transform sparsity have been described in section 2.1.1.1. It is the one of the three most important requirements for the implementation of CS. However, the choice of the transform for exploiting sparsity existing in a particular class of MR images is not an easy task and is a field of ongoing research. Generally, 2D or 3D wavelets are used for this purpose as wavelets have been shown to result in good compression of medical images. On the other hand, the optimal solution is to explore the best transform sparsity for each particular case. Dynamic contrast enhancement MRI (DCE-MRI) is one such example where spatio-temporal correlations can be exploited to increase transform sparsity along with the use of wavelets. Therefore the transform sparsity requirement allows the CS implementer to evaluate the sparsity of the images and provides an insight into the number of samples he/she needs to acquire to achieve exact reconstruction. This is solely dependent on the number of sparse coefficients that are enough to result in an exact reconstruction.

2.2.2 Pseudo-random undersampling

MRI involves collecting of spatial frequency information called k-space as explained insection1.2. To apply CS to MRI, the k-space needs to be randomly undersampled to ensure that aliasing artifacts are not produced due to the non-prime nature of the vector size (theorem 1.1, (15)) as noticed in the case of sub-Nyquist sampling. A randomly undersampled k-space, as shown in figure 2.2, results in artifacts that are incoherent with the image and can be de-noised to obtain the original image. The number of samples required to be acquired is typically 5 – 8 times the number ofsparse coefficients of the data set (15). Hence, the sparser the transformed data, the fewer the samples required to reconstruct!There are two specific practical limitations and/or considerations for random undersampling of k-space. The first limitation is that pure random k-space sampling is difficult to achieve as this requires rapid switching of gradients and in most cases is impractical due to the resulting eddy current and related artifacts.

The second consideration arises due to the fact that most of the energy of the acquired data is located in the low frequency components. Hence a uniform weighting of the samples would result in reduced SNR. To overcome these limitations, variable density pseudo-random sampling schemes have been proposed and successfully implemented (21). The sampling mask consists of increased samples in the center while containing fewer samples in the edges. This alleviates the challenge of loss of SNR but requires optimal gradient design and new k-space trajectories to sample the chosen points in k-space. Another approach is to start from conventional k-space trajectories and introduce incoherent sampling within the same framework by skipping phase encode values as has also been demonstrated in (21) and in this work.

A major factor in the implementation of CS with regard to undersampling is the dimensionality of the data. MR images with higher dimensionality (3D or higher) provide better sparsity (similar to image compression) and hence yield better CS performance. In other words, CS technology is better suited to accelerate MR acquisitions involving higher dimensional data.

This is ideal as MR scans involving higher dimensional data are the ones which are the most time consuming.

(a) (b) (c)

Figure 2.2 Random sampling: (a) k-space of the brain image shown in figure *2.1(a)* (b) A sampling mask showing the sampling locations of the k-space as white pixels while the black pixels represent unsampled locations (c) The resulting minimum energy reconstruction demonstrates the resulting incoherent artifacts

2.2.3. Non-linear reconstruction

The constrained optimization problem put together in sections 2.2.1 and 2.2.2 can be described by the following equation (reproduced from ref. (16))

$$minimize||\psi m||_1$$

$$s.t.||F_u m - y||_2 < \varepsilon \qquad [2.2]$$

where, m is the desired image, y is the measured k-space data, ψ is the sparsifying transform and ε is the parameter for error tolerance. This equation can be recast as an unconstrained optimization problem using the Lagrange method as shown in equation [2.3]. Here, λ is the regularization parameter that needs to be chosen to balance the data consistency and sparsity terms. Equation [2.3] can be solved by the use of an iterative non-linear reconstruction method Among the various such methods available such as subspace pursuit,

steepest descent method, etc, the non-linear conjugate gradient has been well studied and applied.

Briefly, the non-linear conjugate gradient (NCG) calculates the direction of the gradient given by the differentiation of the above equation. At each step the length of the step to be taken in the gradient direction is given by a line-search parameter. The stopping criteria for the iterations are 2 fold: 1) the difference of values of the tolerance parameter between successive iterations is negligible and 2) the value of the tolerance parameter is smaller than the chosen εvalue. The precise number of iterations is problem dependent. The reconstructed image *m* obtained at the end of this process is the desired solution to equation [2.3].

$$argmin_m ||F_u m - y||_2^2 + \lambda||\psi m||_1 \qquad [2.3]$$

(a) (b) (c)

Figure 2.3 Nonlinear reconstruction: (a) k-space of the brain image shown in figure *2.1(a)* (b) A variable density sampling mask showing the sampling locations of the k-space with 33% sampling(c) The resulting image reconstructed iteratively using equation [2.3] implemented via NCG

CHAPTER 3

CS MRSI

Magnetic resonance spectroscopic imaging (MRSI) has been shown to provide valuable information about the metabolic content of the anatomy of interest and thus has been increasingly used in clinical research. However, the long acquisition time associated with multidimensional MRSI is a barrier for translation of this technology to the clinic. I hypothesize that compressive sensing can accelerate conventional MRSI acquisition and hence a novel approach to reduce the acquisition time of MRSI through the application of compressive sensing, by exploiting the statistical sparsity inherent in MRSI data is formulated and presented in this chapter. A retrospective analysis of the application of such a reconstruction method for ^{1}H MRSI of an *in vitro* MRSI brain phantom, *in vivo* brain (normal and cancer) and prostate cancer is detailed. The results are compared with the full k-space reconstruction using root-mean-square-error (RMSE) and performing a one-way ANOVA comparing voxel-wise metabolite intensities computed from the original and corresponding locations in the accelerated reconstructions, to evaluate the implementation.

3.1 MRSI

3.1.1. Introduction

MRSI is a combination of MRI and spectroscopy methods and has been increasingly used in clinical research to assess therapy and aid in diagnosis (22-24). It is well established that malignant prostate and brain tumors express increased levels of choline (Cho)

(25). It has also been demonstrated that most brain tumors express decreased levels of N-acetylaspartate (NAA) and creatine (Cr) leading to the usage of a Cho to NAA index (CNI) as a cancer biomarker (25-28). The peaks of NAA and Cr observed in ^{1}H – MRSI represent a combination of NAA + N-acetylaspartylglutamate (NAAG), and Cr + phosphocreatine (PCr) respectively. Similarly, a useful biomarker for prostate cancer is the ratio of the sum of Cho and Cr to citrate (Cit). It has been extensively shown that Cit levels decrease while Cho increases in malignant prostate tumors (25).

3.1.2. Simplified clinical MRSI pulse sequence

The timing diagram of a volume selective 2D MRSI sequence is shown in figure 3.1. This sequence is based on the point resolved spectroscopy (PRESS) pulse sequence, which has then been modified to encode the spatial dimensions using phase encodes (29). The goal of this experiment is selectively excite spins within a slice of interest of the imaging volume. This is achieved by employing 2 phase encoding gradients, one for each spatial dimension. Both the RF pulses used are slice selective and hence achieve spatial localization. The gradient perpendicular to the directions of the interested slice (G_{SS} in this figure) has the greatest strength to obtain a thin slice in that direction.

The 90^{o} -180^{o} combination forms a spin echo encoded in the two dimensions of the slice which is again refocused by the second 180^{o} pulse after being slice selected. The ADC is typically used to record one half of the second echo. The pulse sequence offers 2 parameters of T_{E1} and T_{E2} to choose appropriate echo times to acquire signals of interest.

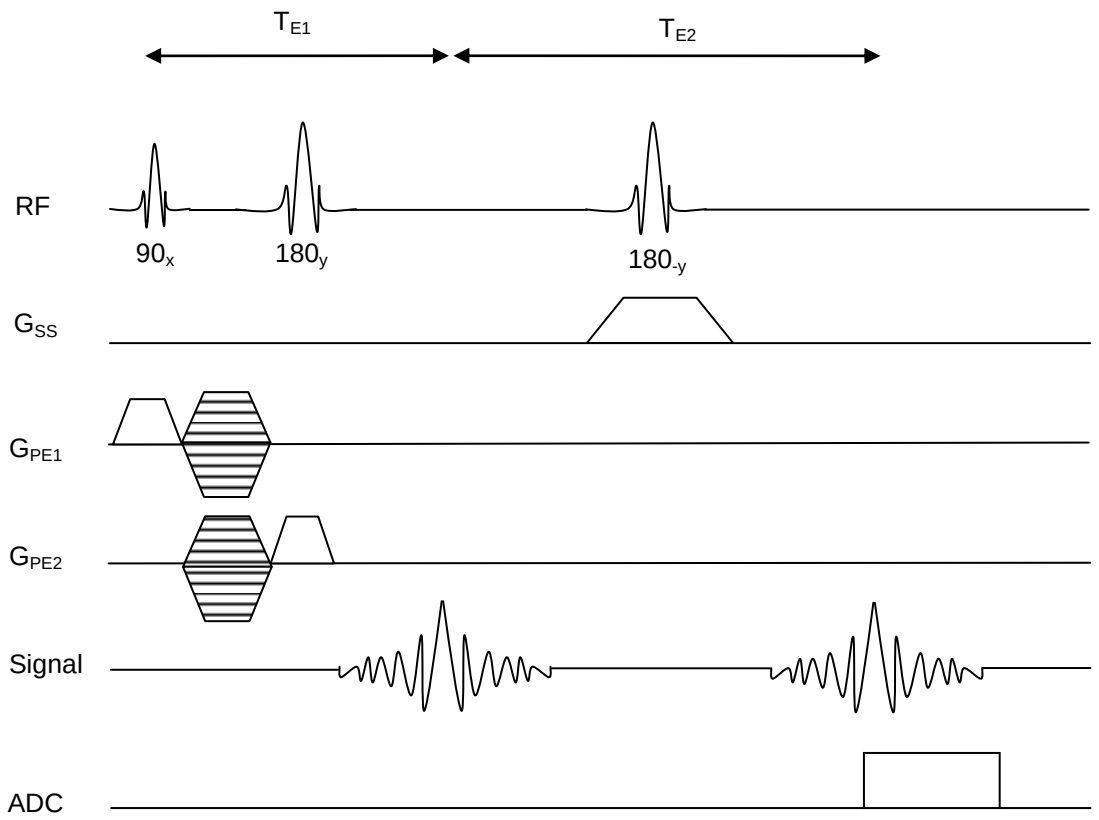

Figure 3.1 A volume selective 2D PRESS based MRSI pulse sequence

3.1.3. Speed-up in MRSI acquisition

The advantages of multi-voxel (2 and 3 dimensional) spectroscopy over single voxel spectroscopy are widely established (28,30). It is possible to obtain better localization of metabolic abnormality and also observe changes in regions originally outside the morphologic lesion using multi-voxel MR spectroscopy. However, the major disadvantage of this technique is the long acquisition time, which is a barrier for routine clinical use (28,30-31). This is primarily due to the necessary presence of increased phase encodes for acquisition.

In general, the capability of reduction in acquisition time with minimal loss of information is limited by the physics governing the modality. In MR based techniques, reduction of acquisition time is conventionally accomplished in one of two methods. One of the approaches that have been used is to acquire fewer values of k-space while the other methods include the exploitation of the redundancy in spatial or temporal domains or both together (32-33). Several fast chemical shift imaging/spectroscopic imaging approaches have been developed in the past and compared theoretically (34) and experimentally (35). In particular echo-planar spectroscopic imaging (EPSI) (36-37) is a powerful spectroscopic imaging technique that remains under-utilized in the clinic (38). This method speeds up spectroscopic imaging by echo-planar read-out of one spectral and one spatial dimension, thereby achieving an acceleration factor equal to the number of points in that spatial dimension. For example, a 16X16 2D matrix would take 16 times less time with EPSI as conventional chemical shift imaging. However, the speed-up may be at the expense of signal-to noise ratio (38) and spectra could be affected by Nyquist ghost artifacts(39). The limiting factor again is the violation of the Nyquist criterion when k-space is undersampled beyond a certain limit thus reducing the SNR and giving rise to aliasing artifacts. I propose using CS as an innovative alternate approach to undersample MRSI k-space in a fashion such that data quality is preserved.

3.2 CS for MRSI

3.2.1. Utility of CS for MRSI

Application of CS for MRSI is apt as the data are sparse in multiple dimensions of frequency and space in transform domains of wavelets and total variation. Wavelet based analyses including quantification; spectral editing and denoising have been applied to magnetic resonance spectroscopy (40-43). Fast MRSI has also been accomplished by the use of wavelets to enable compression in the spectral/spatial domains exploiting the sparsity existing in this transform domain (44-45). The application of CS to MRSI acquisition can be implemented in two ways. One approach would be to assume that one does not have *apriori* information regarding the data in terms of spectral peaks and spatial location; and design a sampling matrix accordingly. This approach gains its strength from the fact that it is applicable to MRSI data irrespective of various MR and related acquisition parameters like nuclei under investigation, anatomy, spectral width, and water suppression.

A contrasting method would be to make use of the knowledge of the peak locations in frequency, methods to estimate water component in any given free induction decay (FID) during acquisition to enable better reconstruction of the smaller metabolites. CS has been also successfully implemented to perform MR parameter mapping experiments (46) making use of data models and thus gaining additional acceleration. Modified applications of compressed sensing involving model-based approaches can be used to accelerate MRSI acquisition even further. The drawback with such approaches is the loss of generality but valid assumptions, which are specific to the MRSI data being acquired, could enable further acceleration and more robust reconstruction. The reconstruction scheme implemented in this work is the former method with an aim to provide a general framework for all MRSI acquisitions.

3.2.2. Requirements for implementation of CS MRSI

Implementation of CS on any MR data set requires the fulfillment of three necessary conditions (16) and has been detailed in section 2.2. MRSI data is both spatially and spectrally sparse in the wavelet domain. Due to the effect of random sampling, the artifacts would be incoherent in this domain. The NCG algorithm alluded to in section 2.2.3 has been implemented in this work to reconstruct the MRSI data.

3.2.3. Sampling of MRSI data

The most significant difference between a uniform sampling method and the random sampling employed in CS is in the resulting aliasing from each approach for a zero-filled reconstruction case. Here, CS has an advantage due to the fact that the aliasing is incoherent unlike the equi-spaced sampling case of the EPSI. (The imaging analog of this problem has been demonstrated in figures 2.1 and 2.2.) This ensures that the reconstruction of MRSI data would not contain coherent aliasing artifacts, which could result in erroneous interpretation of the MRSI spectra. For MRSI data, a sampling mask based on the 2 dimensional variable density with increased number of samples in the center could be chosen. A typical mask used in this work is shown in figure 3.3 (red 3D mask). This ensures random sampling, incorporating *apriori* information about k-space. Also, the prospective implementation of a sequence based on such a mask for MRSI is relatively straight-forward when compared to an imaging pulse sequence due to the presence of phase encode in both undersampling directions. Undersampling of the k-space of the MRSI data in the phase encode directions alone has certain advantages and disadvantages. It has been shown that undersampling in increased dimensions increases sparsity resulting in better reconstructions for CS. For MRSI data, sparsity in the spectral dimension exceeds that in the spatial dimensions alone. This has also been demonstrated in the application of CS for the reconstruction of hyperpolarized ^{13}C MRSI data (47). However, the decrease in acquisition time due to undersampling in the temporal

dimension alone is marginal compared to that obtained due to undersampling of the phase encode directions. Also, the acceleration factor is not directly representative of the undersampling factor. Undersampling in the time dimension results in a k-space trajectory, which requires complex pulse sequences involving fast switching gradients.

3.3 Methods

3.3.1 MRSI data and undersampling

Retrospective studies on 2D MRSI data were performed on data acquired by collaborators at UT Southwestern and kindly provided for my analysis. The MRSI data consisted of a standard GE *in vitro* brain phantom (braino,(48)), normalbrain data, brain cancer and prostate cancer MRSI data sets. The metabolites present in the braino phantom are shown in figure 3.2 with the metabolites of interest encircled in red. (The superscripted number reveals the number of NMR peaks that a particular metabolite exhibits.) The relevant MR acquisition parameters for the different MRSI data sets are summarized in table 3.1.

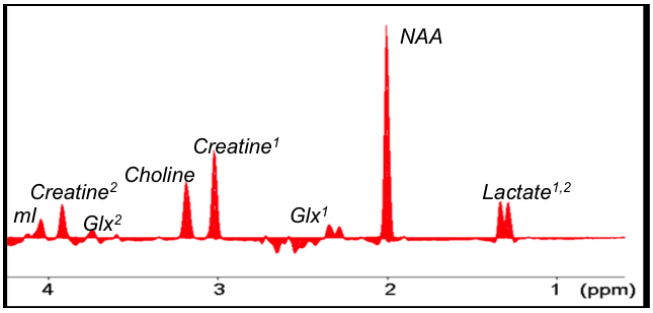

Figure 3.2 Metabolites present in the GE braino phantom (ppm – parts per million).

The data sets were normalized to a data range of 0 to 1 and then subjected to multi-dimensional Fourier transform to obtain the k-space to simulate the MR acquisition process. The data sets were assumed to be acquired in Cartesian k-space trajectory. The k-space thus

obtained was undersampled using a sampling mask generated based on the acceleration factor and variable density sampling.

Table 3.1 Acquisition parameters for the MRSI data

MRSI data	Scanner	RF Coil (receive)	TR(ms)	TE(ms)	Averages	Grid Size	FOV (mm^3)
GE braino	Siemens 3.0T Trio Tim	12 channel head coil	1700	270	2	16 x 16	160 x 160 x 40
Brain (N=6)	Siemens 3.0T Trio Tim	12 channel head coil	1700	270	4	16 x 16	100 x 100 x 15
Brain Tumor (N=2)	Philips 3.0T Achieva	8 channel head coil	1000	112	2	18 x 21 19 x 22	180 x 210 x 15 190 x 220 x15
Prostate cancer (N=2)	Philips 3.0T Achieva	Endorectal	1200 1000	140	1	14 x 10 16 x 12	25 x 50 x 33 20 x 51 x 26

A representative sampling mask for an acceleration factor of 4X is shown in figure 3.3 (3D red mask). The bars represent a sampling location while others represent an unsampled location. The mask was generated by picking random samples from a variable density weighted matrix to replicate the density of samples of the k-space with increased weight in the center and reduced samples in the outer edges. The value of the center of the density compensation that was chosen was dependent on the acceleration factor and was set to be equal to the inverse of the acceleration factor. This method was followed to allow a logical reduction of the sampling of the center while retaining random samples outside the center.

3.3.2 Reconstruction

The workflow of the proposed reconstruction is described in figure 3.3. The undersampled k-space was zero-filled and subject to inverse Fourier transform to obtain an initial estimate of the desired MRSI data. The reconstruction of the MRSI data was cast as a convex optimization problem whose solution was given by minimizing the cost function

described in equations [2.2] and [2.3]. The proposed method exploits the spatial sparsity and spectral sparsity present in the MRSI data. The 2 dimensional Daubechies wavelet transform was used to encode each 2D matrix at different spatial points. However, the data set was not treated as a composite data stack of 2D images. The complete MRSI data set *m* was reconstructed from all the 2D wavelet and total variation coefficients each time a comparison was made with the measured data *y*. This yields a better performance when compared to the method shown in (49), which treats the 2D MRSI data set as a stack of 2D images and estimates each of them separately. The proposed approach eliminates the cumulative error involved in the estimation of a 2D image at each time point and reduces the value of the L_2 norm term while not affecting the L_1 norm terms. The values for the regularization terms λ_{LI} and λ_{TV} were 0.001 and 0.005 respectively. The stopping criteria for the reconstruction were chosen to be a value less than 10^{-6} for the cost function (Є) or exceeding a maximum of 200 line-search iterations. However, the line-search criterion was rarely violated. The reconstruction was subject to 8 iterations to obtain convergence in the value of the cost function.

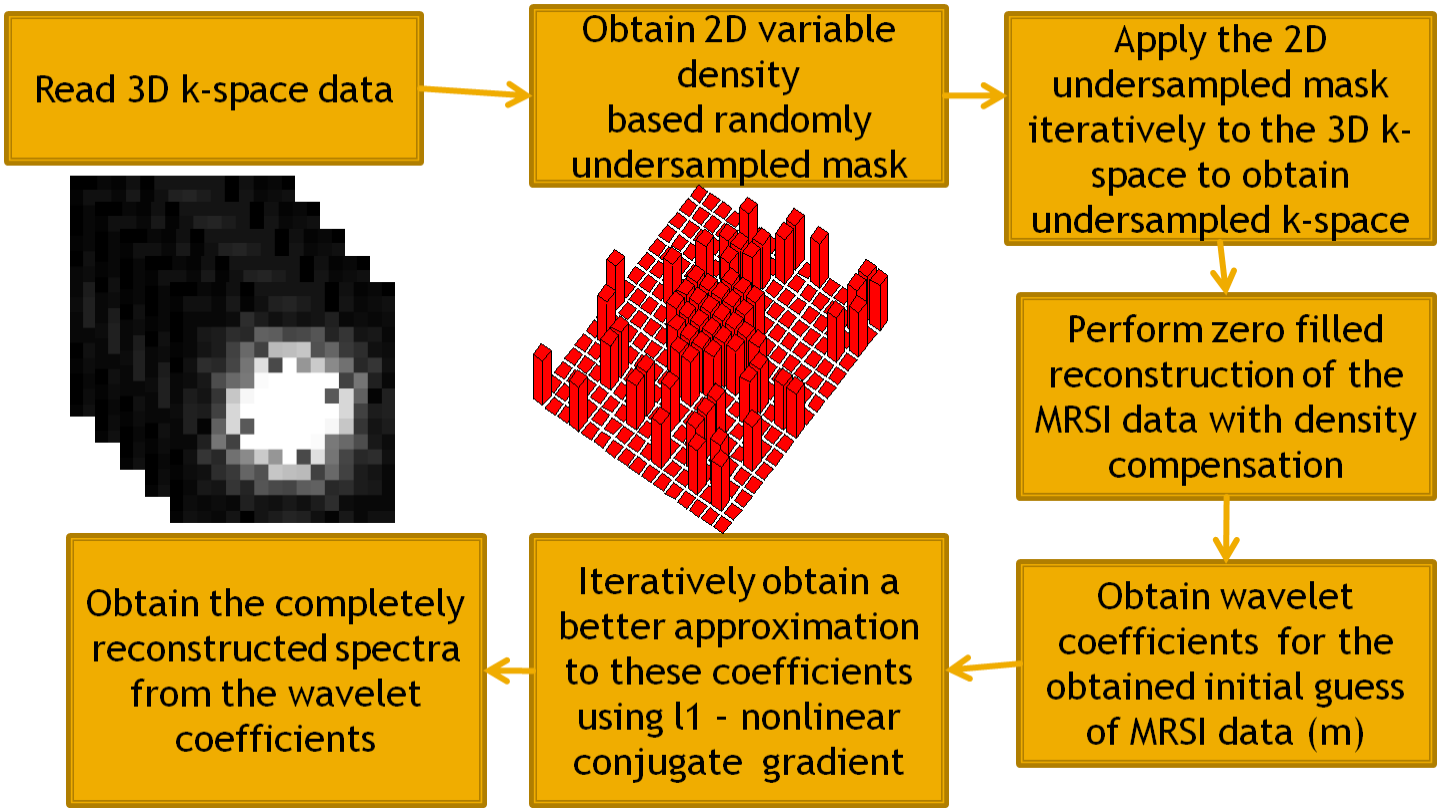

Figure 3.3 Cartoon depicting the workflow of the reconstruction for CS MRSI implementation

3.3.3 Acceleration factors and error metrics

Reconstruction of each data set was performed for 5 acceleration factors of 2, 3, 4, 5 and 10 to evaluate the data quality and utility of the approach implemented. The acceleration factors directly correspond to the saving in acquisition time as the undersampling is purely in the phase-encode directions. The error of reconstruction was quantified by the root mean square error metric (RMSE) computed as shown in equation [3.1]. Since the data range was normalized to vary from 0 to 1; RMSE is an equivalent of the commonly used normalized RMSE, which is obtained by the division of RMSE by the data range.

$$RMSE = \sqrt{\frac{1}{N}\left(\sum_{i=1}^{N}(y_i - y_i^{'})^2\right)} \qquad [3.1]$$

Here, *N* is the total number of data points in a MRSI data set, *y* is the data reconstructed from full k-space, *y'* is the reconstructed data from undersampled k-space.

3.3.4 Post-processing of MRSI data

The MRSI data sets were subjected to the following minimal processing steps in java based Magnetic Resonance User Interface (jMRUI) (50): (a) apodization to remove existing truncation artifacts, (b) baseline correction, (c) time-domain Hankel-Lanczos singular value decomposition filtering of residual water and fat peaks (d) automated zero-order global phase correction and (e) generation of metabolite maps using the Quantitation based on Quantum Estimation (QUEST) algorithm (51) from the "real" part of the phased NMR spectrum, where metabolite map intensities represent contributions of the respective spectral components in the QUEST fit. In case of the brain MRSI data (healthy and cancer), only the region interior to the brain was analyzed. The total number of voxels used for further analysis was 600, 163 and 36 for the healthy brain, brain tumor and prostate cancer datasets, respectively. For the ratio

calculations, voxels having a denominator value of 0 (signifying a lack of deterministic solution in the QUEST fit) in the original data or CS-reconstructed data were set to 0. A sample of the fitting routine is shown for a voxel from the normal brain data is shown in figure 3.4 showing the original (a), estimate from the basis set (b), the fitted metabolites (c) and the resulting residue (d)

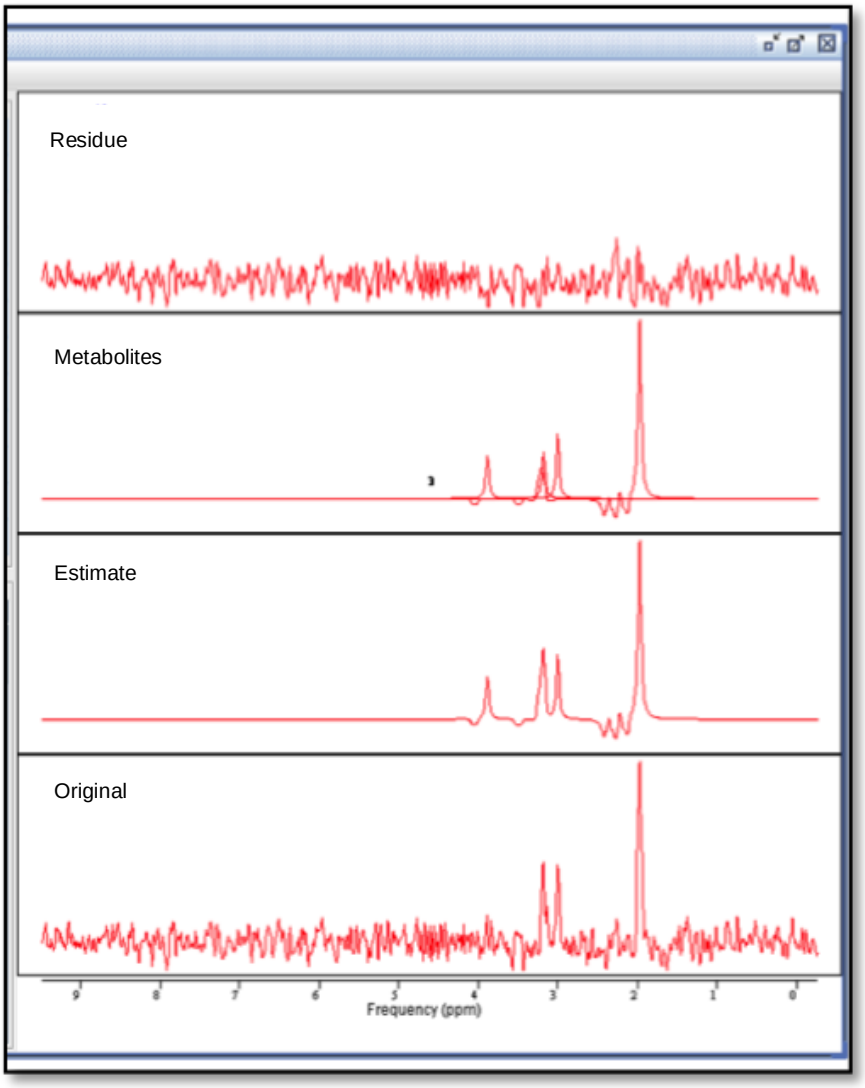

Figure 3.4 Screen capture of the QUEST fitting in jMRUI for a voxel from the normal brain data showing (a) the spectrum from the chosen voxel, (b) estimate from the basis set, (c) the resulting fit and (d) the residue

3.3.5 Statistical Analyses

The metabolite map intensities for each reconstruction and relevant metabolite ratios (CNI for *in vitro* phantom, healthy brain and brain tumor, ((Cho+Cr)/Cit) for prostate cancer) were subjected to a one-way repeated measures ANOVA and followed by Bonferroni's multiple comparison test to further evaluate the effect of correlations among the reconstruction for the different acceleration values chosen (Graphpad Prism; Graphpad Software Inc., La Jolla, CA). The resulting 't' values from Bonferroni's test were converted into p-values (Microsoft Excel, Microsoft Inc, Redmond, WA). The null hypothesis was that there did not exist any significant difference between the original and reconstructed spectra. (A p-value < 0.05 was considered statistically significant.)For the ratio calculations, voxels having a denominator value of 0 (signifying a lack of deterministic solution in the QUEST fit) in the original data or CS-reconstructed data were set to 0. A p-value < 0.05 was considered statistically significant.

3.4 Results

3.4.1 Phantom data

The processed *in vitro* phantom reconstruction data for all the 256 voxels can be seen in figure 3.5 for the complete k-space case (1X) and the CS based reconstructed spectra resulting from acceleration of 2X, 3X, 4X, 5X and 10X for the MR image shown in the center. A voxel from the center of the phantom (green) and another outside of it (red) are chosen for further examination of SNR and signal localization shown in figure 3.6.It can be observed from figures 3.5 and 3.6 that the reconstruction preserves the localization information along with acceptableSNR till 5X.At 10X the reconstruction overestimates the amplitudes of the metabolite signal leading to increased errors.

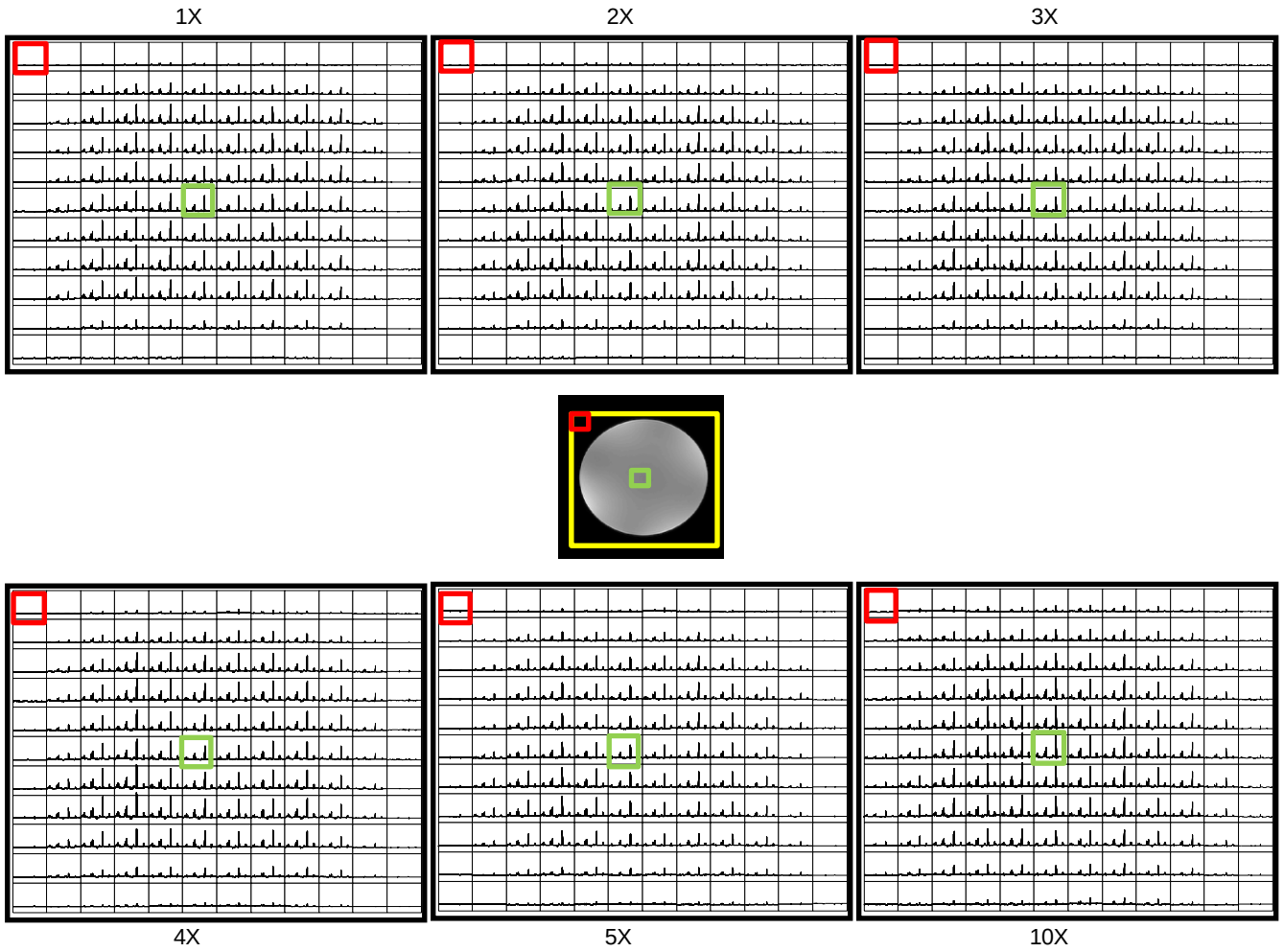

Figure 3.5 Reconstruction of the data grid for the braino phantom for the acceleration factors of 1, 2, 5 and 10. The central image shows the MR image with the MRSI region of interest (yellow square). Also shown are two locations (red and green voxels) which are further closely examined in figure 3.5

The metabolite maps for NAA, Cho, Cr and lactate (Lac) for both the original and reconstructed cases of the *in vitro* phantom can be seen in figure 3.7. It can be seen that the spatial distribution of the metabolites are similar for accelerations till 5X. However, the metabolite maps at 10X show increased intensity as indicated by the spectra in figure 3.6.

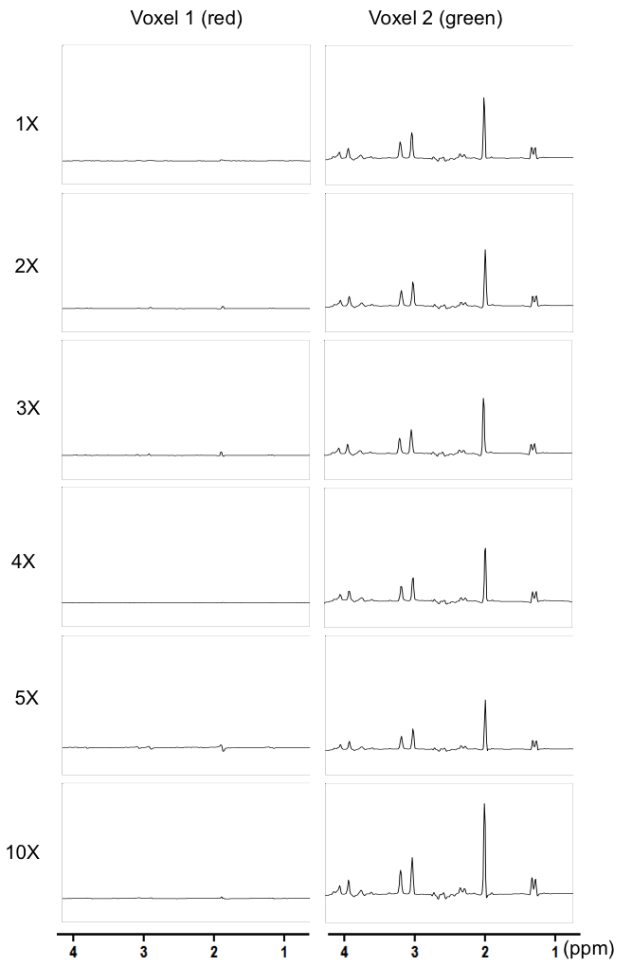

Figure 3.6 Spectra from 2 selected voxels (red and green voxels from figure 1) for the braino MRSI phantom data set for the acceleration factors of 1, 2, 5 and 10X. The y-axis limits for all the plots are -0.25 to 1.25

The results of the one-way ANOVA of the metabolite intensities for the phantom MRSI data have been summarized in table 3.2. It can be seen that the reconstructions resulting from acceleration of 2, 3, 4 and 5X have statistically insignificant differences as compared with the original.The 10X case shows significant differences and the increased metabolite intensities are observed in the metabolite maps in figure 3.7 as well.

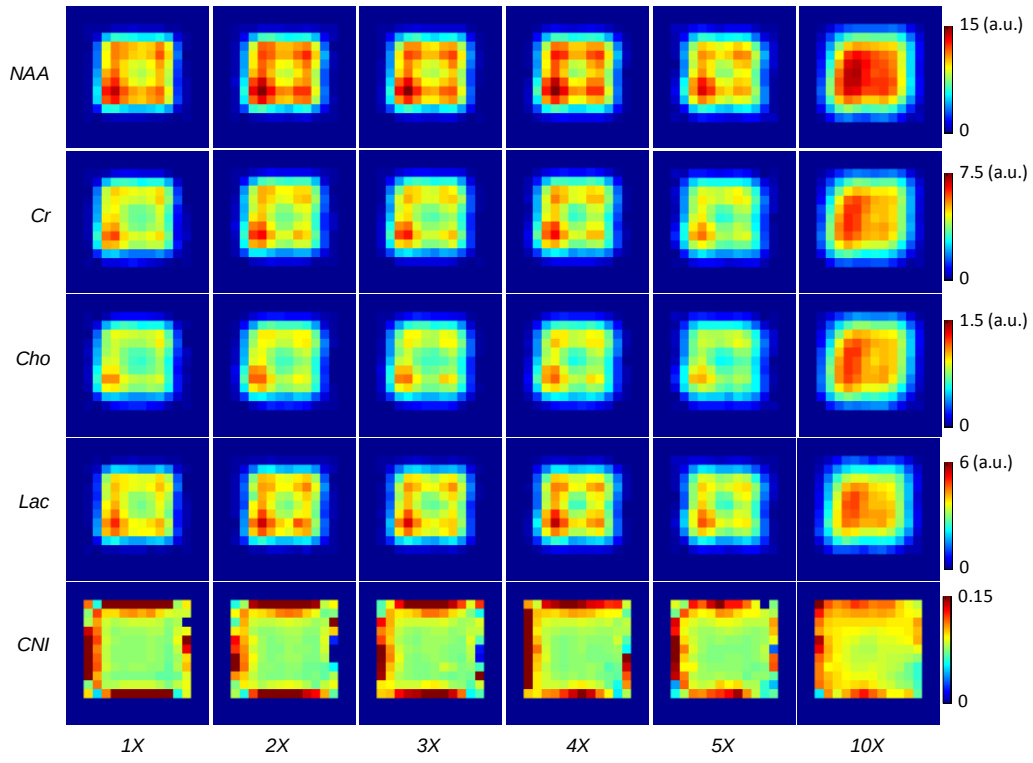

Figure 3.7 Comparative metabolite maps of NAA, Cr, Cho, Lac and CNI for the GE braino phantom for the acceleration factors of 1, 2, 3, 4, 5 and 10X. The yellow box on the MR anatomical image (figure 3.4) indicates the MRSI region of interest depicted in the maps.

3.4.2 Normal brain data

The results of the reconstruction of a representative healthy brain MRSI data set are shown in figures 3.8 and 3.9. Figure 3.8 shows the MRSI grids corresponding to a region (yellow square) shown on the anatomical scout scan (center) at different acceleration factors. It can be seen that the reconstructed MRSI data exhibit similar spatial profiles as the original over the range of accelerations. The green and red boxes represent the locations of 2 voxels chosen to inspect the quality of the reconstructed spectra in figure 3.8. The voxel overlapping the ventricles (green) shows reduced concentrations of NAA, Cr and Cho (shown in the right column of figure 3.9) compared the metabolite levels in the other voxel (red), as is expected. The reconstructed spectra for the accelerated cases shown in the rows 2 to 4 of figure 3.9 are similar to the original. It can be observed that the CS reconstruction preserves the line-shape of the original data as well but spectra are smoother at higher acceleration. Figure 3.10 shows the metabolite maps of NAA, Cr, Cho (reflecting area under the peak) and the CNI as a function of acceleration. The hyper-intensities on the original and reconstructed cases occur in similar locations. However at 10X, the metabolite maps show increased intensity as compared to the original

3.4.3 Brain tumor and prostate cancer

Figures 3.11 and 3.12 illustrate the results for reconstruction for the chosen acceleration factors for representative brain and prostate tumor data sets. It can be noticed from the figures that the reconstruction preserves the localization information. The anatomical figures in the center have a yellow square representing the voxels of interest. The original and CS reconstructed brain tumor MRSI dataset for two voxels representing normal tissue and cancer tissue, respectively, are shown in figure 3.13(a).

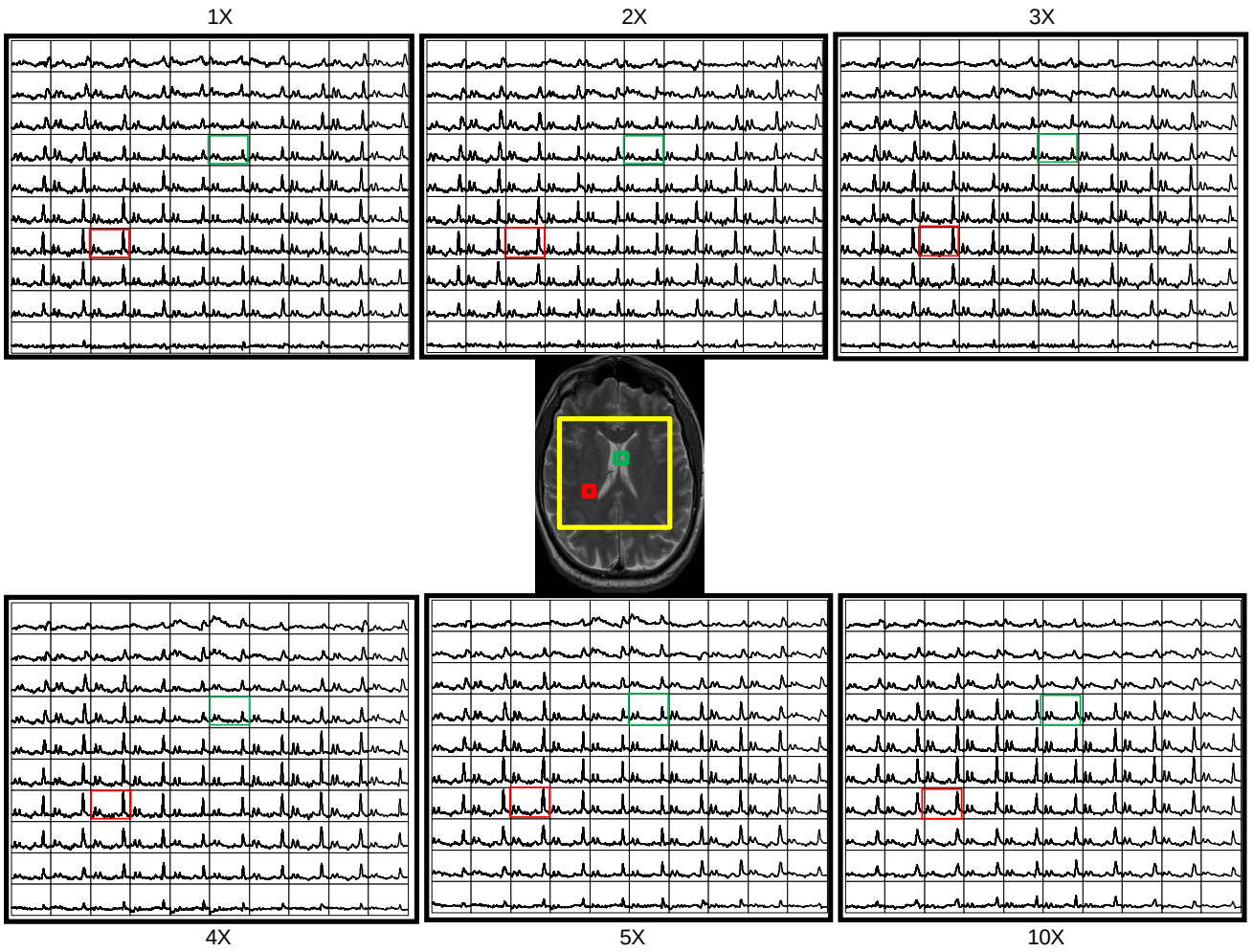

Figure 3.8 Reconstruction of the data grid for a representative brain MRSI data set for the acceleration factors of 1, 2, 5 and 10. The central image shows the anatomical image with the MRSI region of interest (yellow square). Also shown are two locations (red and green voxels), which are further closely, examined in figure 3.9

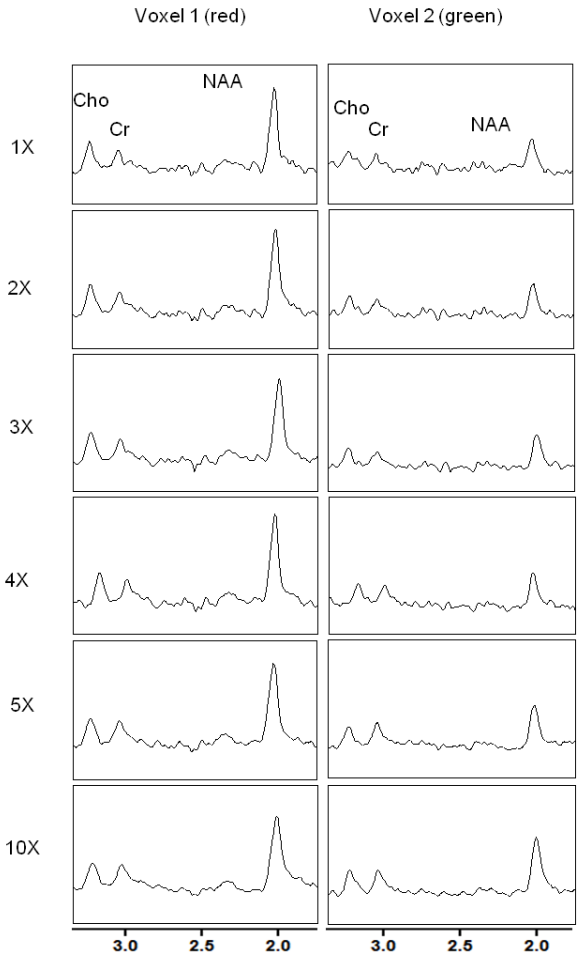

Figure 3.9 Spectra from 2 selected voxels (red and green voxels from figure 1) for a representative brain MRSI data set for the acceleration factors of 1, 2, 5 and 10X. The y-axis limits for all the plots are -0.25 to 1.

It can be seen that the different metabolite profile that discriminates normal brain tissue from cancerous tissue has been faithfully preserved for the results of reconstruction up to 10X. Figure 3.13(b) depicts the reconstruction of two voxels representing normal tissue and cancer tissue respectively, of a prostate cancer MRSI data set.

.

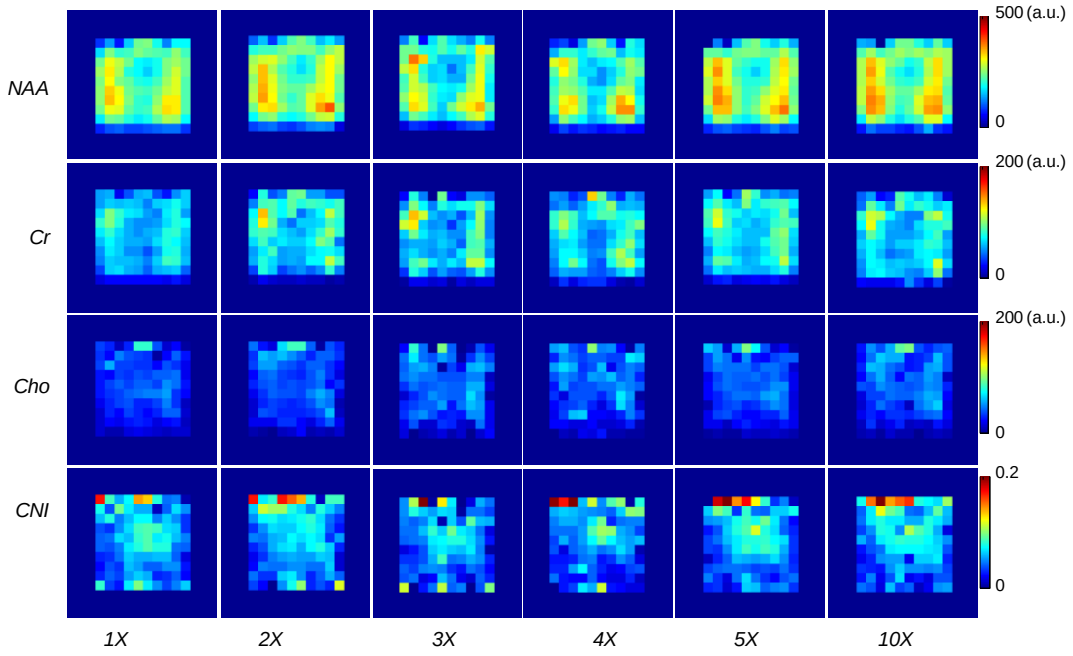

Figure 3.10 Comparative metabolite maps of NAA, Cr, Cho and CNI for a normal brain data set for the acceleration factors of 1, 2, 5 and 10X. The yellow box on the MR anatomical image (figure 3.5) indicates the MRSI region of interest depicted in the maps.

The CS reconstructed spectra maintain fidelity of the different metabolic profiles for both the normal prostate and prostate tumor cases as well. The metabolite maps generated based on these reconstructions are shown in figures 3.14(a) and (b) as a function of acceleration. For the brain tumor data set the metabolite and CNI maps for accelerations of 2X and 5X maintain high fidelity while those at 10X show increased deviation from the original data. For the prostate cancer data set, a decrease in intensity is seen in the metabolite maps as a function of acceleration but the ratio map of (choline+creatine)/citrate for the prostate cancer data set displays high fidelity even up to 10X, particularly for hot-spot localization.

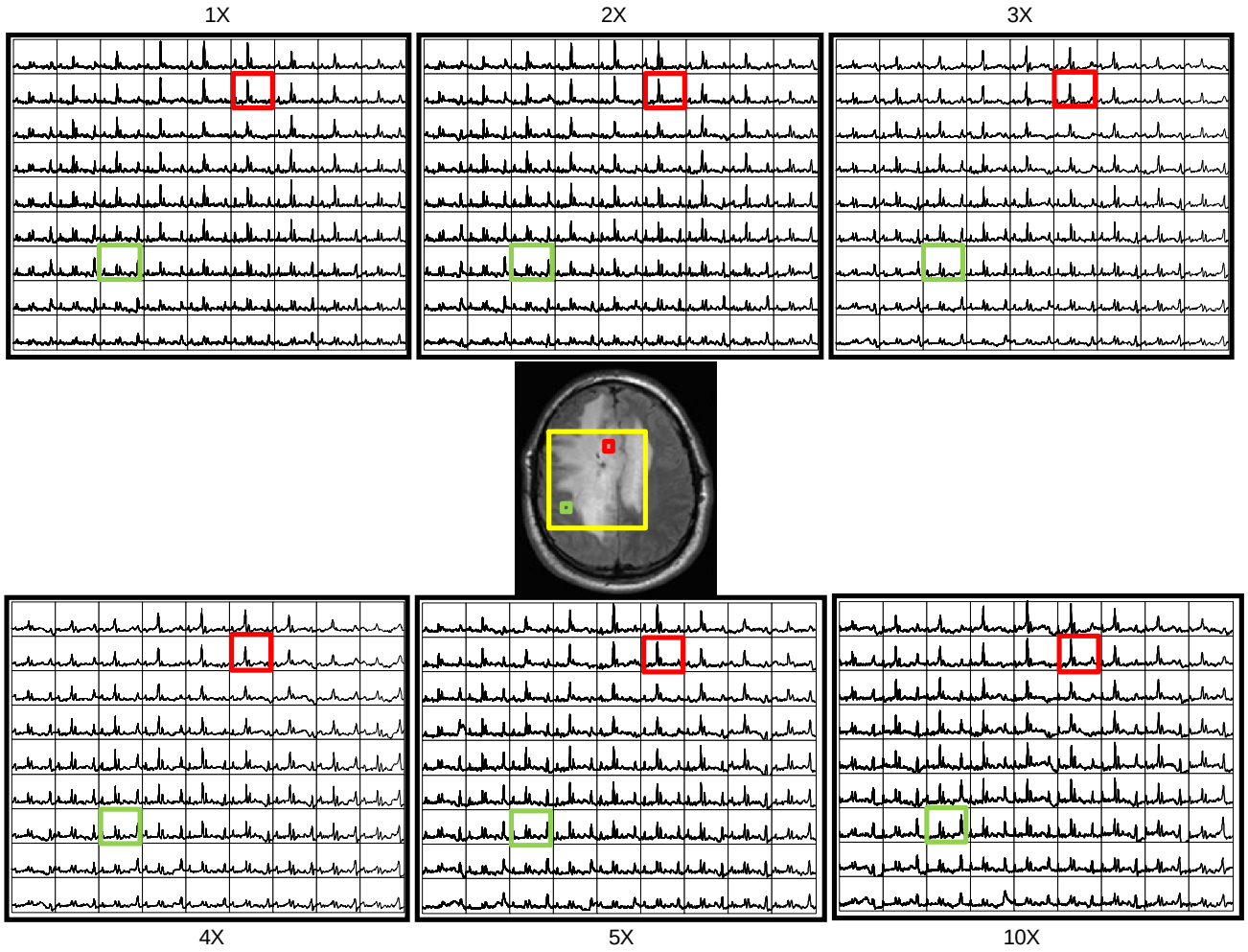

Figure 3.11 Reconstruction of the data grid for a representative brain cancer MRSI data set for the acceleration factors of 1, 2, 3, 4, 5 and 10X. The central image shows the anatomical image with the MRSI region of interest (yellow square). Also shown are two locations (red and green voxels) which are further closely examined in figure 3.13 (a)

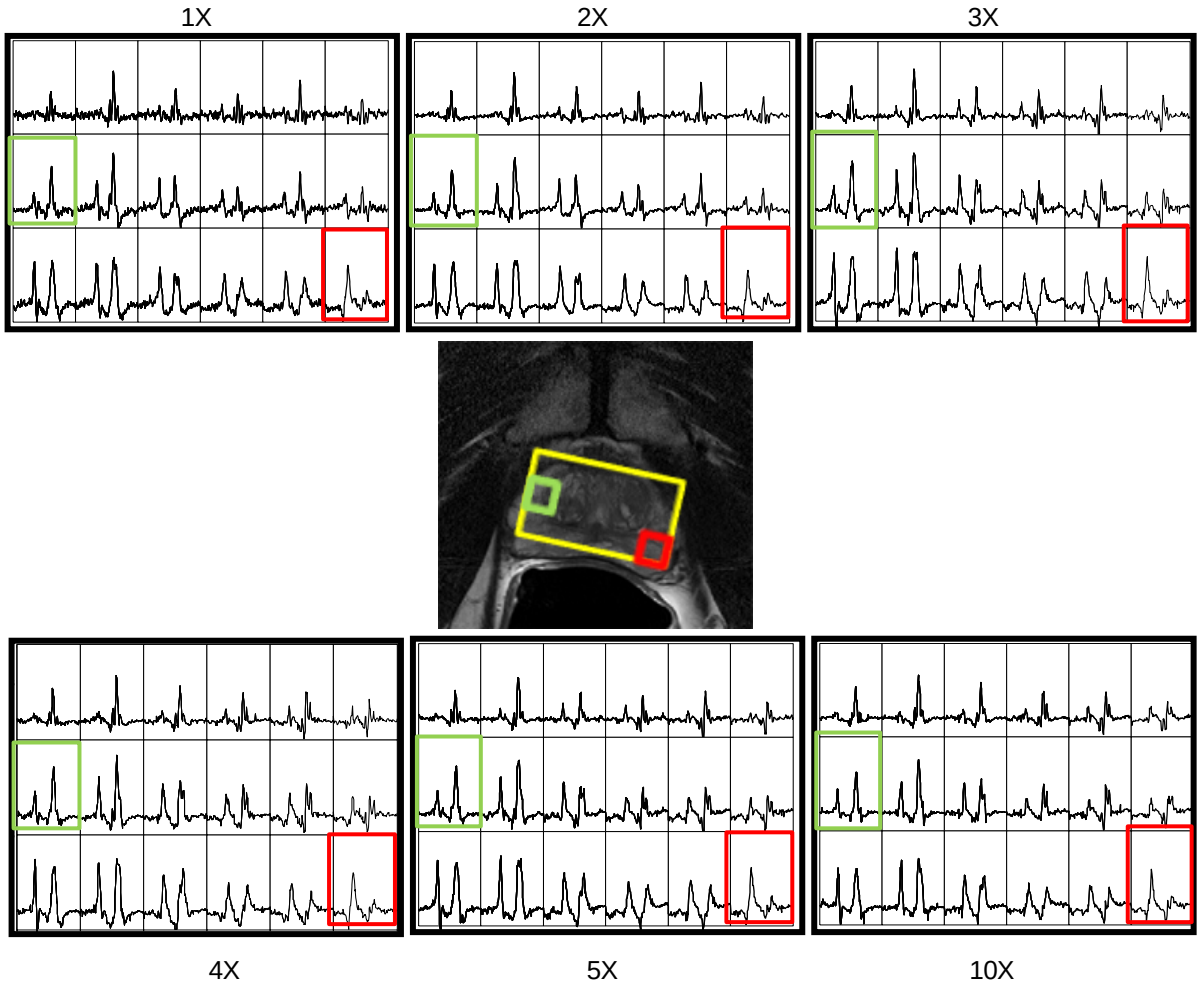

Figure 3.12 Reconstruction of the data grid for a representative prostate cancer MRSI data set for the acceleration factors of 1, 2, 5 and 10. The central image shows the anatomical image with the MRSI region of interest (yellow square). Also shown are two locations (red and green voxels), which are further closely, examined in figure 3.13 (b)

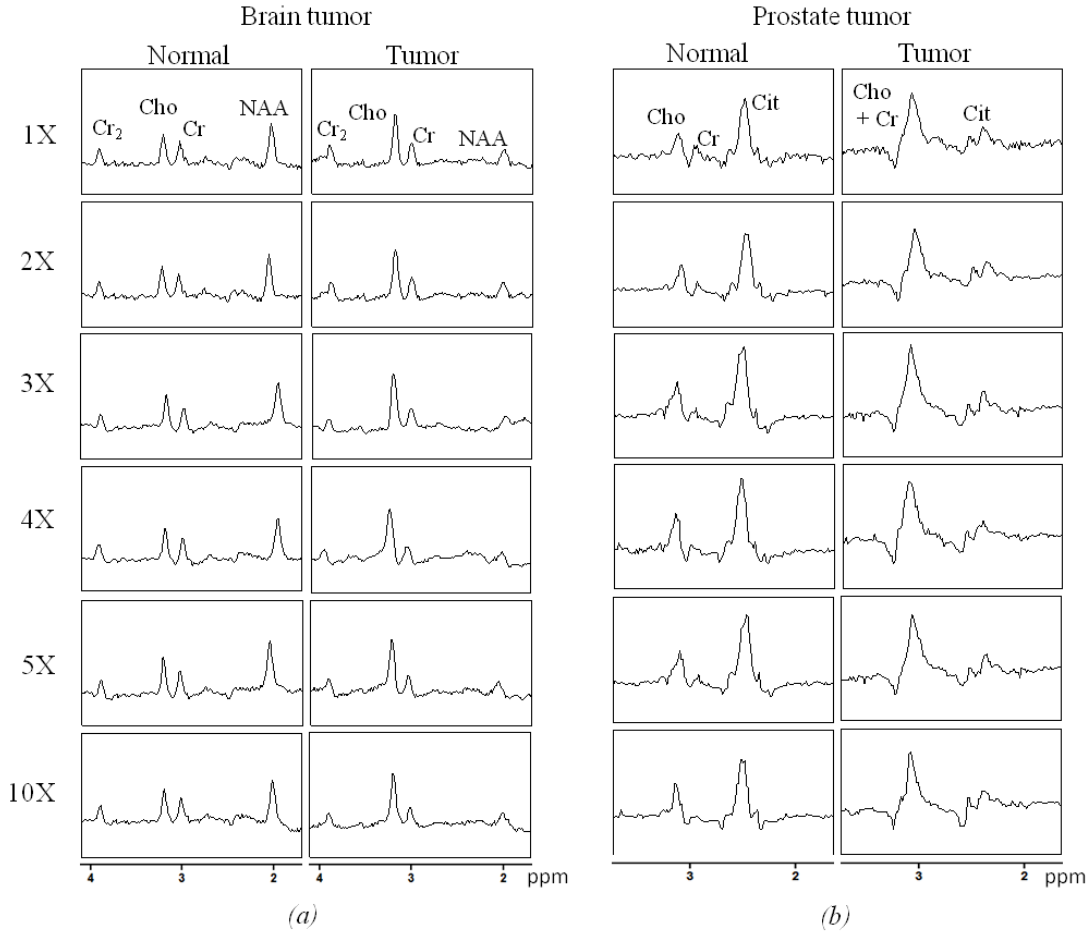

Figure 3.13 Spectra from 2 selected voxels for representative (a) brain tumor and (b) prostate cancer MRSI data set for the acceleration factors of 1, 2, 5 and 10X. In each case the left column shows a voxel from healthy tissue while the right panel shows a voxel in the tumor bearing region. The y-axis limits for all the plots are -0.25 to 1

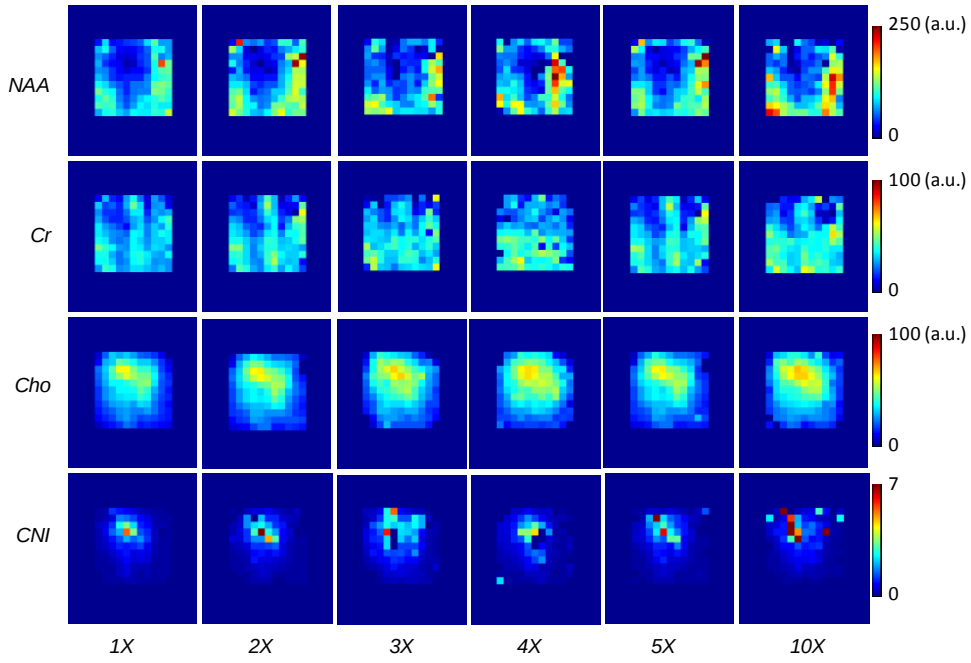

(a)

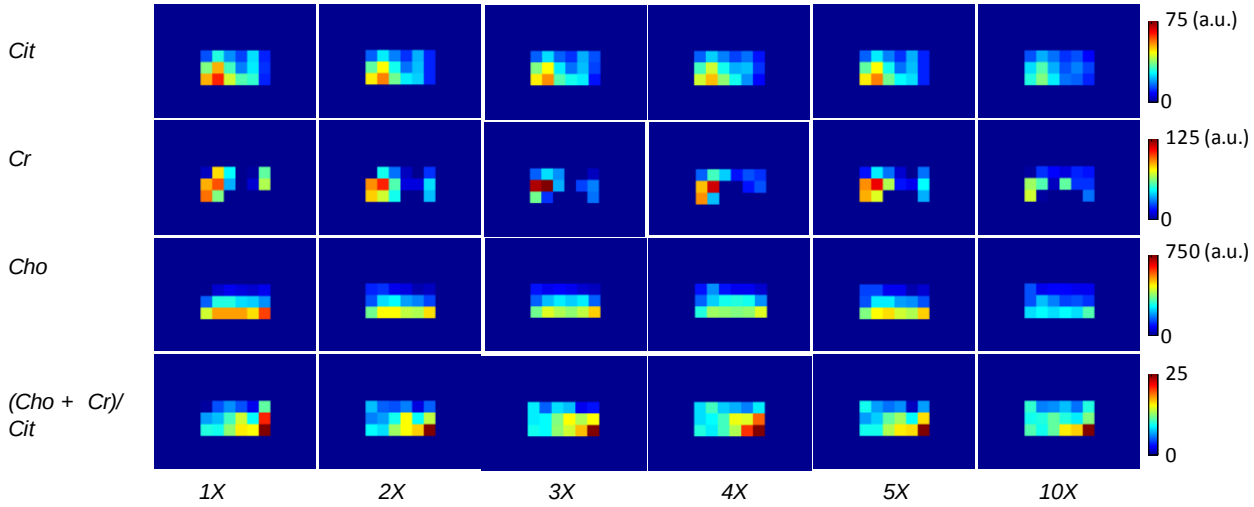

(b)

Figure 3.14 Comparative metabolite and ratio maps for (a) brain tumor (NAA, Cr, Cho) and (b) prostate cancer (Cit, Cr, Cho) MRSI data set for the acceleration factors of 1, 2, 5 and 10X MRSI data. Ratio maps depict CNI (Cho/NAA) for the brain tumor data and (Cho+Cr)/Cit for the prostate cancer data. The yellow box on the anatomical MR image indicates the MRSI region of interest depicted in the maps.

Table 3.2 Mean metabolite intensities (arbitrary units) and ratios (± standard deviation) for the pooled voxel data for four data types: *in vitro* phantom, normal brain, brain tumor and prostate cancer, as a function of acceleration, * denotes a p value < 0.05 resulting from the one-way ANOVA followed by the Bonferroni's test.

		NAA (a.u.)	Cit	Cr	Cho	Lac.	Ratio†
In vitro phantom N= 132 voxels	1X	552 ± 441		241 ±183	46 ± 33	194 ± 158	0.10 ± 0.05
	2X	589 ± 455		256 ± 188	49 ± 35	205 ± 162	0.09 ± 0.04
	3X	567 ± 437		247 ± 183	47 ± 33	197 ± 56	0.10 ± 0.03
	4X	585 ± 444		255 ± 184	49 ± 34	203 ± 158	0.11 ± 0.17
	5X	544 ± 388		237 ± 162	45 ± 30	189 ± 138	0.09 ± 0.03
	10X	700 ±424*		311 ±187*	74 ± 37*	233 ±144*	0.12 ± 0.04*
Brain (Healthy) N= 600 voxels	1X	200 ± 97		52 ± 28	14 ± 9		0.075 ± 0.047
	2X	200 ± 99		52 ± 34	14 ± 10		0.073 ± 0.064
	3X	203 ± 99		52 ± 34	14 ± 10		0.072 ± 0.060
	4X	203 ± 110		52 ± 31	14 ± 10		0.087 ± 0.186
	5X	202 ± 110		52 ± 31	14 ± 11		0.082 ± 0.152
	10X	241 ±138*		65± 39*	18 ± 13*		0.086 ± 0.083*
Brain Tumor N=163 voxels	1X	107 ± 64		42 ± 24	32 ± 14		0.468 ± 0.519
	2X	108 ± 64		43 ± 26	32 ± 14		0.625 ± 1.50
	3X	106 ±70		41 ± 25	33 ± 20		0.580 ± 1.04
	4X	116 ± 80		43 ± 27	33 ± 15		0.413 ± 0.60
	5X	106 ± 74		42 ± 24	32 ± 14		0.712 ± 1.82
	10X	111 ±88		37 ± 17*	33 ± 15		0.837 ±1.89*

Table 3.2 continued

		NAA (a.u.)	Cit	Cr	Cho	Lac.	Ratio†
Prostate Cancer N=36 voxels	1X		19 ± 17	50 ± 82	201 ± 173		19.25 ± 25.23
	2X		19 ± 13	43 ± 83	185 ± 146		14.10 ± 10.21
	3X		18 ± 12	54 ±79	179 ± 142		18.81 ± 27.72
	4X		18 ± 11	47 ±61	196 ±124		18.96 ± 23.62
	5X		19 ± 13	38 ± 54	183 ± 145		16.12 ± 16.44
	10X		14 ± 11*	38 ± 54	147 ± 96*		16.38 ± 23.59

3.4.4 Error quantification and statistics

The mean ± sd. values calculated for each metabolite at acceleration factors of 1, 2, 3, 4, 5 and 10 for the *MRSI* data sets are reported in table 3.2. It can be seen that the mean values of these metabolites are comparable at accelerations up to 5X while the results at 10X show statistically significant differences in 7 of the 16 metabolite maps compared with the original data (1X) as shown in tables 3.3 – 3.6 for the four MRSI data types. It can also be noticed that the 10X depicts differences from the reconstructions resulting at accelerations of 2, 3, 4 and 5 indicated by the statistically significant differences in these tables. The mean values for the ratio maps are also similar to the original, demonstrating that there are no significant changes in the values of the critical biomarkers up to 5X for the (brain phantom), healthy brain and brain tumor data and up to 10X for the prostate cancer data. The errors of reconstruction quantified by the RMSE metric for the 4 data types at the 5 acceleration factors can be seen in figure 3.15. The RMSE values increase with increase in acceleration, as is expected but remains below 0.05 for accelerations up to 10X.

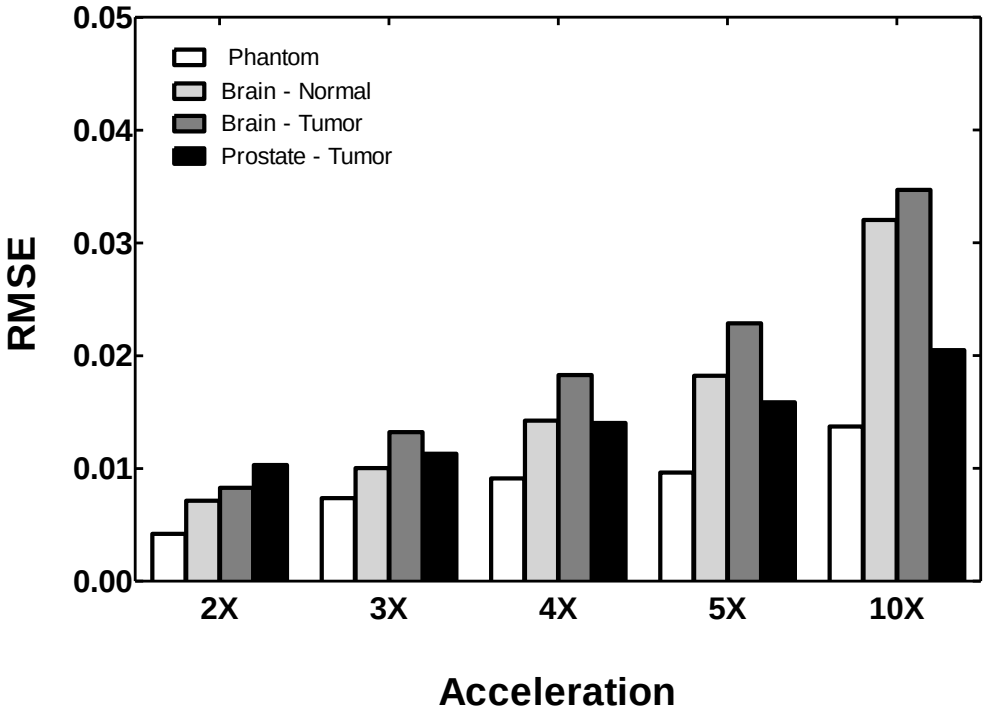

Figure 3.15 Graph of Root mean square error (RMSE) values for the different MRSI data for the acceleration factors of 2, 3, 4, 5 and 10X in comparison with the original data (1X)

Table 3.3 P-values resulting from the one-way ANOVA followed by Bonferroni's comparison test for the *in vitro* phantom, * denotes a p value < 0.05.

		NAA	Cr	Cho	Lac.	Ratio^{T}
In vitro phantom N= 132 voxels	1X vs 2X	0.54	0.55	0.51	0.59	0.40
	1X vs 3X	0.80	0.80	0.78	0.88	0.43
	1X vs 4X	0.57	0.57	0.55	0.64	0.46
	1X vs 5X	0.89	0.88	0.87	0.84	0.29
	1X vs 10X	0.07	0.05	0.01*	0.13	0.03*
	2X vs 3X	0.71	0.71	0.69	0.69	0.96
	2X vs 4X	0.95	0.96	0.94	0.94	0.17
	2X vs 5X	0.46	0.46	0.43	0.47	0.77
	2X vs 10X	0.13	0.09	0.01*	0.23	0.03*
	3X vs 4X	0.75	0.74	0.74	0.74	0.18
	3X vs 5X	0.69	0.69	0.67	0.73	0.73
	3X vs 10X	0.09	0.06	0.01*	0.15	0.03*
	4X vs 5X	0.49	0.48	0.46	0.51	0.12
	4X vs 10X	0.12	0.09	0.01*	0.21	0.40
	5X vs 10X	0.06	0.04*	0.01*	0.10	0.04*

Table 3.4 P-values resulting from the one-way ANOVA followed by Bonferroni's comparison test for the healthy brain MRSI data, * denotes a p value < 0.05.

		NAA	Cr	Cho	Ratio†
Brain (Healthy) N= 600 voxels	1X vs 2X	0.90	0.86	0.94	0.79
	1X vs 3X	0.49	0.89	0.88	0.66
	1X vs 4X	0.86	0.88	0.90	0.98
	1X vs 5X	0.49	0.89	0.88	0.28
	1X vs 10X	0.00*	0.00*	0.00*	0.14
	2X vs 3X	0.42	0.76	0.82	0.86
	2X vs 4X	0.86	0.88	0.90	0.98
	2X vs 5X	0.42	0.76	0.82	0.21
	2X vs 10X	0.00*	0.00*	0.00*	0.11
	3X vs 4X	0.87	0.88	0.90	0.07
	3X vs 5X	1.00	1.00	1.00	0.17
	3X vs 10X	0.00*	0.00*	0.00*	0.09
	4X vs 5X	0.87	0.88	0.90	0.42
	4X vs 10X	1.00	1.00	1.00	0.81
	5X vs 10X	0.00*	0.00*	0.00*	0.55

Table 3.5 P-values resulting from the one-way ANOVA followed by Bonferroni's comparison test for the brain cancer MRSI data, * denotes a p value < 0.05.

		NAA	Cr	Cho	$Ratio^T$
Brain Tumor N=163 voxels	1X vs 2X	0.83	0.63	0.98	0.35
	1X vs 3X	0.82	0.92	0.99	0.18
	1X vs 4X	0.38	0.03	0.33	0.08
	1X vs 5X	0.82	0.93	0.98	0.18
	1X vs 10X	0.38	0.03*	0.33	0.08
	2X vs 3X	0.66	0.57	0.97	0.59
	2X vs 4X	0.49	0.02*	0.32	0.23
	2X vs 5X	0.66	0.57	0.96	0.59
	2X vs 10X	0.49	0.02*	0.32	0.23
	3X vs 4X	0.29	0.03*	0.34	0.44
	3X vs 5X	1.00	1.00	1.00	1.00
	3X vs 10X	0.29	0.03*	0.33	0.44
	4X vs 5X	0.29	0.03	0.34	0.44
	4X vs 10X	1.00	1.00	0.99	1.00
	5X vs 10X	0.29	0.03*	0.34	0.44

Table 3.6 P-values resulting from the one-way ANOVA followed by Bonferroni's comparison test for the prostate cancer MRSI data, * denotes a p value < 0.05.

		Cit	Cr	Cho	$Ratio^T$
Prostate Cancer N=36 voxels	1X vs 2X	0.28	0.59	0.35	0.38
	1X vs 3X	0.82	0.78	0.21	0.95
	1X vs 4X	0.80	0.81	0.75	1.00
	1X vs 5X	0.28	0.40	0.30	0.59
	1X vs 10X	0.09	0.38	0.03*	0.55
	2X vs 3X	0.36	0.43	0.66	0.36
	2X vs 4X	0.37	0.76	0.50	0.38
	2X vs 5X	1.00	0.73	0.90	0.70
	2X vs 10X	0.03*	0.71	0.07	0.75
	3X vs 4X	0.97	0.61	0.30	0.95
	3X vs 5X	0.36	0.29	0.75	0.56
	3X vs 10X	0.07	0.28	0.11	0.52
	4X vs 5X	0.37	0.53	0.44	0.60
	4X vs 10X	0.07	0.51	0.04*	0.55
	5X vs 10X	0.03*	0.97	0.08	0.95

3.5 Conclusion

The goal of this study was to investigate an approach to accelerate ^{1}H MRSI acquisition without loss of information, with a view to facilitate widespread integration of ^{1}H MRSI into standard clinical protocols. Using compressive sensing based reconstruction; I have demonstrated a potential reduction of acquisition time by up to 80% or more for ^{1}H MRSI, with negligible loss of information as evaluated based on clinically relevant metrics. It can be observed that the reconstructed spectra display lesser noise when compared to the original spectra. This can be attributed to the de-noising quality of the wavelets and the smoothing effect of the total variation factor in the reconstruction. The reconstructed spectra at 10X are successful in identifying the metabolites in the data set and do not show erroneous peaks and noise level comparable to the peaks present. However, the results of the statistical comparisons reveal that the reconstructions at 10X are significantly different from the original data. Hence, 10X is considered as the failing point of the implementation.

As demonstrated, the implemented reconstruction method is able to generate metabolite maps similar to the original case. The metabolite maps generated using MRSI hold diagnostic and prognostic significance and the reconstruction preserves this information content faithfully. The high standard deviation in the metabolite intensities in our original data sets (1X), even normal brain, results inherently from the placement of the acquisition grid over the entire brain including the CSF (figures 2 and 3, 1X). Apart from visual inspection of the maps, the one-way ANOVA allow comparison of information content at a given location between fully sampled and CS reconstructed under-sampled data at various accelerations. The results of our approach also show that the reconstructions do not cause a change in these biomarkers like CNI and choline to citrate ratio. Therefore the reconstruction also maintains fidelity in such derived parameters as well. The statistical analyses also indicate that the reconstructions at 5X are similar to the original and the differences are statistically insignificant. However, at 10X the reconstructions show increased error and differences in the biomarker values. On the other hand the RMSE values computed on the reconstructed time domain data for these datasets

remain below 0.05 for accelerations up to 10X. Given that the original data sets were normalized before under-sampling, this reflects an error of below 5% for the reconstructions up to 10X. Conversion of acquired MRSI time domain data to metabolite information is a complicated process involving many user-chosen steps, which can potentially influence the appearance of final metabolite maps. Minimal post-processing of the original and CS-reconstructed data allows us to evaluate the fidelity of the reconstruction objectively but it is possible that the differences observed in the maps at higher accelerations may result from differences in the automated global phase correction. Looking at the trends in metabolite map intensity, for the brain data it was observed that the intensity goes up with acceleration factor, where as in the prostate case, the intensity goes down with acceleration factor. Deviations in either direction are possible based on various factors such as the regularization parameters, grid size and signal-to-noise ratio of the sampled k-space, therefore, this is not a trend, which is being proposed. For a given set of regularization parameters and acceleration factor, optimization routines result in increased error with increased acceleration as has been noticed by increasing RMSE value. Thus, the estimates of the concentrations tend to move further away from the original as acceleration is increased. From the perspective of applicability of the proposed methodology I am re-assured by the observation that the deviations in intensity remain monotonic functions of acceleration (i.e either increasing or decreasing on increasing under-sampling) and the RMSE remains small even at 10X. Thus further reduction in imaging time is possible in most fast spectroscopic imaging sequences by incorporation of compressed sensing methodology. It has been shown that under-sampling in increased dimensions allows for more efficient exploitation of inherent sparsity and results in improved reconstructions for compressed sensing (16). For MRSI data, the sparsity in the spectral dimension exceeds that in the spatial dimensions alone. Obtaining randomly sampled data in the phase encode as well as time dimension requires complex pulse sequences involving fast switching gradients. We have focused here on accelerating conventional MRSI acquisition protocols that are routinely available in the clinic but the application is not limited to these as discussed above.

An important concern for the application of any new reconstruction technique to spectroscopic imaging is the effect on the point-spread function (PSF), and the related bleed-through of information from one spatial location to another. The nature of the PSF and the transform point spread function (TPSF) for compressed sensing in MRI has been discussed in detail by Lustig*et al.* (16). The TPSF for the 3DFT case described therein is analogous to our 2D MRSI case with the temporal (FID) data being the dimension that is completely acquired as analogous to the readout direction in addition to 2 spatial phase encode directions. Theadvantage with compressed sensing is that the incoherent sampling avoids aliasing artifacts (such as seen in EPI/EPSI)(16) and the net effect is a noise-like scatter of intensities all over the field-of-view as opposed to a coherent broadening of the PSF and corresponding bleed-through of information into neighboring voxels.

A limitation of the current study is that it was performed retrospectively on clinical data acquired previously. While retrospective reconstruction is an important first step to determine the feasibility of our approach, a necessary follow-up step would be prospective studies on healthy volunteers where the proposed under-sampling scheme is implemented on clinical scanners and data acquired, reconstructed and compared at various under-sampling factors. Other directions for improvement could be extension to 3D MRSI and the design of new reconstruction routines to exploit sparsity in the spectral dimension along with spatial sparsity and achieve even higher acceleration, particularly for 3D MRSI.

In summary, the results shown indicate insignificant loss of information for an acceleration of up to 5X, which translates to a saving of up to 80% of acquisition time. This would potentially enable increased use of MRSI protocols in the clinic.Acceleration obtained using this approach could be extended for MRSI data of other organs (such as the breast).Alternatively the reduced acquisition time per acquisition could also be used to acquire spectra with harder-to-detect metabolites like glycine (52), through increased averaging.

CHAPTER 4

CS DCE-MRI

Dynamic contrast enhanced (DCE) magnetic resonance imaging (MRI) is an imaging method that provides critical information about the physiology of microcirculation and therefore has become a valuable clinical tool for cancer diagnosis. Since DCE involves imaging of the microcirculation, it is essential to accomplish increased spatial and temporal resolution. It is also well established that high temporal resolution and/or spatial resolution is required for accurate estimation of the pharmacokinetic parameters. This has resulted in fast imaging becoming a prerequisite for such studies. In this chapter, I investigate the efficacy of two such fast imaging methods: conventional keyhole imaging and CS based imaging as applied to DCE, retrospectively. The key-hole approach is one of the simplest and most straight forward approaches among the above mentioned methods to accelerate DCE-MRI while CS based reconstruction of DCE-MRI is a new approach. The goal of this study is to quantify and compare the effect of increasing accelerations on the accuracy of extracted physiological parameters using these two approaches. I explore three variants of each of these two approaches for comparison with the full k-space reconstruction with respect to data quality indicated by RMSE and pharmacokinetic parameters K_{trans} and v_e.

4.1 DCE-MRI

4.1.1 Introduction

Dynamic contrast enhanced MRI (DCE-MRI) has been shown to provide critical information about tumor microvasculature and is sensitive to vascular permeability and interstitial space fraction (53). DCE-MRI allows significantly earlier assessment of changes within tumors than that achieved by measuring anatomical tumor volume (54-55). Hence, DCE-

MRI can be used as an effective diagnostic tool and is a prognostic indicator of cancer progression and tumor response to therapy. DCE-MRI involves acquisition of images of tissues over a length of time before and after the injection of a contrast agent. The changes in signal intensity resulting from the wash-in, extravasation and wash out of the contrast agent can be related to tissue and vascular properties.

4.1.2 Significance of pharmacokinetic parameters

DCE-MRI allows estimation of pharmacokinetic parameters of the contrast agent by utilizing the multi-compartment model for microcirculation. This model has three compartments: microvasculature, the interstitial or extravascular-extracellular space (EES), and the intracellular space (56). This model can be reduced to a two compartment form as there is no intracellular uptake of conventional small-molecular MR contrast agents such as Magnevist™ or Omniscan™ (56). By knowing the concentration of the contrast agent in the blood and tissue, pharmacokinetic parameters like the contrast agent extravasation rate (K^{trans}) and the EES volume fraction (v_e) can be determined. A third parameter, k_{ep},is the ratio of K^{trans} to v_e and it depicts the rate of exchange of the contrast agent to the vasculature.

4.1.3 Role of spatial and temporal resolution in DCE-MRI

Extraction of pharmacokinetic parameters requires moderate to high temporal resolution (56) in DCE-MRI experiments. Spatial resolution plays a significant role as well in a DCE experiment in determining the morphology of the tumor being examined (57). Increased spatial resolution is also a requisite to minimize errors arising due to the inherent heterogeneity in tumor vasculature, which manifests itself at the macroscopic and microscopic level (58). Although this error cannot be completely eliminated regardless of MR resolution, increased spatial resolution would limit the effect of such an error. These two requirements are conventionally in direct conflict and accomplishment of high temporal resolution at a given spatial resolution requires reduction in acquisition time.

4.1.4 Techniques available to accelerate DCE-MRI

There are several approaches to accelerate DCE acquisitions, which have been increasingly used in the recent past. One of these techniques is parallel imaging. This is a robust technique for achieving high temporal and spatial resolution (14,59). However, the cost of this technique is significantly high due to the requirement of advanced hardware(60).

Another technique called the k-t (k-space temporal) broad-use linear acquisition speed-up technique (BLAST) (61) and k-t simultaneous acquisition of spatial harmonics (SENSE)(61) has been used to accelerate DCE-MRI acquisitions. These techniques incorporate parallel imaging with exploiting the spatio-temporal correlations in dynamic MRI acquisitions like DCE and have been also applied to cine-MRI. Techniques based on the k-t technique like the k-t FOCUSS (62) have also been used for DCE-MRI applications. However, these techniques involve the use of training sets and require the spatio-temporal correlations to be accurately captured by the training scan. Studies comparing the k-t BLAST and compressive sensing techniques have been performed(63) and it has been shown that CS based reconstructions resulted in improved temporal fidelity as compared to k-t BLAST.

4.1.5 Keyhole imaging

A popular conventional acceleration scheme is the “key-hole” imaging technique (64) which is a simple and effective approach developed for dynamic imaging applications to accomplish higher temporal resolution at given spatial resolution. Key-hole imaging utilizes the principle that, in a DCE experiment, the changes in image intensity in successive temporal points post-contrast injection occur in the low spatial frequency components while the high spatial frequency components remain relatively unchanged. Therefore, only low spatial frequency components are acquired during the post-contrast scanning thus saving time. The key-hole model can be described as follows:

$$S_{pre}(k) = L_{pre}(k) + H_{pre}(k) \qquad [4.1a]$$

$$S_{post}(k) = L_{post}(k) + H_{pre}(k) \qquad [4.1b]$$

where, $S_{pre}(k)$ is the acquired k-space of the pre-contrast case described as a function of k-space variable k (spatial frequency), consisting of the low frequency components $L_{pre}(k)$ and high frequency components $H_{pre}(k)$; $S_{post}(k)$ is the "assembled" k-space, post-contrast injection, comprising of the acquired low frequency components $L_{post}(k)$ and the high frequency components $H_{pre}(k)$ from the pre-contrast acquisition. Not acquiring the high frequency components during the post-contrast acquisitions helps increase temporal resolution, at least by reducing the number of phase-encodes. The high spatial frequency components from the pre-contrast image are then appended to the low frequency components post-acquisition to obtain dynamic post-contrast images. Conventional key-hole imaging has been further improved with the use of singular value decomposition and its variants(65) which involve the use of classifying the spatial frequencies into high, medium and low components as opposed to only high and low spatial frequency components in the conventional case. It has been also shown that the performance of the conventional key-hole approaches can be improved with the use of constrained image reconstructions and related methods as opposed to data substitution (66-69).

4.2 CS for DCE-MRI

4.2.1 Feasibility of CS for DCE-MRI

Another approach to accelerate DCE acquisition is by the use of CS. CS-based reconstruction of DCE-MRI has been recently demonstrated (70-72). The DCE data set is sparse in the finite difference transform along the time dimension and hence CS can be used to exploit redundancy in temporal correlations as well (70).

4.3 Methods

Existing DCE data sets of five 13762NF rat breast adenocarcinoma tumor-bearing Fisher rats were used to study the utility of each of the approaches described below. The data were obtained on a 4.7T horizontal bore Varian MR scanner. The data sets had dimensions of 64 X 64 and 64 images (4 pre and 60 post-contrast) were acquired with a spin-echo sequence (TR/TE = 200/11 ms) sequentially with a temporal resolution of 12 seconds. The contrast agent Omniscan^{TM}was intravenously administered through the tail vein at a dose of0.1 mmol/kg. Algorithm implementation and data processing was performed using MATLAB (The Mathworks Inc., MA).

4.3.1 Key-hole methods

Three different key-hole approaches classified on the shape of the sampling mask were implemented and are shown in figure 4.1. The first mask contained a square centered at the center of k-space (referred to as "*Key-hole")* while the second contained a number of phase-encode lines in the center of k-space (referred to as "*Key-lines"*).The third mask was based on the locations above a specific threshold of the absolute value of k-space of the pre-contrast image (referred to as "*Key-thresh"*). In each case, size of the mask was such that the ratio of the sum of the number of sampled pixels to the total number of pixels is closest to the under-sampling factor. For the study, these masks were generated for under-sampling factors of 0.5, 0.33, 0.25 and 0.2, which translates to acceleration in acquisition by factors of 2, 3, 4 and 5 respectively. The k-space of the pre-contrast images were averaged to obtain the $H_{pre}(k)$ component. The reconstruction for each case was compared with the full k-space reconstruction quantified by RMSE. Thus, RMSE values were calculated for each reconstruction approach implemented at 4 different acceleration factors for a total of 60 frames post-contrast in the acquisition. Each DCE data set was normalized to the pixel with highest intensity value to obtain a data range of 0 to 1. Since the pre-contrast images used for Key-

holereconstruction are identical to the original pre-contrast images (reconstruction of the complete k-space data), RMSE values were obtained for post-contrast images only.

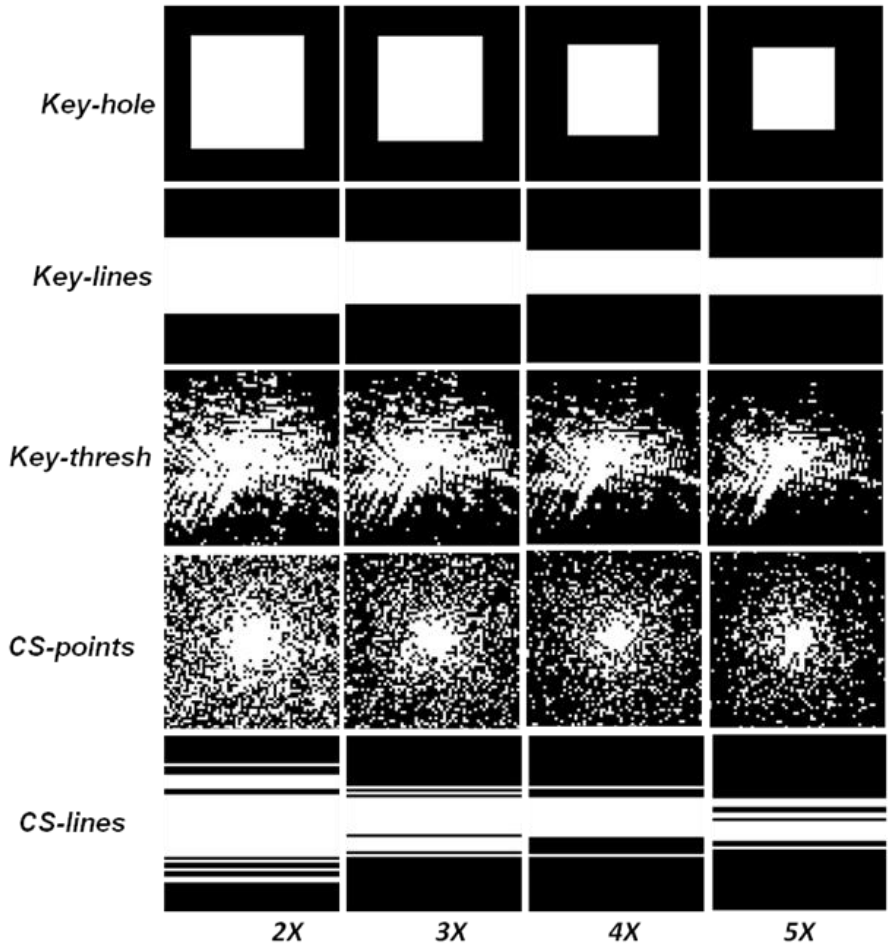

Figure 4.1 Representation of the sampling masks used for acceleration. White pixels represent a sampled location and black pixels represent an un-sampled location. The sampling masks for keyhole-based reconstruction are shown in the top panel: (a) Key-hole (conventional low pass acquisition) (b) Key-lines (acquisition of central phase encodes) (c) Key-thresh (acquisition of k-space points that satisfy a threshold criterion on the pre-contrast images). The sampling masks for compressed sensing based reconstruction are shown in the bottom panel: (d) CS-points (variable-density pseudo-random k-space points) (e) CS-lines (variable-density pseudo-random phase encodes). The third sampling mask for compressed sensing based reconstruction, CS-thresh, is same as (c) and is not shown separately here.

4.3.2 CS methods

Compressed sensing based reconstructions were performed based on 3 different masks. The first mask (referred to as "*CS-points"*) involved the use of points in k-space with a high density weighting at the center of k-space based on picking random samples weighted by a 2D probability density function resulting in more samples in the center of k-space than those at the edges (16). The extent of the fully sampled center of the chosen probability density function was dependent on the inverse of the acceleration factor, i.e. smaller fully sampled region for higher acceleration. The second mask involved similar choice of random phase-encode lines (referred to as "*CS-lines"*). The third mask was generated based on thresholding the absolute value of k-space of the pre-contrast image (referred to as "*CS-thresh"*). The CS-thresh under-sampling mask is same as the Key-thresh mask (Figure 4.1, row 3) but the difference in the two approaches is in the way the DCE data were reconstructed. The under-sampling factors used for the compressed sensing based methods were the same as those used for the Key-hole methods. Each DCE data set was normalized to the pixel with highest intensity value before reconstruction as was done in the Key-hole methods. A cost function for a convex optimization problem was constructed as shown below (70).

$$\epsilon(I_{diff}) = ||FI_{diff} - y_{diff}||_2 + \lambda_{L1}||WI_{diff}||_1 + \lambda_{TV}(I_{diff}) \qquad [4.2]$$

where, I_{diff} is the desired difference image between the reference image and the intermediate image, F is the Fourier transform operator, W is the wavelet transform operator, $||.||_1$ and $||.||_2$ are the L_1 and L_2 norm operators respectively, λ_{L1} and $\lambda_{TV}$are regularization parameters for the L_1 term and total variation (TV) term respectively, and Є is the value of the cost function. The image reconstruction for each case was performed by minimizing the above cost function using a nonlinear conjugate gradient approach. Regularization parameters λ_{L1} *and* λ_{TV}were set to0.005 and 0.01, respectively. As in the case of the key-hole methods, the reconstructions based on compressed sensing were compared with the full k-space reconstruction using RMSE as the metric. A mean value of RMSE was calculated for the data immediately following contrast

injection for each under-sampling factor and method based on the 5 data sets as performed in the case of the Key-hole methods.

4.3.3 Segmentation of region(s) of interest (ROI)

The original and reconstructed DCE data sets were subjected to a semi-automatic segmentation procedure to delineate areas of muscle, well-perfused and poorly-perfused regions as shown for a representative data set in figure 4.2. I marked the periphery of the tumor region based on the T_2-wieghted image (figure 4.2a) and the pre (figure 4.2b) and post-contrast (figure 4.2c) MR anatomical image of the original reconstruction. The muscle region was delineated using a user selected area outside the periphery of the tumor region. The area within the periphery of the tumor region was segmented automatically into well- and poorly-perfused regions using the following criteria: a particular pixel would be classified as well-perfused region if the 3rd post-contrast image (36 seconds post contrast injection) showed an enhancement of greater than 50% with respect to the average pre-contrast image. The poorly-perfused region was defined here as the result of the subtraction of the well-perfused region from the total area within the periphery of the contrast enhanced region.

4.3.4 Pharmacokinetic analysis

The signal intensity time course was converted to corresponding concentrations of the contrast agent concentration information was then utilized to generate maps of the pharmacokinetic parameters of $K^{trans}$and v_e based on a reference region method of quantification of DCE pharmacokinetic parameters by Yankeelov et al. (73) These maps were generated for the complete k-space reconstruction method, key-hole imaging methods as well as the reconstructions based on compressive sensing. The implementation for calculating the two pharmacokinetic parameters assigned limits to the range of each that were physiologically relevant (v_e, [0 0.8], K^{trans} [0 0.8]) and fit values of pixels outside this range were not considered for further analyses (46). A comparison of these parametric maps for each case was performed

to evaluate the efficacy of each reconstruction approach for DCE data acquisition. The full k-space reconstruction was the reference standard with which the accelerated reconstructions were compared.

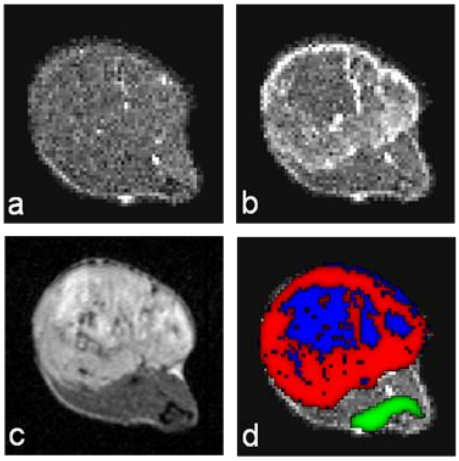

Figure 4.2 Image segmentation for a representative data set. T_1-weighted (a) pre and (b) post-contrast MR images and (c) T_2 weighted images are used to identify the (d) muscle (green), well-perfused (red) and poorly-perfused (blue) regions in the images for analysis.

4.3.5 Statistical analyses

The pharmacokinetic parameters (K^{trans} and v_e) calculated using different reconstruction methods for all the data sets were grouped together for each acceleration factor and compared pixel by pixel with the complete k-space reconstruction. A paired t-test was performed on the pharmacokinetic maps generated from complete k-space as the control and the six reconstruction methods at the 4 under-sampling factors to evaluate the fidelity of the reconstructed data. The null hypothesis was that there were no statistically significant differences between the full k-space and the reconstructed data and a p-value greater than 0.05

was considered to be a non-significant difference between a particular reconstruction method and the control.

4.3.6 Prospective study

A prospective study based on the implementations on the retrospective analysis was performed on a horizontal bore 4.7T Varian scanner to image a13762NF rat breast adenocarcinoma tumor-bearing Fisher rat. The data set had dimensions of 64 X 64 X 64 and 65 temporal samples (5 pre-contrast and 60 post-contrast) was acquired with a undersampledgradient-echo sequence (TR/TE = 10/1.02ms, nominal flip angle 35^0) sequentially with a temporal resolution of ~11 seconds and a FOV of 5cm in each direction. The undersampling of the sequence was achieved by feeding in an external phase encode (PE) table with 32 phase encode values for each of the 2 phase encode directions used in the sequence while the read-out direction (kx) was completely sampled. Thus, an undersampling factor of 2 was achieved in each direction resulting in a total acceleration of 4, hence reducing the temporal resolution for the acquisition from ~44 seconds to ~11 seconds. The phase encode values chosen from the set of 0 to 63 were: 4, 8, 12, 16, 18, 20, 22, 24, 25, 26, 27, 28, 29, 30, 31, 32, 33, 34, 35, 36, 37,38, 39, 40, 41, 43, 45, 47, 49, 53, 57 and 61. The same value of phase encodes were used for both directions resulting in a undersampling mask shown in figure 4.3 where the location of the red bars denote a sampled location in the ky-kz plane while the height of the bar represents the fully sampled read-out direction. These values of phase encodes resulted in a varying density sampling mask with increased sampling in the center with the sampling density decreasing towards the edges. This sequence was compiled on the scanner and stored. The contrast agent Omniscan^{TM}was intravenously administered through the tail vein at a dose of0.1 mmol/kg (graduate student Praveen K. Gulaka performed the IV injection).

The reconstruction scheme detailed in section 4.3.2 was extended to the 3D case and was used to reconstruct the volumes at the different time points. The segmentation analyses

described in section 4.3.3 was employed on the central slice of the volumes at all time points to visualize the time-intensity course of the muscle, well-perfused and poorly-perfused regions.

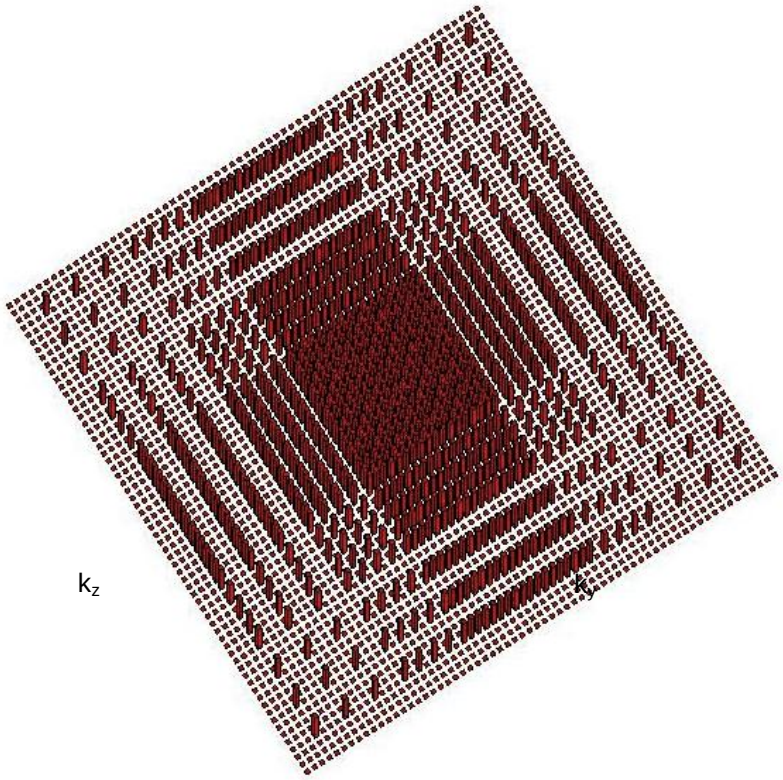

Figure 4.3 Undersampling mask used for the modified ge3d sequence implemented on the Varian 4.7T scanner. The image shows the undersampled phase encode values (locations of the red bars) for the ky-kzaxes while the fully sampled read-out direction is represented by the height of the bar.

4.4 Results

4.4.1 Data quality and errors of reconstructions

The image panel in figure 4.4 shows the quality of reconstruction of a representative DCE data set at 36 sec post contrast injection using the 6 different approaches at acceleration factors of 2X, 3X, 4X and 5X. At acceleration factors of 4X and 5X, some signal loss at regions in the image (e.g. center left) can be observed in the non-threshold based methods. This can be attributed to the fact that given the spread of spatial frequencies in the object, the smaller mask size of the Key-hole, Key-lines, CS-points and CS-lines mask is likely to miss important spatial frequencies. In all methods a blurring is observed with increasing acceleration.

The time course of the RMSE values over all the 5 data sets reconstructed using the 6 approaches at the 4 acceleration factors are depicted in figure 4.5 using a novel image based representation. In this representation, the RMSE values are designated color scale intensities while the x and y-axes represent frames post-injection (time) and reconstruction method/acceleration factor, respectively. This allows assessing the fidelity of reconstruction for the multi-dimensional data set in condensed manner. Some observations can be easily made from figure 4.5. Firstly, for every technique, the reconstruction error increases with increasing acceleration. This is to be expected for the key-hole methods as more of the intermediate frequency components (which could change in content as the contrast agent washes in and out) are retained from the pre-contrast image. Even for the CS-based methods, this is not unexpected as there is increasing reliance on the iterative reconstruction process to estimate the missing k-space values as acceleration increases. Overall, it can be observed that each CS-method consistently shows lower RMSE values than the corresponding key-hole method for any given acceleration (e.g. Key-lines vs CS-lines or Key-thresh vs CS-thresh at 4X). This is true regardless of the segmented region being analyzed. Since keyhole imaging involves acquiring of merely low frequency components, loss of dynamic edge information could also contribute to increased errors in reconstructions along with errors due to truncation effects.

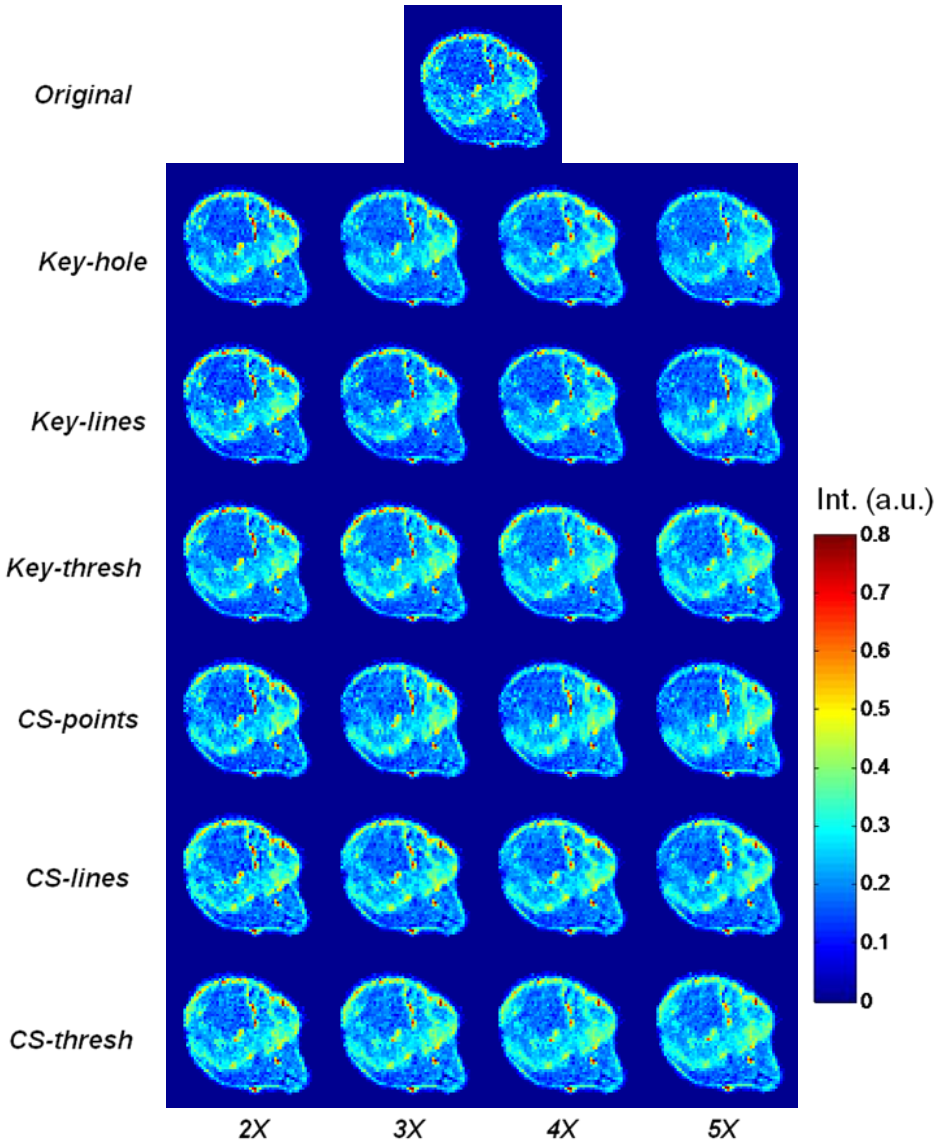

Figure 4.4 Reconstruction of DCE data sets using the 6 acceleration approaches described. Top image depicts the full k-space reconstruction and successive rows represent contrast enhanced image (36 seconds after injection) using keyhole-based reconstruction (Key-hole, Key-lines and Key-thresh) and compressive sensing–based reconstruction (CS-points, CS-lines and CS-thresh) at acceleration factors of 2X, 3X, 4X and 5X, respectively.

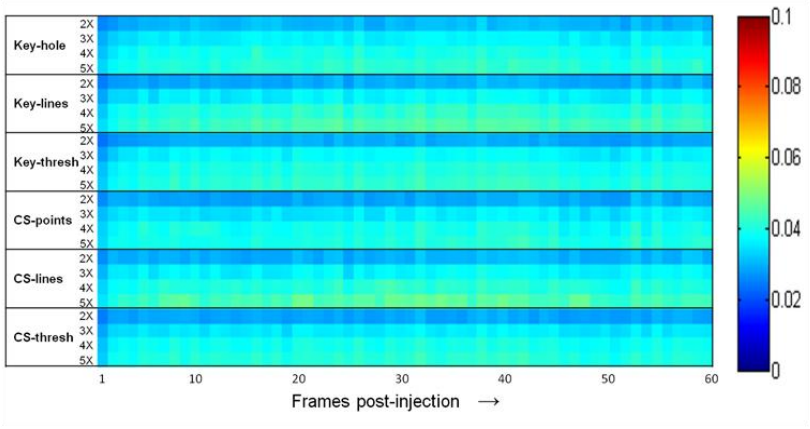

(a)

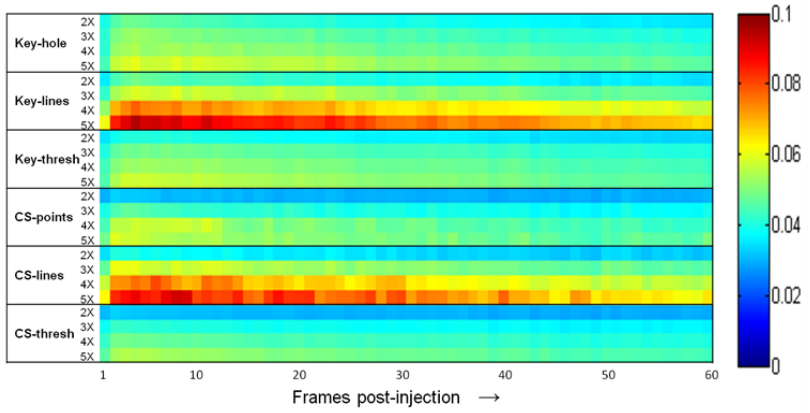

(b)

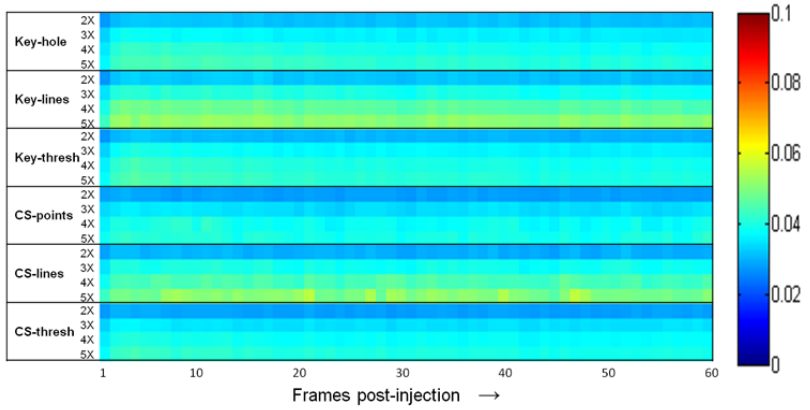

(c)

Figure 4.5 A new, image-based representation of RMSE values for the 6 acceleration approaches described (Key-hole, Key-lines, Key-thresh, CS-points, CS-lines and CS-thresh) at various accelerations (2X, 3X, 4X and 5X) for the segmented a) muscle, (b) well-perfused and (c) poorly-perfused regions.

The two phase-encode lines based methods, Key-lines and CS-lines, show the highest error particularly at higher accelerations, presumably due to consistently lower sampling in the phase-encode direction than other masks at the same overall under-sampling factor. The two methods based on a priori information, Key-thresh and CS-thresh, show the least RMSE with CS-thresh performing better at any given under-sampling factor. The better performance of CS-thresh is due to the overall de-noising and reduction of artifacts resulting from the iterative reconstruction process, which is the only difference between these two approaches (which use the same mask).Among the keyhole methods, it can be noted that Key-thresh mask performs consistently better than the other two methods at any given acceleration. This could be due to dynamic intermediate frequencies not being captured by the Key-lines and Key-hole masks. The compressed sensing methods showed a similar and consistent pattern of results irrespective of the acceleration factor. The CS-thresh mask always performed the best followed by CS-points and CS-lines mask based reconstructions. The CS-points mask with density compensation has the most randomly distributed sampling scheme and is also constrained to have samples throughout the mask thereby reducing the sampling density at the center. The CS-lines approach is closer to the CS-points case but has lower sampling in the read-out direction as seen in figure 4.1. Since most of the significant changes do occur in the low and intermediate frequencies, CS-points is better able to capture these changes in the read-out direction than CS-lines.

Comparing the differences in errors in the three segmented regions yields expected results. In case of the muscle (Figure 4.5a) and the poorly-perfused (Figure 4.5b) regions, it can be observed that all the 6 methods show high fidelity with errors under 5%. Thewell-perfused (Figure 4.5c) region shows highest errors with those approaching 10% at higher acceleration in the Key-lines and CS-lines methods. This is a result of the well-perfused region being at the periphery of the tumor and contributing the most to dynamic changes in the spatial frequency information. As the perfusion of contrast agent induces high changes in intensity near the edge, new spatial frequencies are needed to account for the “new” edges. In general, these

frequencies may be missed by under-sampling and thus contributing to higher errors in this segmented region.

4.4.2 Pharmacokinetic and statistical analyses

The maps of two fundamental parameters of K^{trans} and v_e for a representative data set for the implemented acceleration factors and approaches are shown in figures 4.6 and 4.7, respectively. Qualitatively, the maps at 2X show similarity with the full reconstruction in terms of values and distribution for both key-hole and CS. With increasing acceleration, artifactual decreases in parameter values mirror the signal intensity artifacts in the reconstructed image intensities (figure 4.4). This is particularly evident in the v_e maps (figure 4.7). In general the maps show a decreasing trend in parameter values as a function of acceleration with the CS approaches showing a smaller variation. The results of the statistical analyses of the 2 pharmacokinetic parameters (for n= 5 animals) are shown in tables 4.1 and 4.2. Surprisingly, the deviations in mean K^{trans} and v_e of the accelerated data sets compared to the original data do not match the trends observed in the RMSE values. This is not surprising as there is no linear relationship between the intensity variations of the time course data and the fit parameters K^{trans} and v_e.The fit parameter values are also affected by signal/noise ratio which is affected by the total variation term in equation 4.2. Also a high amount of variation in K^{trans} and v_e was observed in the original data which somewhat confounds statistical comparisons. Only one value in tables 4.1 and 4.2 was statistically different ($p<0.05$) compared to the original (ve for the poorly-perfused region at 2X acceleration using the Key-lines sampling). In general it was observed that the CS-based methods tend to overestimate K^{trans} and v_e irrespective of sub-region (poorly perfused or well-perfused) while the key-hole based methods underestimated K^{trans} in the well perfused region. In either category (key-hole or CS) the threshold based technique performed better than its counterpart for v_e estimation. CS methods actually performed better at 5X than at 2X, with the CS-thresh method displaying least variation as a function of acceleration.

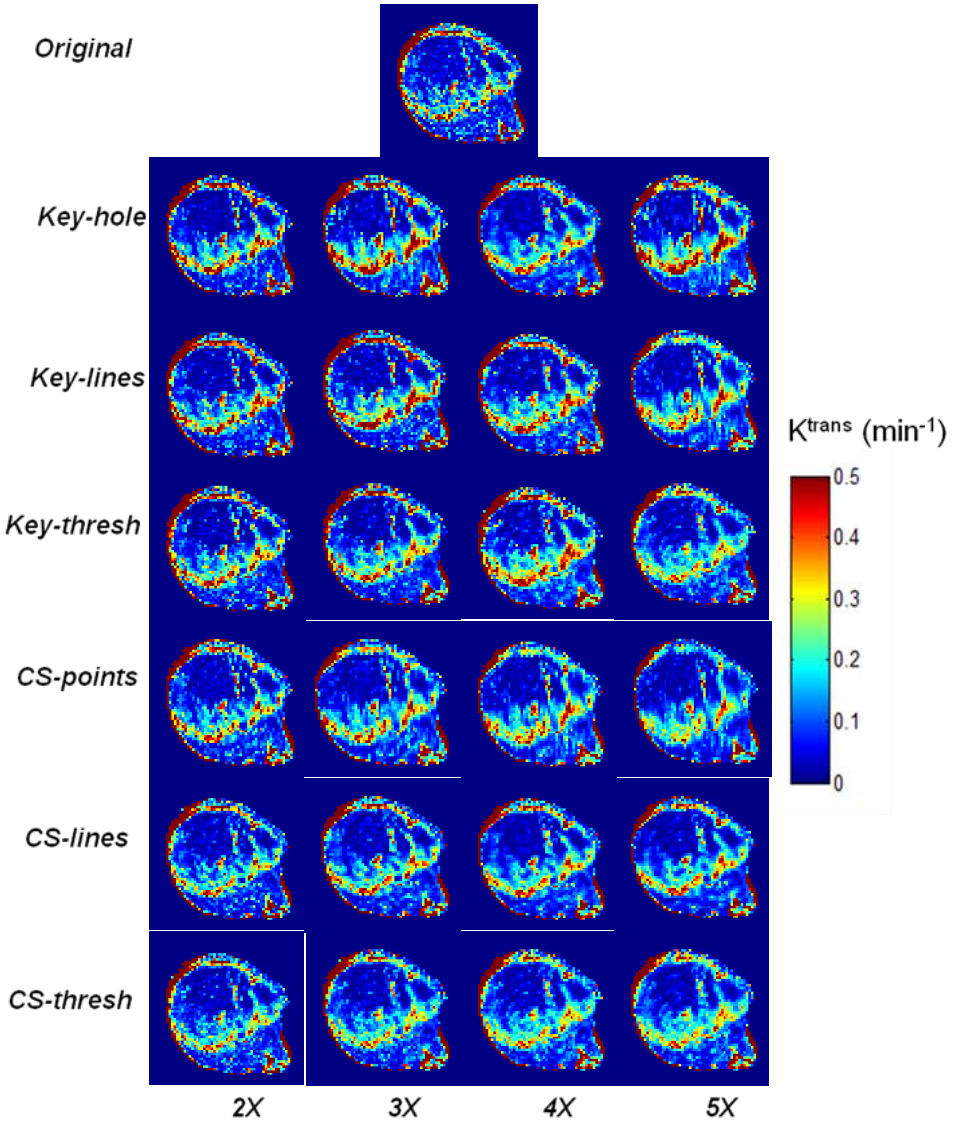

Figure 4.6 Calculated K^{trans} maps using the data reconstructed from the six acceleration approaches described. Top image depicts the K^{trans} map reconstructed from full k-space reconstruction and successive rows represent K^{trans} maps using keyhole-based reconstruction (Key-hole, Key-lines and Key-thresh) and compressive sensing–based reconstruction (CS-points, CS-lines and CS-thresh) at acceleration factors of 2X, 3X, 4X and 5X, respectively.

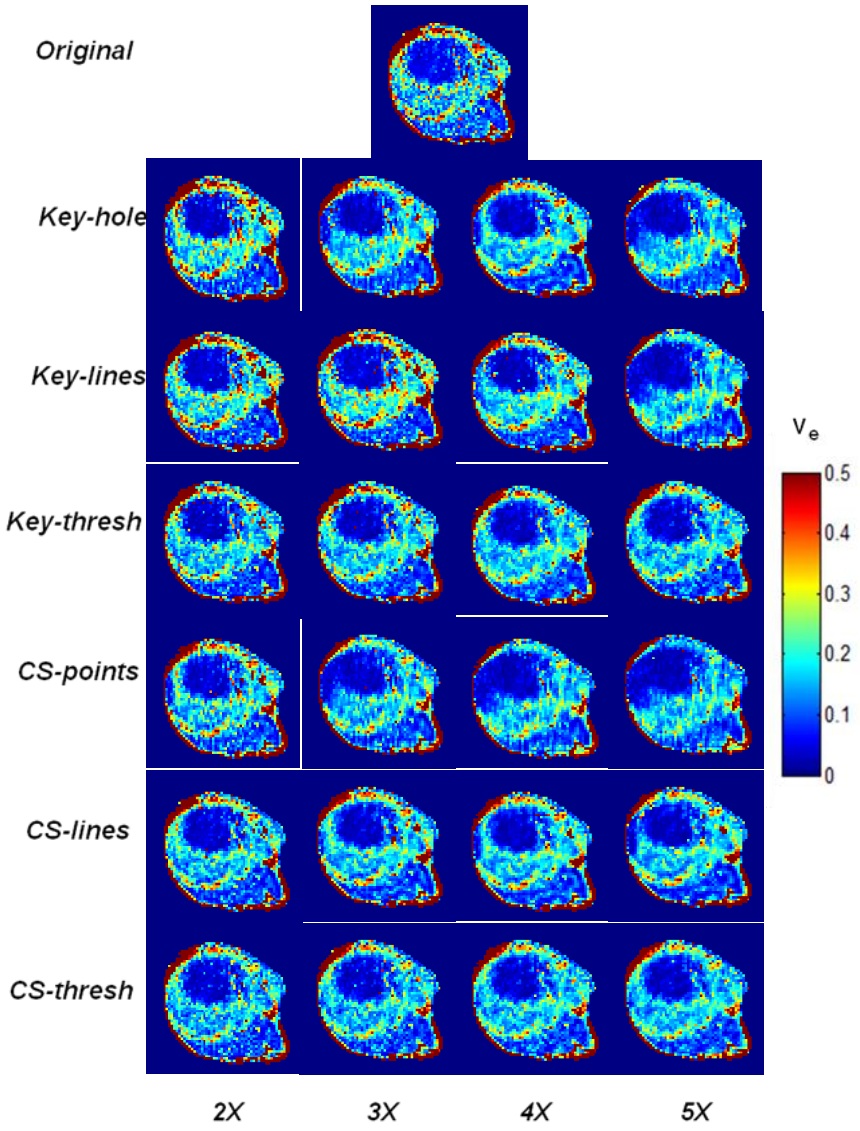

Figure 4.7 Calculated K^{trans} maps using the data reconstructed from the six acceleration approaches described. Top image depicts the K^{trans} map reconstructed from full k-space reconstruction and successive rows represent K^{trans} maps using keyhole-based reconstruction (Key-hole, Key-lines and Key-thresh) and compressive sensing–based reconstruction (CS-points, CS-lines and CS-thresh) at acceleration factors of 2X, 3X, 4X and 5X, respectively.

Table 4.1 Comparisons of the K^{trans} maps between the six reconstruction methods at 4 different undersampling factors with the maps obtained using complete k-space reconstruction. The table lists the mean K^{trans} (min^{-1}) ± standard deviation (n=5 animals). The mean K^{trans} values for the well-perfused and the poorly-perfused regions of the original data were 0.18 ± 0.12 min^{-1} and 0.09 ± 0.05 min^{-1}, respectively.

		K^{trans} (min^{-1})					
		Key-hole	**Key-lines**	**Key-thresh**	**CS-points**	**CS-lines**	**CS-thresh**
well-perfused	**2X**	0.17 ± 0.11	0.17 ± 0.11	0.17 ± 0.10	0.21 ± 0.16	0.20 ± 0.14	0.21 ± 0.15
	3X	0.18 ± 0.12	0.17 ± 0.11	0.17 ± 0.11	0.21 ± 0.15	0.21 ± 0.15	0.21 ± 0.16
	4X	0.18 ± 0.11	0.16 ± 0.10	0.17 ± 0.10	0.18 ± 0.12	0.19 ± 0.13	0.20 ± 0.15
	5X	0.17 ± 0.11	0.14 ± 0.08	0.16 ± 0.10	0.19 ± 0.14	0.17 ± 0.13	0.21 ± 0.15
poorly-perfused	**2X**	0.09 ± 0.06	0.09 ± 0.06	0.09 ± 0.06	0.10 ± 0.07	0.10 ± 0.07	0.09 ± 0.06
	3X	0.10 ± 0.08	0.09 ± 0.07	0.09 ± 0.06	0.10 ± 0.07	0.10 ± 0.07	0.10 ± 0.06
	4X	0.10 ± 0.08	0.10 ± 0.07	0.10± 0.07	0.09 ± 0.06	0.09 ± 0.06	0.10 ± 0.07
	5X	0.09 ± 0.07	0.09 ± 0.06	0.09 ± 0.06	0.09 ± 0.05	0.09 ± 0.06	0.10 ± 0.07

Table 4.2 Comparisons of the v_e maps between the six reconstruction methods at 4 different undersampling factors with the maps obtained using complete k-space reconstruction. The table lists the mean v_e ± standard deviation (n=5 animals). The mean v_e values for the well-perfused and the poorly-perfused regions of the original data were 0.21 ± 0.08 and 0.16 ± 0.04, respectively.

		v_e					
		Key-hole	**Key-lines**	**Key-thresh**	**CS-points**	**CS-lines**	**CS-thresh**
well-perfused	**2X**	0.22 ± 0.07	0.22 ± 0.08	0.20 ± 0.06	0.25 ± 0.10	0.26 ± 0.13	0.22 ± 0.08
	3X	0.21 ± 0.08	0.25 ± 0.12	0.19 ± 0.06	0.24 ± 0.12	0.23 ± 0.15	0.21 ± 0.08
	4X	0.20 ± 0.08	0.23 ± 0.19	0.19 ± 0.06	0.22 ± 0.10	0.26 ± 0.16	0.20 ± 0.08
	5X	0.20 ± 0.07	0.20 ± 0.11	0.18 ± 0.07	0.21 ± 0.10	0.25 ± 0.16	0.20 ± 0.08
poorly-perfused	**2X**	0.18 ± 0.02	0.20 ± 0.03	0.16 ± 0.01	0.22 ± 0.05	0.24 ± 0.08	0.20 ± 0.03
	3X	0.18 ± 0.02	0.24 ± 0.10	0.16 ± 0.03	0.21 ± 0.08	0.26 ± 0.12	0.19 ± 0.02
	4X	0.17 ± 0.02	0.20 ± 0.11	0.16 ± 0.01	0.20 ± 0.06	0.25 ± 0.14	0.19 ± 0.02
	5X	0.17 ± 0.02	0.18 ± 0.10	0.16 ± 0.02	0.18 ± 0.06	0.23 ± 0.14	0.19 ± 0.02

4.4.3 Prospective study

Figures 4.8, 4.9 and 4.10 show the results of the prospective study. The minimum energy reconstruction with density compensation for the undersampled scheme for the central slices in the 3 orientations is shown in figure 4.8 (a) and the corresponding iterative reconstructions are shown in figure 4.8 (b). It can be noticed from 4.9 (a) that ghosting exists in the minimum energy reconstructions, which is suppressed in the reconstructed images. (All images are displayed between [0 0.75])

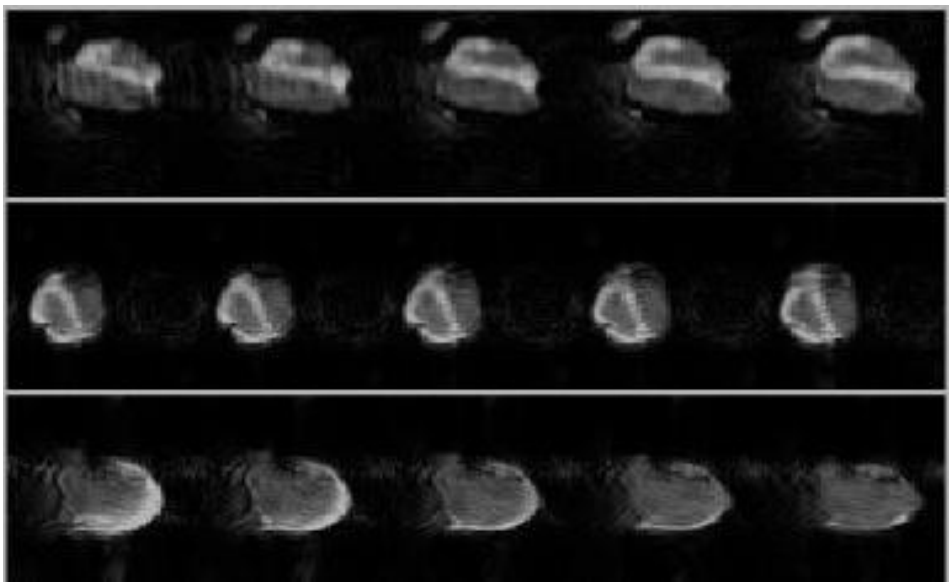

(a)

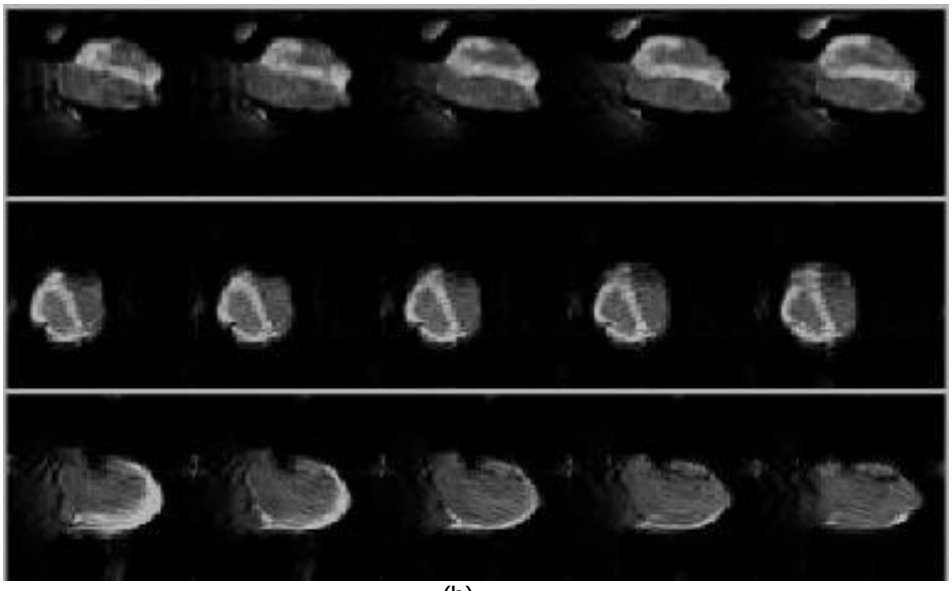

(b)

Figure 4.8 (a) The minimum energy reconstruction resulting from the undersampling scheme employed in the prospective study and (b) the results of the iterative reconstruction for the central slices in the 3 orientations.

Figure 4.9 shows images of the central slice acquired at the temporal points of 5, 6, 7, 8, 20 and 65 corresponding to 55, 66, 77, 88, 220 and 715 seconds from the start of the acquisition respectively, to depict the time course of the experiment. It can be seen that the contrast agent helps delineate the periphery of the tumor as can been noticed through the differences in the baseline image at time-point (frame) 5 and subsequent frames of 6, 7 and 8. The increase in intensity at frame 8 can also be visualized which decreases at frame 20 and reduces further at frame 65. This is reflected in the time-intensity course resulting from the segmentation procedure shown in figure 4.10. The three regions of the muscle (green), well-perfused (orange) and poorly-perfused (red) regions are shown in figure 4.10(a). The percentage change in intensity with respect to the mean baseline intensity has been computed and shown for each time frame in figure 4.10 (b). It can be noticed from figure 4.10(b) that the periphery has the highest enhancement as compared to the other 2 regions with the poorly-perfused region showing a higher enhancement than the muscle.

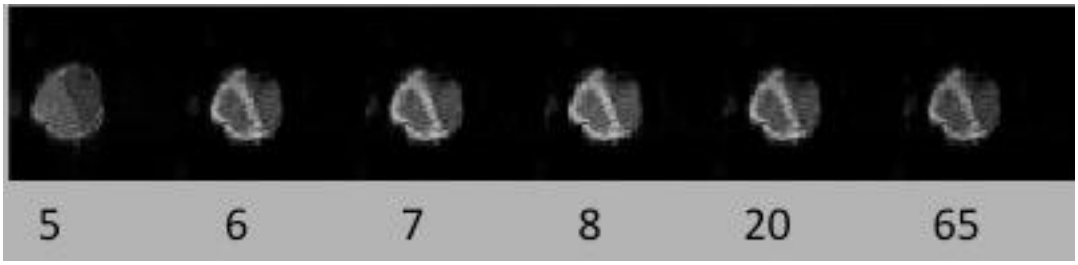

Figure 4.9 Time-course of the experiment depicted by the temporal frames of the central slice at baseline (frame 5), immediately post-contrast (frames 6,7, 8), an intermediate time point (frame 20) and the last time point (frame 65).

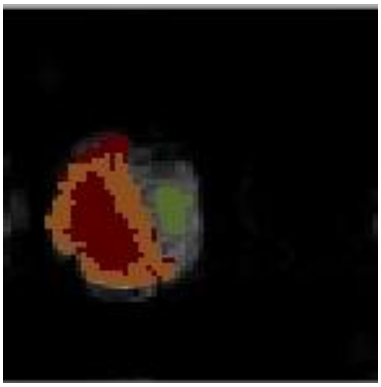

(a)

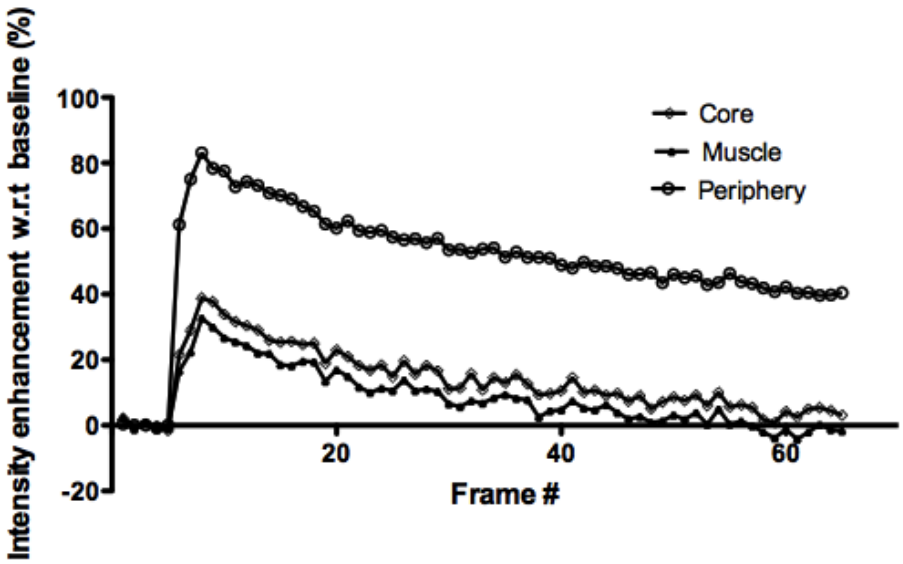

(b)

Figure 4.10 (a) The result of the segmentation procedure on the central slice showing the muscle (green), well-perfused (orange) and poorly-perfused (red) regions. (b) Intensity-time course for the three regions as a function of the temporal frames

4.5 Conclusions

It has been shown here and previously that DCE MRI can be reliably accelerated through methods like compressed sensing (70-72,74) and key-hole based reconstructions (75-76) to obtain increased spatial and/or temporal resolution. Comparing the two approaches with respect to data quality and calculation of pharmacokinetic parameters illuminate the advantages, disadvantages and utility of each. Each of these two types of reconstruction methods has unique advantages and disadvantages. As compressed sensing reconstruction is dependent on an iterative approximation, it is well tolerant to changes in structure of the object while it is being imaged, unlike the key-hole approaches which rely on the k-space of the pre-contrast image for edge (high frequency) information.Thus, in situations where there is significant dynamic change in structure (e.g. cardiac MRI) key-hole might not be optimal. Also, artifacts arising from phase errors may occur in key-hole imaging due to the 'stitching' of the low and high frequency components. However, the compressed sensing based reconstruction needs tuning of regularization parameters which is not the case with key-hole methods. Comparatively, Key-hole methods are easier to implement and relatively easy to reconstruct. CS-based approaches involve implementation of sophisticated pulse sequences in some cases but are comparatively more robust as shown by the quantification of errors for reconstruction and the statistical tests for the parametric maps. Acceleration factors of up to 5X can be achieved with implementation of the approaches described here. However, prospective implementation of some of these approaches is not straight forward. For instance, the thresholded mask for either the Key-hole approach or the compressed sensing would involve a pulse sequence which needs to sample k-space points in an asymmetric and discontinuous fashion.This implementation would not be practical. Alternatively, a real-time design of a variable density spiral k-space trajectory which would cover most of the points in k-space depicted by the sampling mask obtained immediately after the pre-contrast scan could be used to design the pulse sequence. Further optimization in k-space trajectory could be made with Bayesian experimental design(77). These approaches can be combined with hardware

basedacceleration for further reduction in acquisition time (78-80). In parallel with this effort(81), Smith et al. recently investigated the effect of retrospective CS-based acceleration (up to 4X) on the accuracy of extracted pharmacokinetic parameters from DCE MRI data obtained as part of pre-clinical and clinical studies(74,82). The under-sampling scheme used by them is identical to the CS-lines approach described here but the reconstruction algorithm used by them is different from this study. Nevertheless, they show similar trends in their data as seen in our study which is reassuring.

The prospective studies show the importance of undersampling in the DCE-MRI set-up. Acceleration enabled the acquisition of the tumor volume as opposed to the multi-slice acquisition which can be restrictive with respect to spatial coverage and hence information content. The undersampling scheme however does not possess incoherent sampling and hence results in ghosting artifacts as can be seen in figure 4.8(a). The undersampling scheme used has variable density but follows a specific pattern of undersampling.An undersampling scheme, which includes incoherence and variable density sampling, could be used to alleviate this issue.

In summary, I have demonstrated that an acceleration of up to 5X is possible with retention of fidelity of DCE-MRI pharmacokinetic parameters by use of compressive sensing. A sample prospective study has been shown to demonstrate the ease of implementation on a preclinical scanner using external phase encode tables. Further studies could use such methodology for prospective studies in combination with hardware-based acceleration to improve temporal/ spatial resolution in DCE-MRI studies or to improve signal/noise ratio for improved parameter estimation.

CHAPTER 5

CS SWIFT

5.1 SWIFT MRI

Sweep imaging with Fourier transformation (SWIFT) is a novel MR imaging technique which allows for fast, short T_2 sensitive MR imaging with reduced motion artifacts and reduced signal dynamic range (83). CS has been demonstrated as a viable technique to accelerate MR acquisition (16) and its application for SWIFT imaging has been detailed in this chapter. This has been demonstrated on a resolution phantom and 5 human knee data sets. The results of reconstruction are evaluated based on RMSE metric and segmentation of regions corresponding to the ligaments.

5.1.1. Introduction

Acquisition of MR signal is accomplished through RF excitation as described in section 1.1. The excitation has so far been performed in three different methods: continuous wave (CW) (2,84), stochastic (85) and pulsed NMR (86). SWIFT MRI is a combination of the three methods. It utilizes swept frequency for excitation as in the CW method but the signal is acquired in the time domain as in the pulsed method. SWIFT MRI uses principles derived from stochastic NMR to extract the desired signal from the acquired data. SWIFT involves excitation immediately followed by acquisition thereby resulting in a near-zero TE. This provides an opportunity to image objects that have a very short T_2^* component such as bone and connective tissues of the musculoskeletal system, macromolecules and quadrupolar nuclei like ^{39}K and ^{23}Na.

5.1.2. SWIFT pulse sequence and reconstruction

Figure 5.1 shows a simple cartoon of the SWIFT MRI pulse sequence (reproduced from (83)). The pulse sequence involves a series of RF pulses each lasting a time period T_p. Each pulse has N segments with each segment on during time τ_p followed by data collection after a time period of τ_a. The dwell time (dw) given by the time difference between two consecutive data measurements is shown in the figure 5.1(c).

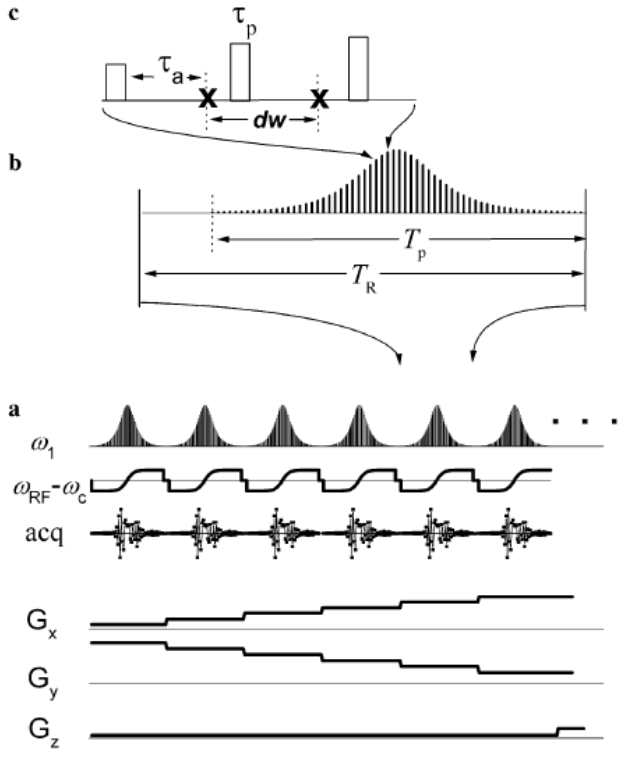

Figure 5.1 (reproduced from (83)): Cartoon depicting the (a) SWIFT pulse sequence, (b) magnified RF pulse and (c) closer look at the individual pulses to show the dwell time (dw)

Phase encoding is achieved in three directions by the application of the 3 gradients (G_x, G_y, G_z) as shown in the figure 5.1 which trace a 3D radial trajectory as shown in figure 5.2. The gradients also help in spoiling of the unwanted stimulated echoes during the change of direction for a new orientation. However, the signal acquired is weighted by the RF pulses. The total T_R is equivalent to the sum of T_p and the time required for gradient switching from one orientation to

the next. Reconstruction of SWIFT MR data can be accomplished by gridding (8) (as described in section 1.2.4.) followed by a correlation based correction to deconvolve the effect of RF weighting (83).Currently, exquisite 3D SWIFT images can be acquired within minutes but imaging dynamic changes in short T_2 species, such as T_2 exchange contrast agents, would require an even faster imaging scheme. CS is a viable technique to accelerate MR acquisition and can be utilized to speed up SWIFT acquisitions.

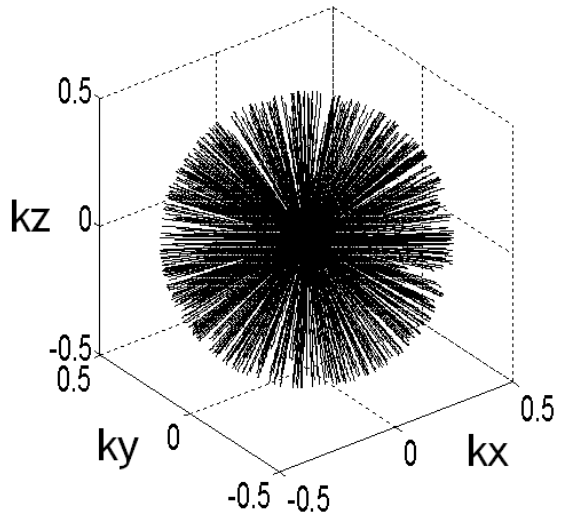

Figure 5.2 The resulting k-space trajectory of the shown SWIFT pulse sequence

A SWIFT derived pulse sequence to enable easier implementation is the Concurrent Dephasing and Excitation (CODE) sequence (87) which involves dephasing of the read-out gradient during RF excitation hence providing echo-times of up to 0.2ms and greater. Another important difference between these two sequences is that CODE data is acquired post excitation and as an asymmetric echo as compared to the FID acquisition of the SWIFT sequence. However, both sequences have a similar koosh-ball k-space trajectory and employ the read-out gradient during excitation(87).

5.2 CS for SWIFT MRI

CS could enable SWIFT imaging of dynamics of musculoskeletal system, breast DCE-MRI and neuroimaging among other applications that require increased resolutions and also for fast dynamic imaging of T_2 exchange contrast agents to obtain accurate pharmacokinetics.

5.2.1. Feasibility of CS for SWIFT MRI

It can be deduced from figure 5.1 that SWIFT MRI results in volume-based acquisitions. Since most anatomical features do not vary drastically for typical MR resolution, the simplest sparsity transform for the SWIFT MRI images is the 3D total variation norm (finite differences transform). This ensures that incoherent noise produced by the pseudo-random sampling pattern can be removed to recover the underlying object. Pseudo-random sampling for SWIFT MRI is straightforward as each spoke on the radial trajectory contains information related to the center of k-space. Unlike the conventional radial imaging scheme, SWIFT is a FID based acquisition and hence each spoke does not span the range of k-space values. However spokes can be easily chosen at random without concerns of losing SNR due to reduced sampling in the center but this has to be compensated during the reconstruction through sampling density correction as mentioned in section 1.2.4. The resulting gradient waveform would not be as smooth as the existing method shown in figure 5.1 but could be practically implemented without consequences of random jumps in k-space. The resulting data from such an undersampling scheme can be reconstructed via the NCG algorithm (section 2.2.3).

5.2.2. CS SWIFT MRI reconstruction

Reconstruction for CS SWIFT MRI can be cast as a convex optimization problem as detailed in section 2.2.3. The major difference would be the use of the 3D total variation norm as opposed to the 2D used in [2.3] where m is the desired SWIFT MR volume, ψ is the 3D TV

norm and the other terms being the same as described in [2.3]. Therefore, the unconstrained minimization problem can now be mathematically represented as shown in [5.1].

$$argmin_m ||F_u m - y||_2^2 + \lambda_{TV} TV_{3D}(m) \qquad [5.1]$$

The use of 3D wavelets would have resulted in increased sparsity in the reconstructions but was not chosen due to increased computational requirements.

5.3 Methods

The demonstration of CS SWIFT MRI was performed through application of the reconstruction on SWIFT data which consisted of a resolution phantom (Nuclear Associates, 76-903, Fluke Biomedical) and 5 human knee MRI volumes acquired using the CODE sequence. The MRI protocol was approved by the Institution Review Board of the University of Minnesota, MN. All data were acquired on a Siemens 3.0T Magnetom Trio. The phantom was acquired along 16,000 projections with 128 phase encodes, FOV = 40cm, TR = 4 ms resulting in a matrix size of 147 x 147 x 147. The total acquisition time was 74s. The projections were acquired in blocks of 500. Each block was defined using a sorted Halton ordering scheme, to encompass a random but uniformly distributed sampled set of projections encompassing the object. This phantom was chosen to evaluate the utility of the ability of the reconstruction to reproduce fine structure detail. In all the cases of *in vivo* data, the TR was 3.4ms and flip angle of 5^0, number of projections was 128,000 and the FOV was chosen to cover the knee and acquired using a knee RF coil. Four data sets had matrix sizes of 256 x 256 x 256 while one of them had dimensions of 379 x379 x 379. The acquired k-space was gridded to Cartesian k-space as in (9) (code supplied by collaborators at Minnesota) and Fourier transformed with density compensation to obtain the full k-space reconstruction. The gridding parameters consisted of an oversampling factor of 2 to avoid aliasing and an apodization kernel of length 2 to reduce ringing artifacts.

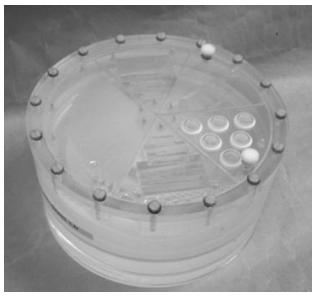

Figure 5.3 Photograph of the resolution phantom used in the project

The compressed sensing reconstruction was performed for acceleration factors of 2, 3, 4 and 5X. The undersampled k-space was gridded as in the prior case and Fourier transformed with density compensation (zfwdc) and normalized. This served as the initial estimate of the volume which was iteratively reconstructed using a custom implementation of a nonlinear conjugate gradient algorithm to solve [5.1] using a value of 0.005 for λ_{TV}. This value was fixed for all reconstructions including the phantom and the knee data sets. This was done to ensure consistency in comparative analyses. Error quantification was performed by computing the RMSE (eq. 3.1) weighted by the number of voxels in each data set, for each acceleration factor of the resolution phantom and the pooled in *vivo* data.

A simple semi-automatic segmentation procedure was implemented to visualize the ligaments: anterior cruciate ligament (ACL), posterior cruciate ligament (PCL) and adjacent structures. A ROI was drawn on each of the center sagittal slice of the original data sets to obtain the mean (μ) and standard (σ) deviation of the intensity of the region as shown in orange overlay in figure 5.4 for the representative data set (a). A threshold value greater than the standard deviation subtracted from the mean (μ - σ) was chosen to obtain voxels of interest depicted in figure 5.4 (b). This value of threshold was used for corresponding reconstructions at the chosen values of accelerations and the procedure repeated for all data sets. The number of segmented voxels in each case was tabulated andthe percentage difference in the number of voxels was calculated for each acceleration and data set with respect to the corresponding full

k-space reconstruction and the average and standard deviations of these percentages were computed over the 5 data sets.

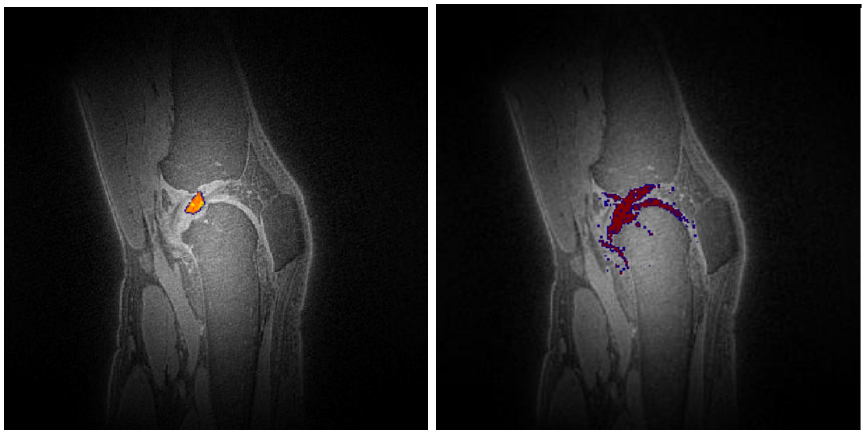

Figure 5.4 Segmentation procedure (a) ROI drawn on the center sagittal slice shown in orange overlay on the MRI (b) the resulting segmentation on the corresponding slice.

5.4 Results

5.4.1. Resolution phantom

The results of reconstruction for the phantom can be qualitatively assessed through figures 5.5- 5.8. Figure 5.5 depicts a line intensity profile through a symmetric feature to depict the reconstruction process. (All images are displayed in the range of [0 0.75]). It can be seen that the zfwdc profile contains relevant information but contains incoherent noise (typical of CS), which is subsequently removed by the iterative reconstruction. It can also be seen that this noise increases with undersampling. The denoising effect of the TV can be visualized by comparing the line intensity graphs of the zfwdc to those corresponding to the iteratively reconstructed graphs. Five slices from the center of the volume for each of the three orientations are shown in figures 5.6 – 5.8. These panels demonstrate the utility for choosing a 3D TV norm as it can be confirmed that the features do not change drastically over space for

the chosen MR resolution and FOV. It can be observed that the reconstructions retain fidelity for accelerations up to 5X. It can be seen from the figure 5.6that fine detail is also preserved. However, a subtle loss of sharpness in the image can be observed when comparing 5X to 1X. It can also be noticed that the background noise increases with acceleration as can be seen in figure 5.5 and a progressive smoothening with increased accelerations to compensate for the increased noise.

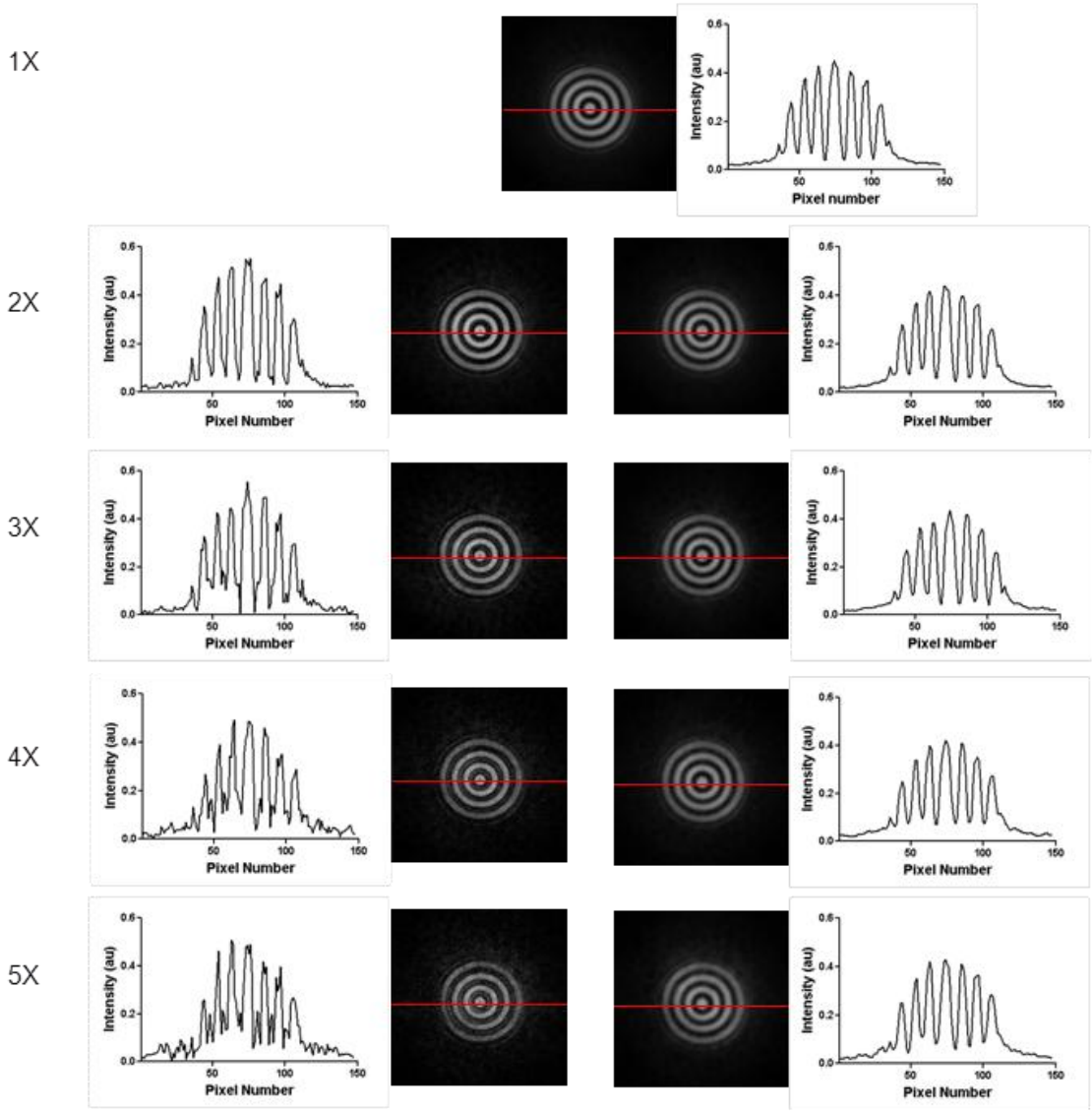

Figure 5.5 Line intensity profile of a symmetrical feature in the resolution phantom shown in the top panel (a) the images reconstructed after zero-filling with density compensation for the accelerations shown and (b) the corresponding reconstructions and the plot of line intensities adjacent to the images

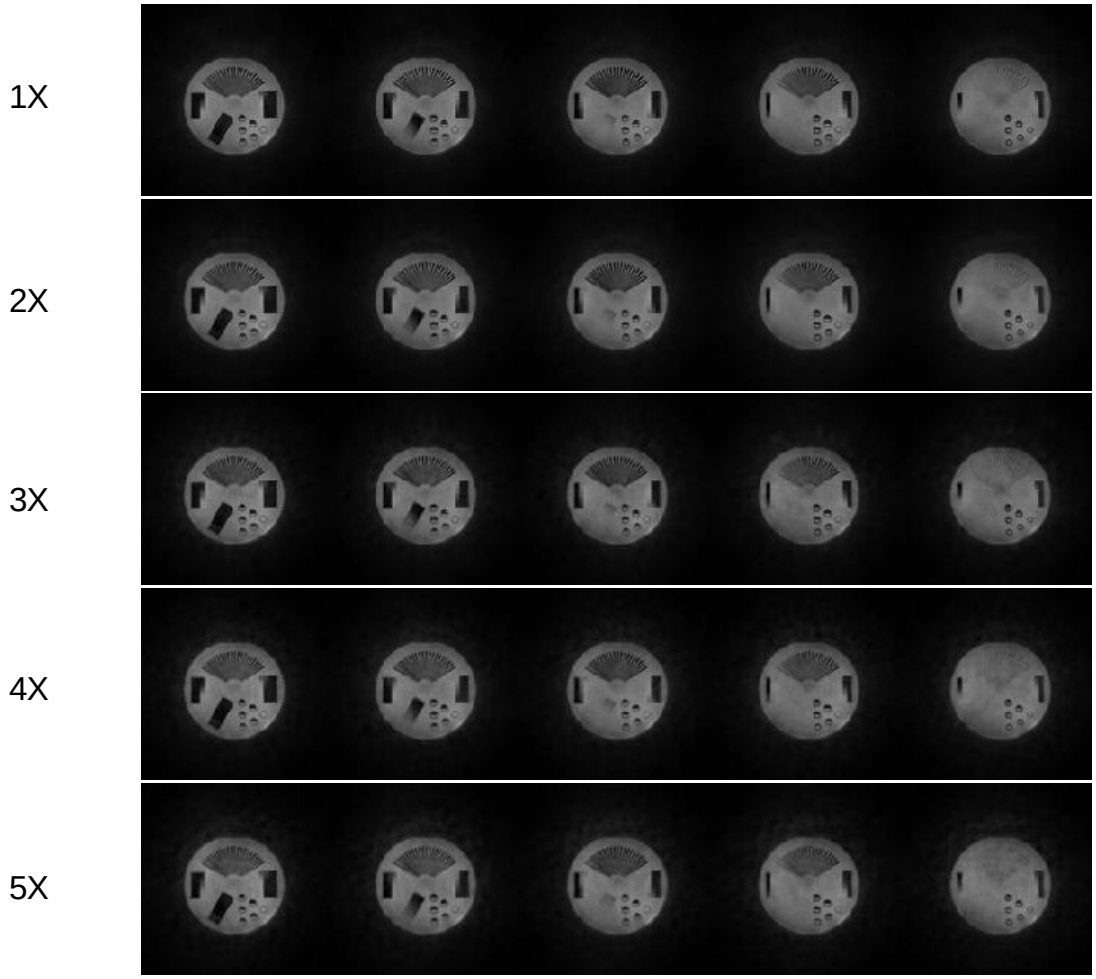

Figure 5.6 Slices through the center of the resolution phantom as seen in the coronal orientation

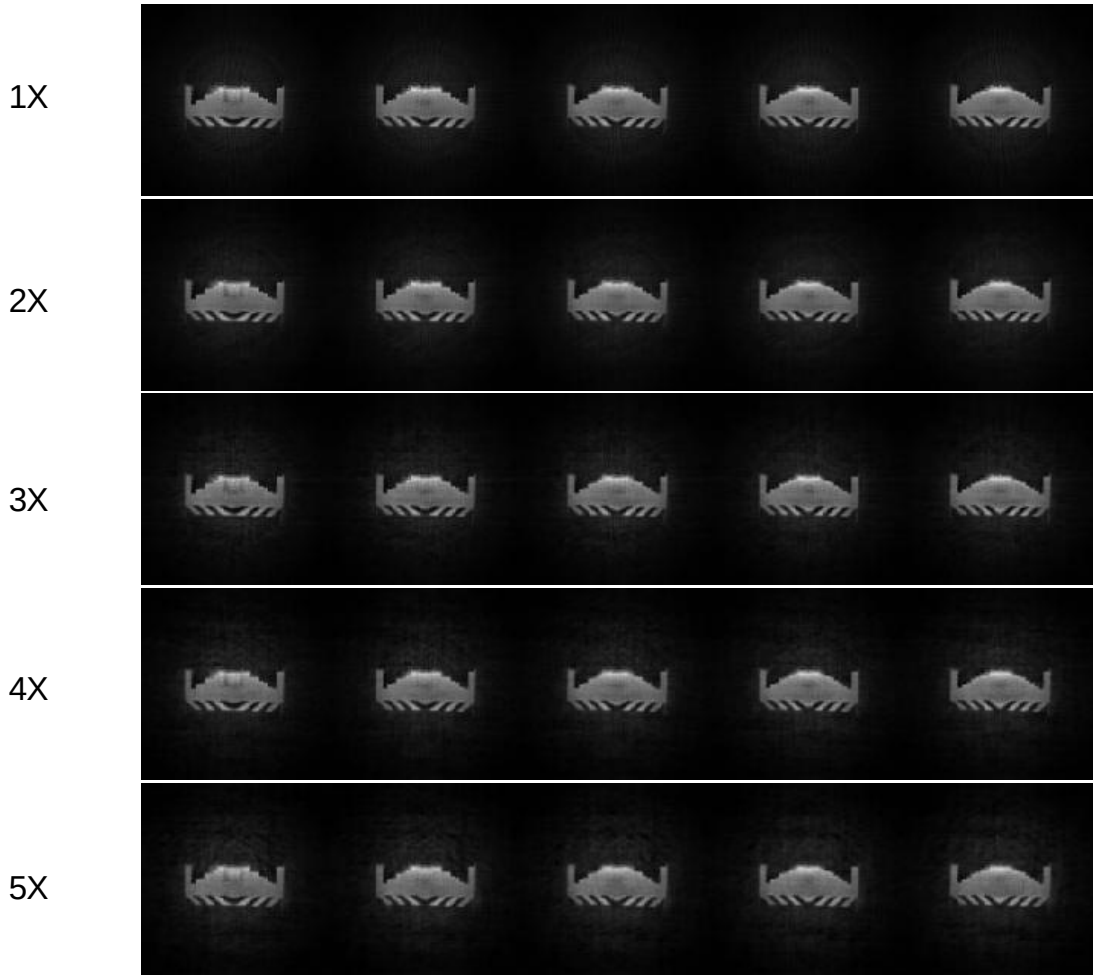

Figure 5.7 Slices through the center of the resolution phantom as seen in theaxial orientation

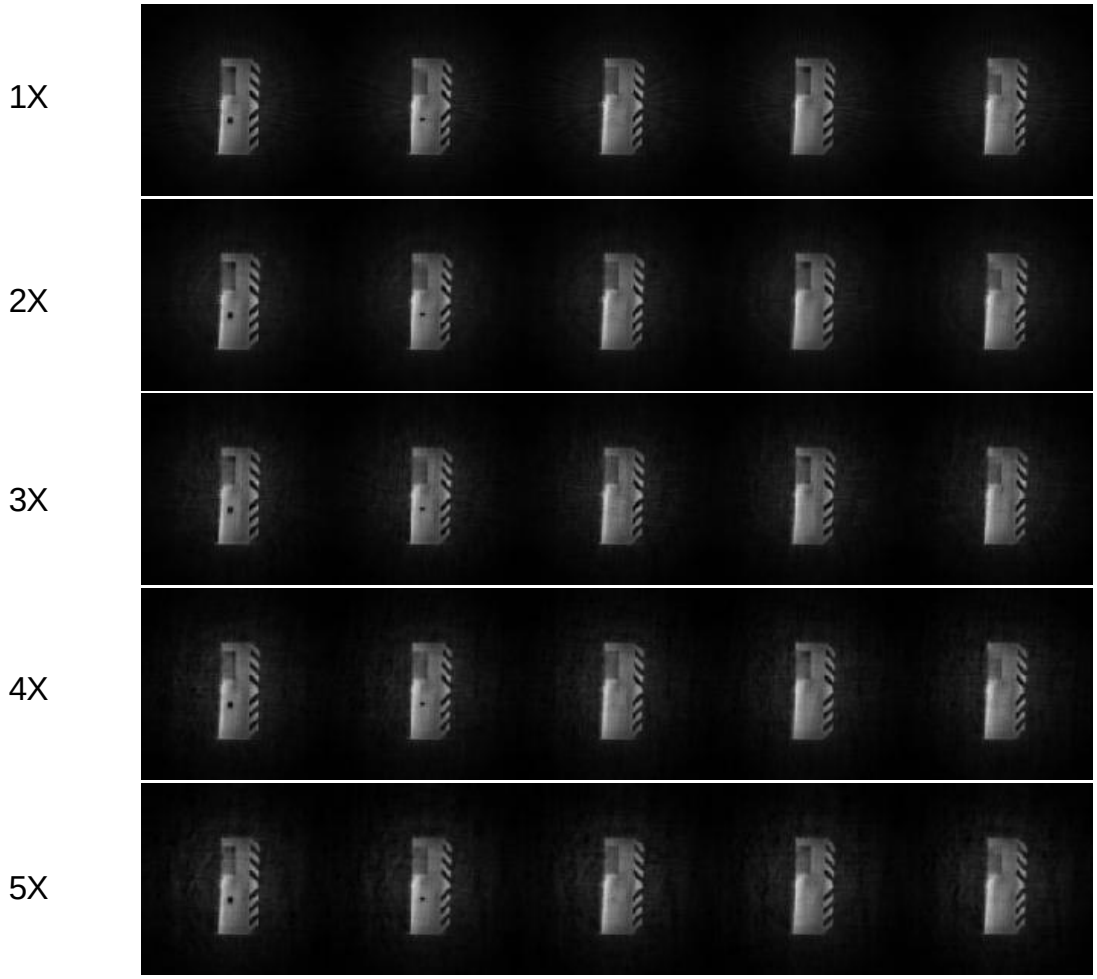

Figure 5.8 Slices through the center of the resolution phantom as seen in the sagittal orientation

5.4.2. In vivo knee data

The CS CODE MRI of a representative human knee is shown in figure 5.9. The image panels show the effect of iterative reconstruction for the compressed sensed CODE data. The original reconstruction using the full k-space data can be seen at the top of the panel. A line intensity profile from the image shown by the red line on the image is shown in the graph adjacent to it. The first column of images below shows the zfwdc images for acceleration factors of 2, 3, 4 and 5 while the second column depicts the corresponding iterative reconstructions.

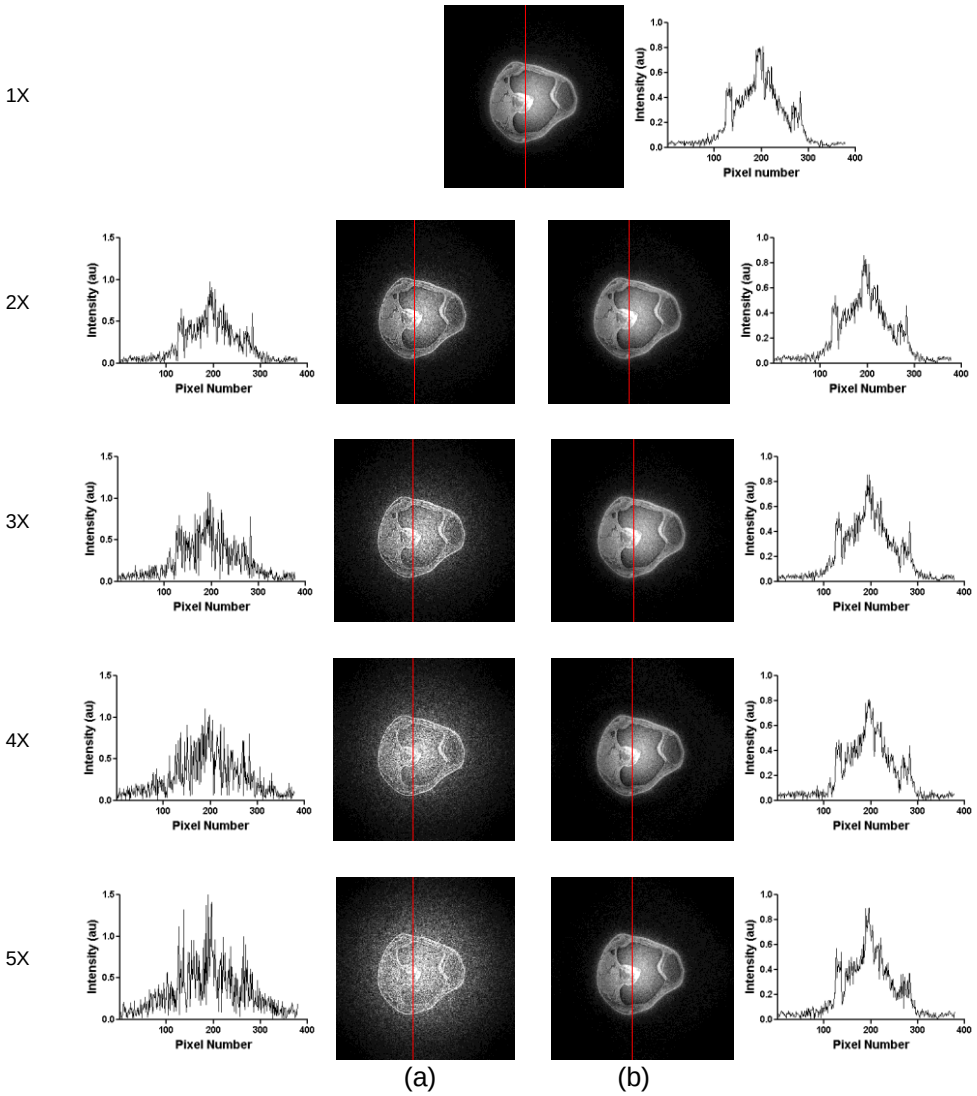

Figure 5.9 Line intensity profile of a symmetrical feature in the representative human knee shown in the top panel (a) the images reconstructed after zero-filling with density compensation for the accelerations shown and (b) the corresponding reconstructions and the plot of line intensities adjacent to the images

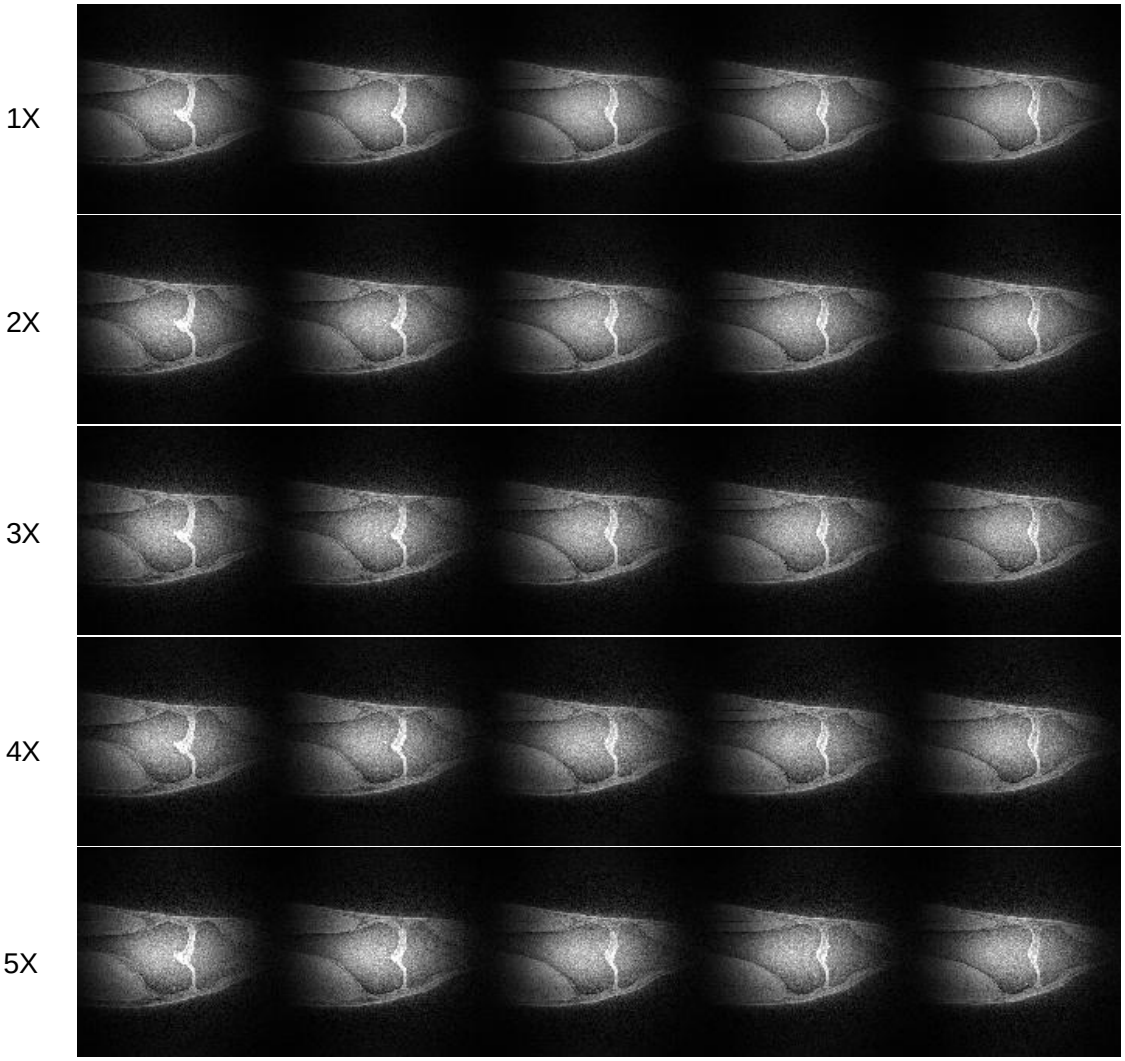

Figure 5.10 Slices through the center of a representative human knee (with each slice separated from the other by 3 slices) as seen in the coronal orientation.

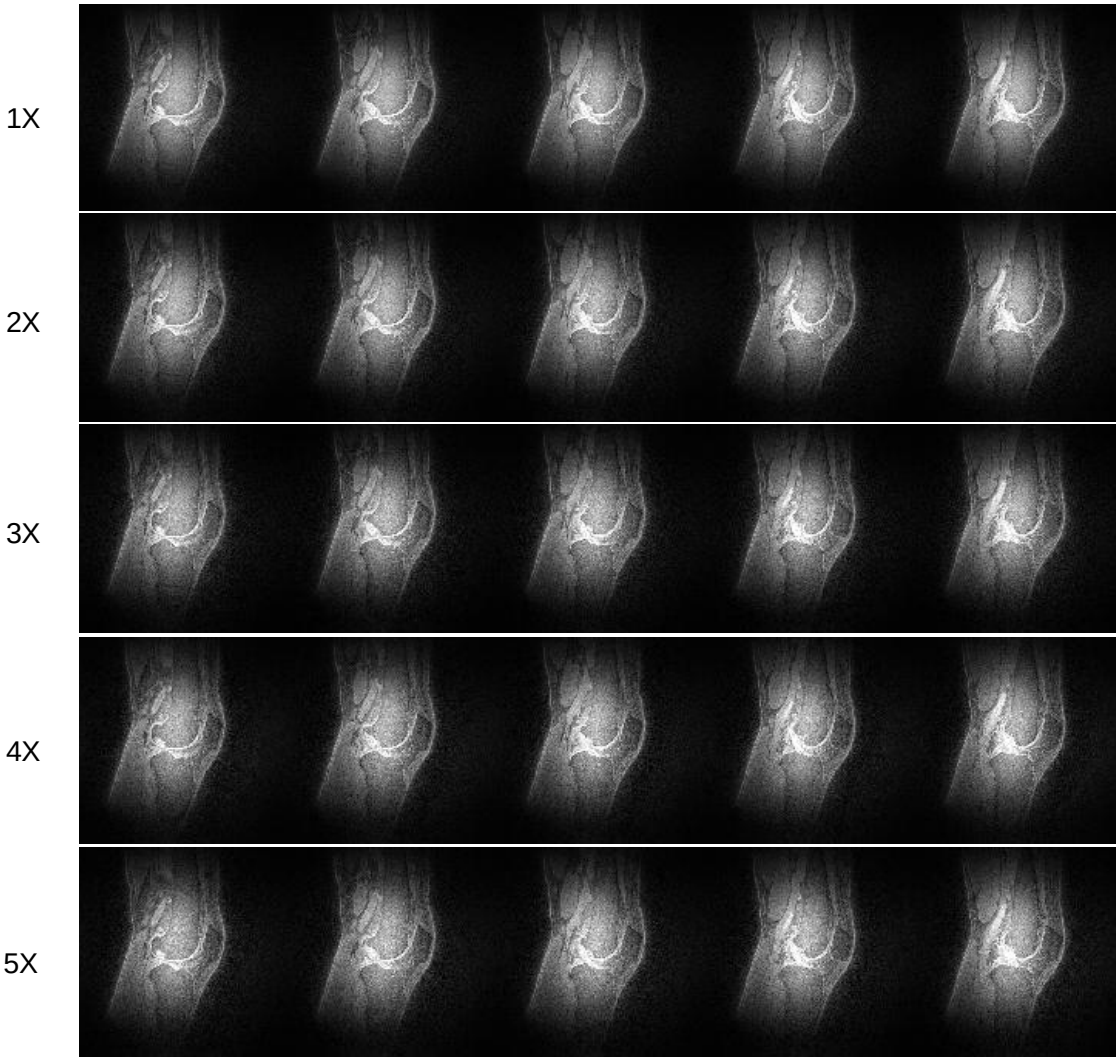

Figure 5.11 Slices through the center of a representative human knee (with each slice separated from the other by 3 slices) as seen in sagittal orientation.

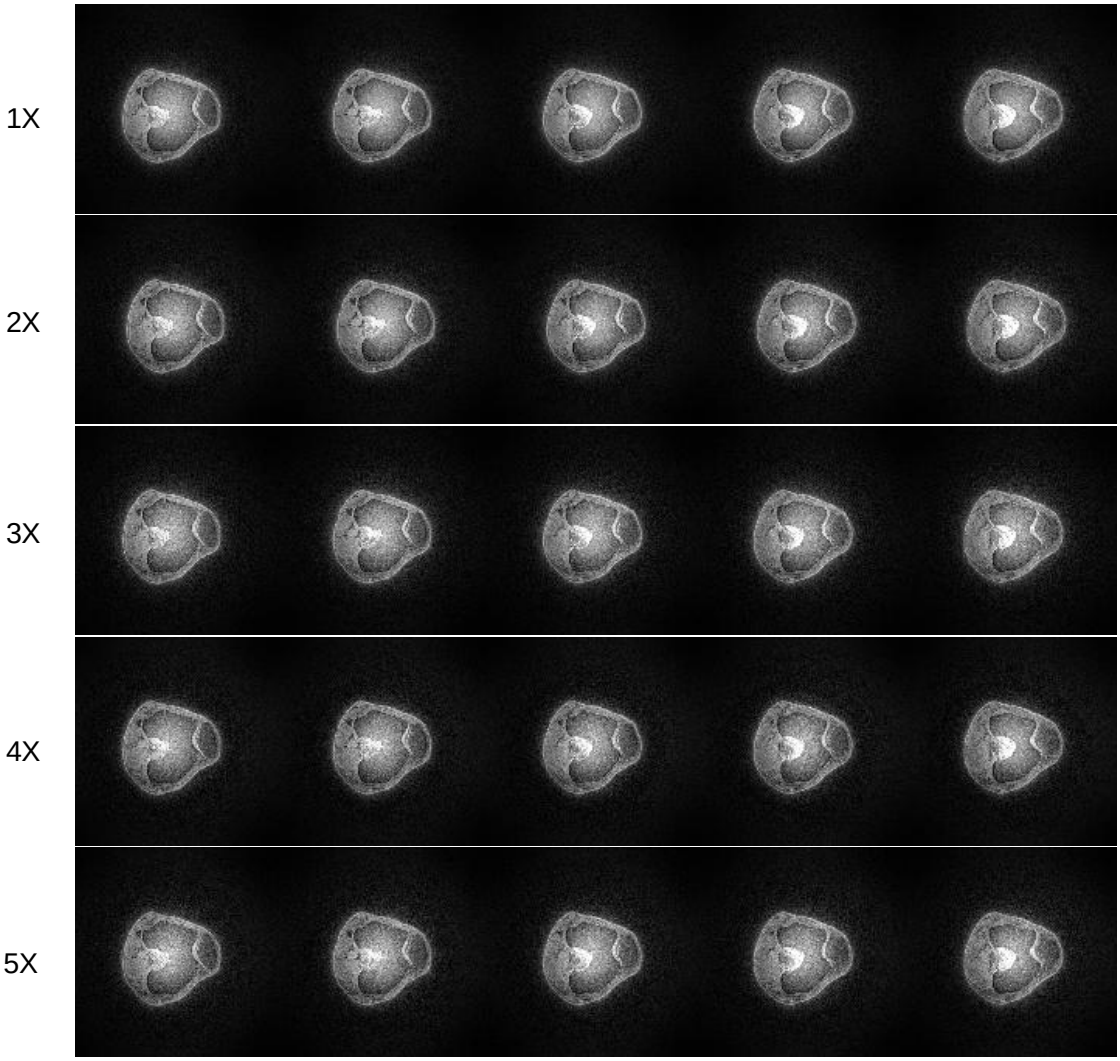

Figure 5.12 Slices through the center of a representative human knee (with each slice separated from the other by 3 slices) as seen theaxial orientation.

It can be observed that the reconstructions successfully recover the information corresponding to the original case. It can also be noticed that the zfwdc images become progressively noisier with accelerations but the reconstructions compensate for the noise and recover the underlying image. The zfwdc images depict incoherent noise characteristic of compressed sensing (note the change of scale for the zfwdc line intensities). The image panels

in figures 5.10 – 5.12 show five slices from the center (with each slice separated by two slices) as seen in the three different orientations. These image panels depict the fidelity of the reconstructions across slices and orientations.

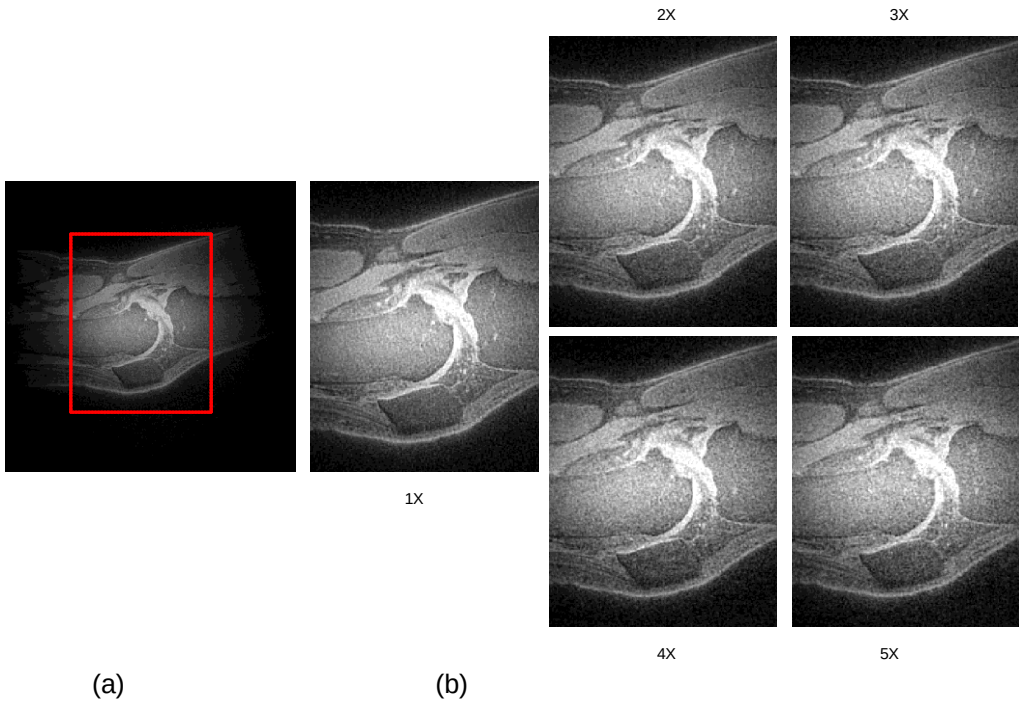

Figure 5.13 (a) Sagittal view of the center slice of the representative data set showing the ligaments (b) Magnified images at 1, 2, 3, 4, and 5X for the area showed by the red box in (a)

It also justifies the use of the 3D TV norm to denoise the minimum energy reconstruction, which has high frequency noise, opposed by the nature of TV. The 5X reconstruction has increased noise background as in the case of the phantom reconstruction. Figure 5.13 shows magnified images of the central slice in the sagittal plane to evaluate reconstruction of important structures important in musculoskeletal studies. It can also be noticed that these fine details in the image related to the ligaments such as the anterior cruciate ligament (ACL) and the posterior cruciate ligament (PCL) have been faithfully reproduced even at 5X. Also, the effect of gridding that can be seen in the 1X image as oblique lines from top-left

of the image to bottom-right are present in all the reconstructions due to the usage of gridding in the process. Therefore, the reconstruction preserves the information regarding knee structures important for diagnosis of musculoskeletal pathologies, such as the ACL and PCL, important for injuries related to ligament tear, has been preserved.

5.4.3. Error quantification

Figure 5.14 shows the results of quantification of error using RMSE. The value for RMSE increase with acceleration as is expected and is lesser for the phantom as compared to the *in vivo* data sets.However, the values of RMSE do not exceed 0.02 even at 5X. These values reflect the fidelity of reconstructions shown in figures 5.5 – 5.13.

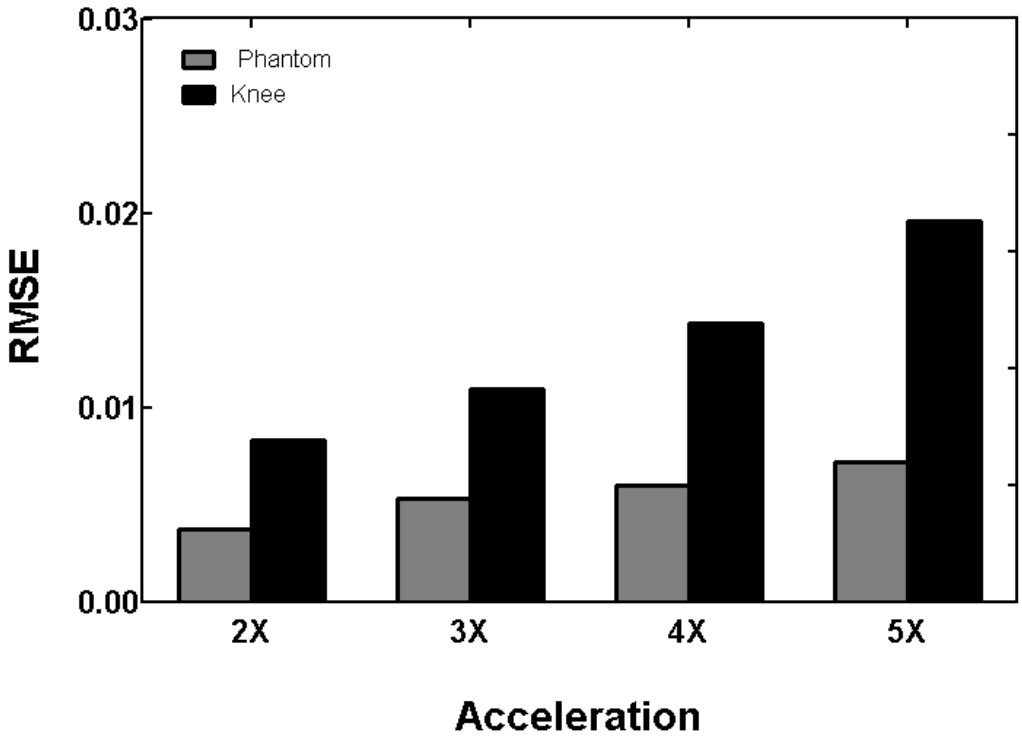

Figure 5.14 RMSE values for the reconstructions of phantom and knee data sets over acceleration factors of 2, 3, 4 and 5X as compared to 1X

5.4.3. Volume segmentation

The results of the segmentation procedure are shown in figure 5.15 (a & b). It can be seen in figure 5.15(a) that the number of voxels resulting from reconstructions is similar to the 1X case but difference increase with acceleration. Particularly in case of Data4, the 5X has a significant increase in the number of segmented voxels. Similarly, it can be seen that 4X and 5X show increased error for Data5. These observations are reflected in figure 5.15 (b) where the percentage errors increase with increase in acceleration as is expected. The 5X case shows an error of ~17% and can be considered as the limit of the implementation.

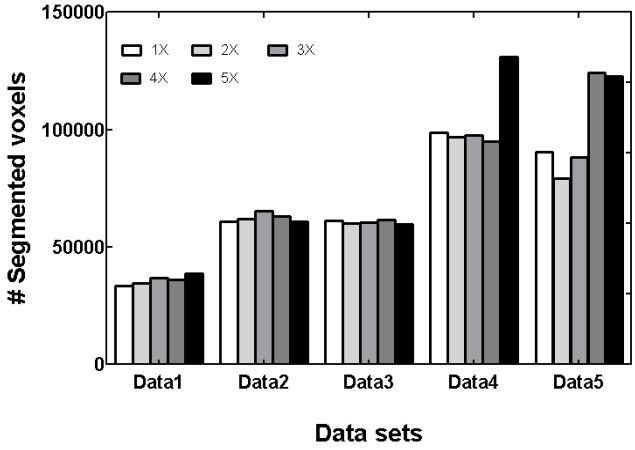

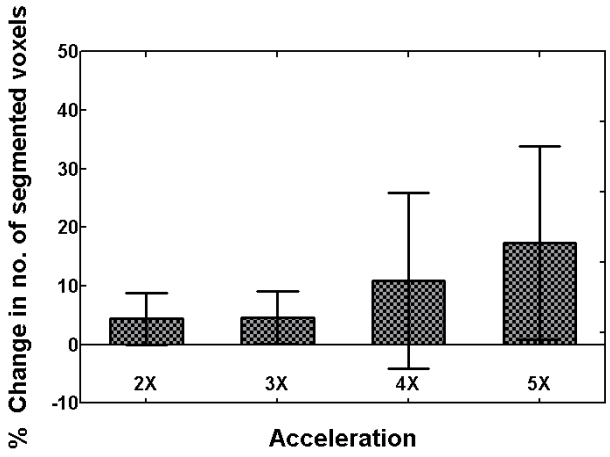

Figure 5.15 Segmentation results (a) Number of segmented voxels for each data set in comparison with the corresponding accelerated reconstructions (b) The pooled resulting difference in percentages for all the 5 data sets for the 4 acceleration factors with respect to the original data.

5.5 Conclusions

In this project, the demonstration of CS for accelerating SWIFT based MRI has been performed. It has been shown that it can be reliably accelerated up to 5X. The phantom data and the *in vivo* data sets show high fidelity reconstruction as indicated by the image panels and RMSE values. The segmentation procedure indicates an estimate of the percentage of error and can be observed that it increases in data4 and 5 reflected in the increased error percentages at 5X. 3D TV has been employed as the sparsifying transform and has been shown to operate efficiently. The implementation could benefit from the use of 3D wavelets to enable further acceleration. This must be however weighed against computational complexity considering that these data sets are three-dimensional and have matrix sizes of 256 in each of the three dimensions. The speed of reconstructions could be increased using graphical processing units and/or through increased usage of sparse matrices in MATLAB. Iterative reconstruction in particular needs to be accelerated due to the dependence of the current estimate on its previous value. Implementation of the CS based pulse sequence is straightforward due to the radial nature of the acquisition. This k-space trajectory is also an ideal match for CS as detailed in 5.2.1. The prospective pulse sequence could be highly useful in a variety of biological applications such as cine-MRI applications of the musculoskeletal system (88) and imaging of connective tissues such as menisci, tendons, ligaments that contain bound water with ultra-short T_2 values. However, radiological evaluation of these images is necessary to evaluate clinical utility and significance. In addition to knee imaging, SWIFT has also been demonstrated on breast DCE-MRI (89) and neuroimaging (90). Acceleration is a key requirement in some of these studies and can be used to obtain increased information content. CS SWIFT MRI can also be used to image dynamics of fast T_2 exchange contrast agents to visualize contrast that needs high speeds of acquisition. Therefore, the advantages of CS SWIFT MRI can be utilized to image higher dimensional information and/or obtain accelerated images to visualize dynamics of biological systems with short T_2 related features.

CHAPTER 6

CONCLUSION AND RECOMMENDATIONS

Acceleration of MRI acquisitions is a key area of development in MR technology to facilitate attainment of increased information content. This is a fundamental improvement for a medical imaging system. Compressed sensing has been shown to achieve this goal without significant loss of SNR. In this work, compressed sensing has been demonstrated on three novel applications. Each of these applications would be able to obtain enhanced information content through compressed sensing: reduced acquisition time can be used to obtain better spatial and/or temporal resolutions, increased SNR through increased averaging and most importantly acquire MR data within acceptable acquisition times for the subject. The increased throughput reduced Specific Absorption Rate (SAR) and reduced MR technician time all result in significant gains from a clinical perspective. Reduction in SAR alone can enable further acceleration of acquisitions. Therefore, the applications demonstrated have significantly high clinical relevance.

6.1 CS MRSI

Compressed sensing accelerated ^{1}H MRSI has been demonstrated on the 2D case in chapter 3. The evaluation of this application has shown that MRSI can be reliably accelerated for undersampling of 5X through reproducibility of clinically relevant biomarkers as indicated by non-significant statistical differences between the original and 5X reconstructions and the

increased statistical differences at 10X. Hence the null hypothesis of no significant differences is confirmed up to 5X and this ratifies the hypothesis that CS can be employed to accelerate conventional MRSI acquisitions. These findings would allow and enable prospective implementations of pulse sequences based on CS MRSI and also point to parameters such as the choice of required acceleration and the sampling maskand most importantly, indicate the limitations of a prospective implementation based on this method of implementation. This is particularly relevant for MR researchers using MRSI as the tool to investigate novel biomarkers of pathologies. Most of these metabolites are smaller, such as glutamate and glycine, in amplitudeto other metabolites such as NAA and require increased averaging and specialized pulse sequences to image them. This application now serves as a motivation for such research to employ compressed sensing to achieve increased averaging. However, the most significant impact would be on routine MRSI exams. Since the prospective implementation of the proposed phase encoding scheme is straight forward, implementation of the pulse sequence would not be too involved. MRSI has been a specialized MR technique in the set of MR methods in the sense that it requires increased acquisition skills in voxel placement, shimming and lipid suppression. This application allows the technician in the clinical setting to focus more on the above processes. The major hurdle for the use of MRSI in a clinical setting as opposed to a clinical research setting is the lengthy acquisition time and required technician skills. Through this application, it has been shownthat a potential to overcome this hurdle can be achieved.

It has also been shown that the performance of compressed sensing improves with increased dimensionality similar to the results of compression algorithms. Extension of the current application to true 3D MRSI would allow for enhanced sparsity resulting in increased accelerations. This would also allow for non-Cartesian k-space trajectories to be implemented in the multiple phase encode directions. The advantage of this approach would be a better control on SNR, faster acquisitions and tailored k-space sampling leading to more incoherent artifacts.

This would result in increased reconstruction complexity due to the required gridding, regridding and sampling density operations but would be justified by the gains mentioned above.

6.2 CS DCE-MRI

The retrospective speeding-up of DCE-MRI through the application of compressed sensing has been demonstrated in chapter 4. DCE-MRI is a particularly well suited problem for compressed sensing due to the simultaneous requirement of spatial and temporal resolutions. To this end, it has been demonstrated that CS based methods can provide good fidelity with 20% of k-space data or more. It has also been shown that this undersampling does not significantly alter the pharmacokinetic maps as shown by the results of the statistical tests confirming the null hypothesis that there are no statistically significantly differences between the full k-space reconstruction and the accelerated reconstructions. Another important question addressed by the study is the choice of the undersampling mask for CS as applied to DCE-MRI. The undersampling mask needs to be an optimized solution between ease of implementation and desired pseudo-random sampling. The experimental set-up for a DCE-MRI scan is typically dictated by the physical characteristics of the chemical compound used as the contrast agent such as its molecular weight and the choice of the pharmacokinetic model used to obtain the pharmacokinetic maps. These experimental parameters reflect the necessity for the spatial and/or temporal resolutions.Keeping this in view, the goal of CS for these applications should be to enhance information content rather than achieve increased acceleration only. For instance, a temporal resolution of 23 seconds, a spatial resolution of 0.3mm/pixel (2D case) and the reference region kinetic model have been shown to be satisfactory(91). A useful CS application would be to obtain a 3D MRI of the tumor, resulting in increased information content rather than to obtain increased time resolution for this experimental protocol. This is particularly important

and required due to the heterogeneity that is often present in tumors and 3D morphology aids in obtaining comprehensive information regarding the tumor and also due to the fact that multi-slice imaging is restricted due to the required temporal resolution.

The results of the study also point to the efficiency of the sampling masks based on thresholded k-space of the particular tumor volume being examined as these masks include *apriori* information regarding the object being imaged. However, implementation of these masks is not straightforward. An optimal gradient design based on varying spiral density such that most points of the mask are sampled, is one of the options but is computationally intensive on the reconstruction side. Moreover, the artifacts resulting from spiral imaging are not easily recognizable as they are spread across the image. However, these results point towards the requirement and efficacy of alternate k-space trajectories from a CS perspective. The most elegant solution would be, to be able to design the 'optimal' k-space trajectory for CS based on the application, maximum incoherence, required acceleration, demands on gradient performance and including *apriori* information about the object being imaged. These call for an optimization routine that can be implemented real-time and can be translated into a pulse sequence for acquisition. MR image reconstruction for such trajectories devoid of identifiable artifacts is a challenging opportunity. As MRI moves towards personalized acquisition through technologies like multi-dimensional RF pulses and parallel-transmit, understanding of complex k-space trajectories would be of great importance. This could significantly enhance the role of CS for multidimensional applications such as DCE-MRI.

6.3 CS SWIFT

SWIFT MRI is a novel technique that involves the combination of NMR methods to obtain information on short- T_2^* components. This has been used in different applications of the knee, brain and breast to demonstrate its utility. In chapter 5, the application of CS on SWIFT MRI has

been detailed. It has been shown that SWIFT MRI data of a resolution phantom and human knee can be reliably accelerated up to 5X within tolerable values of error as shown by the RMSE and the results of the segmentation procedures. CS SWIFT MRI is a classic example of the exploitation of the k-space trajectory of SWIFT by CS. In other words, the problem lends itself very well to the requirements of CS explained in Chapter 2. The reconstruction of CS SWIFT MRI needs to be improved to facilitate online reconstruction on the scanner. The implemented reconstruction runs on a Windows platform, Xeon processor and uses MATLAB as the programming tool. This needs to be translated to the scanner hardware and software to examine and improve the implementation of the prototype implemented in the lab. The reconstruction engines sold with the scanner can aid in this process. Hence, the next step for prospective implementation would involve evaluating the reconstruction in the scanner environment. It is expected that such retrospective applications will provide a basis for prospective implementation to further acquisition of cine-MRI data of the knee. Evaluation of these images by a radiologist is critical for this implementation to facilitate prospective studies. Hence, this is the most significant evaluation step required for this project. This demonstration of CS SWIFT on knee can also be readily extended to other anatomies where SWIFT could be useful and acceleration is required, as the pulse sequence is expected to be the same. Therefore, the results of Chapter 5 can be used to evaluate future possible roles for CS SWIFT MRI in different applications such as breast DCE-MRI and dynamic imaging of T_2 exchange agents.

APPENDIX A

TOP LEVEL MATLAB SCRIPTS FOR THE THREE PROJECTS

A.1 CS MRSI

Main file for demonstration of compressed sensing based reconstruction of undersampled MRSI data

Contents

- Choose periodization mode for wavelet decomposition
- Variable Initialization
- Read input data.
- Undersample k-space
- Zero filled with density compensation
- Reconstruction parameters.
- Wavelet coeffs.
- Iterative reconstruction
- Write truth file.
- Check grid matching - added this part for visualization - Spectrum of interest is in the first 400 points.
- Check voxel matching - Spectrum of interest is in the first 400 points.
- Write reconstructed file.

Choose periodization mode for wavelet decomposition

```
closeall; dwtmode('per'); addpath(genpath('.'));clc;
```

Variable Initialization

```
write_spectra =0; usamp = 0.5;%usamp factors of 0.5,0.33,0.25,0.2,0.1
D = [16 16 1024];% Size of the data set
P =5];%Polynomial for the variable density sampling
```

Read input data.

```
[time_dom_signal,spectra,str_data2] = read_brain_data(D);
spectra = spectra/max(abs(spectra(:)));];% Normalize
kspace = reconstruct_kspace(spectra,ones(size(spectra)));
```

Undersample k-space

```
pdf = genPDF([D(1) D(2)],P,usamp,2,usamp,0);
 [mask,~,actpctg] = genSampling(pdf,30,3);%actpctg is the actual usamp achieved
disp(['Actual undersampling is ',num2str(sum(mask(:))/numel(mask))]);% another
verificationfigure;imagesc(mask); mask = mask./pdf;   %Density
compensationsampling_mask=repmat(mask,[1 1 D(3)]); %repeat through time.
kspace_us = kspace.*sampling_mask;
```

Zero filled with density compensation

```
csi_zfwdc = reconstruct_spectra(kspace_us);  % This helps in using one value for beta for all cases.kspace =  kspace/max(abs(csi_zfwdc(:))); kspace_us = kspace_us/max(abs(csi_zfwdc(:))); csi_zfwdc = csi_zfwdc/max(abs(csi_zfwdc(:)));
```

Reconstruction parameters.

```
maxIter= 8; % Number of ncg iterations (internal to the recon iter) was 8.
xfmWeight =0.001; TVWeight =0.005; level = 4; wname = 'db4'; ];% Wavelet params
```

Wavelet coeffs.

```
      [W,B] =get_wcoff(csi_zfwdc);
```

Iterative reconstruction

```
for k=1:8 % Number of recon iterations was 8.
m1 = ncg(W,B,sampling_mask,kspace_us,maxIter,TVWeight,xfmWeight,level,wname);
[W,B] =get_wcoff(m1);
%      imagesc(sum(abs(m1),3));colorbar;drawnow;
end
RMSE = get_RMSE(spectra, m1); disp(RMSE);
display_spectra_mosaic(spectra);
```

Write original file.

```
if(write_spectra ==1)     [filename,pathname]=uiputfile(\*.txt','Save as true jmrui file');
fileaddress = fullfile(pathname,filename);     save_jMRUI_fmts(spectra,str_data2,fileaddress);
end
```

Check grid matching - added this part for visualization - Spectrum of interest is in the first 400 points.

```
display_spectra_mosaic(cat(3,spectra(:,:,1:400),zeros(16,16,100), m1(:,:,1:400)));
```

Check voxel matching - Spectrum of interest is in the first 400 points.

```
figure; subplot(211); plot(squeeze(abs(spectra(8,8,1:400))));hold on;
plot(squeeze(abs(m1(8,8,1:400))),'r');   subplot(212);
plot(squeeze(abs(spectra(1,1,1:400))));hold on; plot(squeeze(abs(m1(1,1,1:400))),'r'); drawnow;
```

Write reconstructed file.

```
[filename,pathname]=uiputfile('\*.txt','Save as jmrui file');
if(filename ~= 0) fileaddress = fullfile(pathname,filename);
save_jMRUI_fmts(m1,str_data2,fileaddress);
end
```

Published with MATLAB® 7.13

A.2 CS DCE-MRI

A.2.1 Key-hole methods

This file describes the project –Mainfile for keyhole methods.

Contents

- Paths to be added.
- Full k-space reconstruction.- A1 Center the k-space and Image space.
- Keyhole reconstruction phase encode lines - A2
- Keyhole reconstruction BOX - A3
- Keyhole reconstruction THRESH - A4
- Obtain RMSE
- Make an AVI file.

Paths to be added and load data files.

```
clearall; addpath(genpath('.'));
[fname,dirname] = uigetfile(); load(fullfile(dirname,fname));
sampling_density=0.2;
% %% Priors
apram.x2 =x2; ];% Shift to get the image in the center
apram.x =x; % Shift to get the data in the center
apram.y =y; % Shift to get the data in the center
apram.BW =BW; % Mask to apply for the image in the end
if(exist('kspace','var')==0) [kspace,pre_num,post_num] = get_data_dce(1); end];% Read input
data
if(exist('pre_num','var')==0)     pre_num=4;     post_num=60; end];% Define pre and post
contrast frames
display_enable=0;D = size(kspace);
kspace_cshift = zeros(D);
recon_full_data = kspace_cshift;  %display_dce_data(kspace_cshift);
```

Full k-space reconstruction.- A1 Center the k-space and Image space.

```
for k =1:size(kspace,3)
k2 = (squeeze(kspace(:,:,k)));
kspace_cshift(:,:,k) = circshift(k2,[y x]);
recon_full_data(:,:,k) = BW.*circshift(ifft2c(squeeze(kspace_cshift(:,:,k))),[0 -x2]);
%
imshow(abs(squeeze(recon_full_data(:,:,k))),[],'InitialMagnification',600);colormap(gray);pause;e
nd
kspace_cshift = kspace_cshift./max(abs(recon_full_data(:)));
recon_full_data = recon_full_data./max(abs(recon_full_data(:)));
S = get_intensity_ROI(abs(recon_full_data),BW); plot(S);
```

Keyhole reconstruction phase encode lines - A2

```
addpath'\DCE\CS_MRI\A2\';
disp('keylines');
[sampling_mask_keylines,samp_act_conv]=A2_gen_sampling_mask_keylines(D,pre_num,post
_num,sampling_density); % Keylines mask
kspace_keylines = sampling_mask_keylines.*kspace_cshift;
recon_keylines_data =
recon_key(kspace_keylines,pre_num,post_num,sampling_mask_keylines,apram);
%
display_dce_data(kspace_keyhole);recon_keylines_data(:,:,1:pre_num)=recon_full_data(:,:,1:pr
e_num);
recon_key_data = recon_keylines_data;
```

Keyhole reconstruction BOX - A3

```
disp('Keyhole'); [sampling_mask_keybox,samp_act_keybox] =
A2_gen_sampling_mask_keybox(D,pre_num,post_num,sampling_density); % Keyhole
maskkspace_keyhole_box = sampling_mask_keybox.*kspace_cshift;
recon_key_data_box =
recon_key(kspace_keyhole_box,pre_num,post_num,sampling_mask_keybox,apram);
%
display_dce_data(kspace_keyhole_box);recon_key_data_box(:,:,1:pre_num)=recon_full_data(:,
:,1:pre_num);
```

Keyhole reconstruction THRESH - A4

```
disp('Keythresh'); kspace_pre_mean = mean(kspace_cshift(:,:,1:pre_num),3);
[sampling_mask_thresh,samp_act_keythresh] =
A2_gen_sampling_mask_keythresh(D,pre_num,post_num,sampling_density,kspace_pre_mean
); % Keythresh mask
kspace_keyhole_thresh = sampling_mask_thresh.*kspace_cshift; recon_key_data_thresh =
recon_key(kspace_keyhole_thresh,pre_num,post_num,sampling_mask_thresh,apram);
%
display_dce_data(recon_key_data_thresh);recon_key_data_thresh(:,:,1:pre_num)=recon_full_d
ata(:,:,1:pre_num);
```

Obtain RMSE

```
RMSE_keyhole=get_RMSE(recon_full_data,recon_key_data);
RMSE_keybox=get_RMSE(recon_full_data,recon_key_data_box);
RMSE_keythresh=get_RMSE(recon_full_data,recon_key_data_thresh);
uisave({'recon_full_data','recon_key_data','recon_key_data_box','recon_key_data_thresh'});
```

Make an AVI file.

```
makeavifile_keyhole(recon_full_data,recon_key_data,recon_key_data_box,recon_key_data_thr
esh);
```

Published with MATLAB® 7.13

A.2.2 CS methods

Contents

- Generate one pdf so that all the original recons will be the same.
- Read priors about the data set
- Input data for recon
- Case wise recon
- AVI file showing %undersampling and recons


```
% Main file for CS based methods.
```

Generate one pdf so that all the original recons will be the same.

```
clearall; addpath(genpath('.'));
[fname,dirname] = uigetfile(); load(fullfile(dirname,fname));
```

Read priors about the data set

```
apram.x2 =x2;
apram.x =x;
apram.y =y;
apram.BW =BW;
apram.kspace = kspace;
if(exist('pre_num','var')==0)
apram.pre_num = 4;
apram.post_num=60;
else
apram.pre_num =pre_num;
apram.post_num = post_num;
end
```

Input data for recon

```
sampling_density=0.2;
P =3;%Polynomial determining the variable sampling density
D = [64 64];
pdf = genPDF([D(1) D(2)],P,sampling_density, 2 ,0.1,0);
```

Case wise recon

```
[recon_full_data,gauss_recon,rmse_gr] = cs_methods('Gaussian',pdf,sampling_density,apram);
[~,glines_recon,rmse_gl] = cs_methods('Gauss_lines',pdf,sampling_density,apram);
[~,gthresh_recon,rmse_gt] = cs_methods('Threshold',pdf,sampling_density,apram);
```

AVI file showing %undersampling and recons

```
makeavifile_all((100*sampling_density),abs(recon_full_data),abs(gauss_recon),abs(glines_recon),abs(gthresh_recon));
uisave({'recon_full_data','gauss_recon','glines_recon','gthresh_recon'}, \Processed_data\var1')
```

Published with MATLAB® 7.13

```
function [recon_full_data,mfinal,RMSE] = cs_methods(mask,pdf,sampling_density,apram)
```

Contents

- Priors
- Read input data.
- Variable declaration
- PDF and sampling mask with density compensation
- Get im_zfwdc and normalize - % This helps in using one value for beta for all values.
- Reconstruction parameters.
- Wavelet coeffs.
- Iterative reconstruction
- Apply ROI.

Priors

```
x2 =apram.x2;
x =apram.x;
y =apram.y;
BW =apram.BW;
kspace = apram.kspace;
pre_num = apram.pre_num;
post_num = apram.post_num;
```

Read input data.

```
If(exist('kspace','var')==0)
[kspace,pre_num,post_num] = get_data_dce(1);
end
```

Variable declaration

```
D = size(kspace);
kspace_cshift = zeros(D);
RES=kspace_cshift;
for k =1:size(kspace,3)
k2 = (squeeze(kspace(:,:,k)));
kspace_cshift(:,:,k) = circshift(k2,[y x]);
end
kspace_pre_mean = mean(kspace_cshift(:,:,1:pre_num),3);
P =3;
```

PDF and sampling mask with density compensation

```
sampling_mask = zeros(size(kspace_cshift));
switch(mask)
case'Gaussian'
for k=1:size(kspace_cshift,3)
sampling_mask(:,:,k) = genSampling(pdf,10,60);                    % generates a sampling pattern
based on CS-points
sampling_mask(:,:,k) = squeeze(sampling_mask(:,:,k))./pdf;
end

case'Threshold'
for k=1:size(kspace_cshift,3)
[sampling_mask(:,:,k),samp_act]= genSampling_thresh(pdf,10,60,kspace_pre_mean);          %
generates a sampling pattern based on CS-thresh
sampling_mask(:,:,k) = squeeze(sampling_mask(:,:,k))./pdf;
end

case'Gauss_lines'
for k=1:size(kspace_cshift,3)
[sampling_mask(:,:,k),actpctg] = genSampling_glines(pdf,10,60,sampling_density) ;
% generates a sampling pattern based on CS-lines

sampling_mask(:,:,k) = squeeze(sampling_mask(:,:,k))./pdf;
end
end
```

Get im_zfwdc and normalize - % This helps in using one value for beta for all values.

```
recon_full_data = reconstruct_images(kspace_cshift);
kp = repmat(kspace_pre_mean,[1 1 size(kspace_cshift,3)]);
mref = reconstruct_images(kp);
kspace_us = sampling_mask.*(kspace_cshift - kp);
im_zfwdc = reconstruct_images(kspace_us);   % Normalize data to 0 - 1
mref = mref/max(abs(recon_full_data(:)));
kspace_cshift =  kspace_cshift/max(abs(recon_full_data(:)));
kspace_us = kspace_us/max(abs(recon_full_data(:)));
im_zfwdc = im_zfwdc/max(abs(recon_full_data(:)));
recon_full_data = recon_full_data./max(abs(recon_full_data(:)));
```

Reconstruction parameters.

```
maxIter =10;
xfmWeight =0.005;
TVWeight =0.015;
level = 4;
wname = 'db4';
RMSE = zeros(length(xfmWeight),length(TVWeight));
% matlabpool open 6
for h=1:length(xfmWeight)
for s=1:length(TVWeight)
```

Wavelet coeffs.

```
        [W,B] =get_wcoff_dce(im_zfwdc,level,wname);
%         X= get_wavdecompimg(squeeze(W(1,:)),B,'db4');
%         imshow(abs(X));drawnow;% Display the wavelet decomposition
```

Iterative reconstruction

```
for k=1:8
m1 = ncg(W,B,sampling_mask,kspace_us,maxIter,TVWeight(s),xfmWeight(h),level,wname);
[W,B] =get_wcoff_dce(m1,level,wname);
endmfinal = m1 +mref;
```

Apply ROI.

```
recon_full_data = reconstruct_images(kspace_cshift);
for k=1:size(kspace,3)
mfinal(:,:,k) = BW.*circshift((squeeze(mfinal(:,:,k))),[0 -x2]);
recon_full_data(:,:,k) = BW.*circshift((squeeze(recon_full_data(:,:,k))),[0 -x2]);
end
RMSE(h,s) = get_RMSE(recon_full_data,mfinal);
end
end
```

Published with MATLAB® 7.13

‘

A.3 CS SWIFT MRI

Contents

- 1X case
- Radial kspace is the undersampled. No need of mask anymore, useproj_nums instead.
- Create RECONIN structure


```
clear all;

[Filename,Pathname]=uigetfile(\*.mat');
load(fullfile(Pathname,Filename)); clear PathnameFilename; % read input data
```

1X case

```
input_data = reshape(input_data,5,[],128000);
PARAM.matrix=256;
xorg = single(get_im_rad(input_data,PARAM)); % obtain image from projection data
figure;imagesc(abs(squeeze(xorg(:,:,round(size(xorg,3)/2)))),[0 1]);colormap(gray);
```

Radial kspace is the undersampled. No need of mask anymore, useproj_nums instead. Change accelerations to 2,3,4 and 5

```
PARAM=PARAM_CODE;%for d1% PARAM.matrix=256;%FOR D2, D3,D4 AND D5
acceleration =5; num_spheres = 100;%for d2-d5 128
num_projs =1000;
num_pts =388;
input_data = reshape(input_data,5,num_spheres,num_projs,num_pts);
[y,sel]=undersample_data(input_data,acceleration);%data,acc,num_spheres,num_projs% clear
input_data; [x0,y] = (get_im_rad(y,PARAM));
y2=y;pdf = single(pdfgen(0,y,(1/acceleration)));
x0 = get_im(y2./pdf); % zfwdc
figure;imagesc(abs(squeeze(x0(:,:,round(size(x0,3)/2)))),[0 1]);colormap(gray);
```

Create RECONIN structure

```
RECONIN.PARAM =PARAM; RECONIN.x0 =(x0); RECONIN.y =(y);
save('ZFDATA1','RECONIN'); save('ZFDATA_ORG','RECONIN');
```

Published with MATLAB® 7.13

Iterative reconstruction starts here.

```
clear all;

disp('Iterative recon starting');
loadZFDATA1;
x0 = RECONIN.x0; % Initial estimate for recon (zfwdc)
y = RECONIN.y;
PARAM = RECONIN.PARAM;
TVw=0.5e-3;%recon params
clearRECONIN;
figure;
tic;
for k=1:2
disp(k);
disp('--------------------');
x0 =(ncg2_hz(x0,y,TVw,PARAM));
end
toc;
cleary;
clearTVw;
clearPARAM;
loadZFDATA1;
RECONIN.x0=x0;
save('ZFDATA1.mat','RECONIN'); % Save final recon variable x0 as part of RECONIN
```

Published with MATLAB® 7.13

A.4SOURCES AND LIBRARIES

Code for generating the undersampling mask and the non-linear conjugate gradient have been re-written, modified and adapted to the specific application,based on Dr. Michael Lustig's Sparse MRI V0.2 open source code (92). The Matlab executable code (mex-files) for gridding and regridding employed in the SWIFT application has been shared by Dr. Steen Moeller, University of Minnesota and has been demonstrated previously (87). The remainder of the code has been developed by utilizing the signal processing, image processing and wavelet toolboxes in Matlab, The Mathworks Inc., MA.

APPENDIX B

WAVELET ANALYSES

Wavelets were used for transform sparsity in the CS MRSI and CS DCE-MRI projects. This was accomplished using the functions provided by the *Wavelet toolbox* in Matlab, The Mathworks Inc., MA.

B.1 CS MRSI

The MRSI spectra are sparse in the wavelet domain. The wavelet decomposition for the complex MRSI data was performed by obtaining the 2Dfourth level decompositions for each of the real and imaginary components separately using the multi-level 2D wavelet decomposition function '*wavedec2*'. The 2 dimensions included the spectral dimension and a spatial dimension. This analysis was repeated over the third dimension of space. The wavelet used for the analysis was the Daubechies-4 orthogonal wavelet. The resulting wavelet coefficients were treated as part of a single 3D variable (say *W*) composed of the real and imaginary wavelet coefficients of the corresponding components of the 3D data.

The sparsity constraint was evaluated by employing the definition in equation [B.1.1]. This definition was followed to ensure smoothness of the L_1function (described by ψ in[2.3])as the function of sum of the absolute values is not a smooth function and is not well defined for all values of m. The value (α) for the smoothness factor in all the implementations is 1 x10^{-15}. This definition aids in evaluating the gradient required by the non-linear conjugate gradient algorithm.

$$|W| = \sqrt{WW^* + \alpha} \quad [\text{B. 1.1}]$$

The reconstruction of these wavelet coefficients was performed using the 2D multi-level synthesis *'waverec2'* function with the respective real and imaginary reconstructions corresponding to the real and imaginary components of the MRSI spectra. The inputs to this function were the wavelet coefficients *W* calculated by '*wavedec2'* and the details of the level of decomposition (i.e. fourth level) and wavelet family (Daubechies).

B.2 CS DCE-MRI

The DCE-MRI images acquired post-contrast are sparse with respect to the baseline image (or the reference image). The difference image between an image after the injection and the reference image can then be further sparsified by the use of wavelets. In this case, the function *'wavedec2'*was used to decompose the 2D difference image at temporal point *t.* The decomposition was again performed separately on the real and imaginary channels as in the MRSI case. The parameters for the decomposition were the same as used for the MRSI case in terms of the level and the wavelet family used. The resulting wavelet coefficients were stored as a single 3D variable used later for reconstruction of the complex image data as in the MRSI case. The sparsity constraint was evaluated as per equation [B.1.2]. The reconstruction was performed using the *'waverec2'* function with identical parameters from the MRSI case.

APPENDIX C

LIST OF PUBLICATIONS AND CONFERENCE ABSTRACTS

Publications

1. **Geethanath, S**, Baek, H, Ganji, SK, Ding, Y, Maher, EA, Sims, RD, Choi, C, Lewis, MA, Kodibagkar, VD, "Compressive sensing could accelerate ^{1}H MR metabolic imaging in the clinic" (Radiology, in press)

2. **Geethanath, S**, Baek, H, Kodibagkar, VD, "Retrospective analysis of application of compressive sensing to ^{1}H MR metabolic imaging of the human brain", SPIE Medical Imaging, 7626; 2010. p 76260G-76211

Papers in preparation

1. **Geethanath, S**, Gulaka, PK, Kodibagkar, VD, "Acceleration of conventional data acquisition in dynamic contrast enhancement: comparing keyhole approaches with compressive sensing" (Magnetic Resonance Engineering, submitted)

2. Menon, JU, Gulaka, PK, McKay, MA, **Geethanath, S**, Kodibagkar, VD, "Dual-modality, dual-functional nanoemulsions for cellular and molecular imaging" (Nanotechnology, in preparation)

Conference abstracts

1. Menon, JU, Gulaka, PK, Darjazanie, T, **Geethanath, S**, Kodibagkar, VD, "Dual-modality, dual-functional nanoemulsions for cellular and molecular imaging", BMES Annual Meeting, Hartford, Connecticut, October 2011

2. **Geethanath, S**, Baek, H, Ganji, SK, Ding, Y, Choi, C, Sims, RD, Lewis, MA, Kodibagkar, VD, "Fast ^{1}H MR metabolic imaging of cancer", ISMRM Annual Meeting, Montreal, Canada, May 2011 *(Oral presentation)*

3. **Geethanath, S**, Gulaka, PK, Kodibagkar, VD, “A comparative study of keyhole and compressed sensing based approaches to accelerate DCE MRI”, ISMRM Annual Meeting, Montreal, Canada, May 2011

4. **Geethanath, S**, Moeller, S, Corum, C, Lewis, MA, Kodibagkar, VD, “A swifter SWIFT using compressed sensing”, ISMRM Annual Meeting, Montreal, Canada, May 2011

5. **Geethanath, S**, Baek, H, Ganji, SK, Ding. Y, Choi, C, Sims, RD, Kodibagkar, VD, “Application of compressed sensing for rapid MR metabolic imaging” Gordon conference on in vivo magnetic resonance, Andover, NH, July 2010

6. Rastogi, U, **Geethanath, S**, Kodibagkar, VD , “Spectral spatial pulses for quantitative ^{1}H MR tissue oximetry” Gordon conference on in vivo magnetic resonance, Andover, NH, July 2010

7. **Geethanath, S**, Baek, H, Kodibagkar, VD, “Accelerated H Chemical Shift Imaging of the brain using compressive sensing”, ISMRM Annual Meeting, Stockholm, Sweden, May 2010 *(Oral presentation)*

8. **Geethanath, S**, Baek, H, Kodibagkar, VD, “Retrospective analysis of application of compressive sensing to ^{1}H MR metabolic imaging of the human brain”, SPIE Medical Imaging, San Diego, February, 2011 *(Oral presentation)*

REFERENCES

1. Matt A. Bernstein KFK, and Xiaohong Joe Zhou. Handbook of MRI pulse sequences: Elsevier; 2004.

2. Bloch F. Nuclear Induction. Physical Review 1946;70(7-8):460.

3. Gold GE, Han E, Stainsby J, Wright G, Brittain J, Beaulieu C. Musculoskeletal MRI at 3.0 T: Relaxation Times and Image Contrast. American Journal of Roentgenology 2004;183(2):343-351.

4. Tsai C-M, Nishimura DG. Reduced aliasing artifacts using variable-density k-space sampling trajectories. Magnetic Resonance in Medicine 2000;43(3):452-458.

5. Wajer FTAW. Non-Cartesian MRI scan time reduction through sparse sampling: Ponsen & Looijen; 2001.

6. Irarrazabal P, Nishimura DG. Fast Three Dimensional Magnetic Resonance Imaging. Magnetic Resonance in Medicine 1995;33(5):656-662.

7. Kumar A, Welti D, Ernst RR. NMR Fourier zeugmatography. Journal of Magnetic Resonance (1969) 1975;18(1):69-83.

8. Jackson JI, Meyer CH, Nishimura DG, Macovski A. Selection of a Convolution Function for Fourier Inversion Using Gridding. Ieee T Med Imaging 1991;10(3):473-478.

9. Pipe JG, Menon P. Sampling density compensation in MRI: Rationale and an iterative numerical solution. Magnetic Resonance in Medicine 1999;41(1):179-186.

10. Sarty GE, Bennett R, Cox RW. Direct reconstruction of non-Cartesian k-space data using a nonuniform fast Fourier transform. Magnetic Resonance in Medicine 2001;45(5):908-915.

11. Block KT, Uecker M, Frahm J. Undersampled radial MRI with multiple coils. Iterative image reconstruction using a total variation constraint. Magnetic Resonance in Medicine 2007;57(6):1086-1098.

12. Haacke EM, Lindskogj ED, Lin W. A fast, iterative, partial-fourier technique capable of local phase recovery. Journal of Magnetic Resonance (1969) 1991;92(1):126-145.

13. Sutton BP, Noll DC, Fessler JA. Fast, iterative image reconstruction for MRI in the presence of field inhomogeneities. Medical Imaging, IEEE Transactions on 2003;22(2):178-188.

14. Pruessmann KP, Weiger M, Scheidegger MB, Boesiger P. SENSE: Sensitivity encoding for fast MRI. Magnetic Resonance in Medicine 1999;42(5):952-962.

15. Candes EJ, Romberg J, Tao T. Robust uncertainty principles: Exact signal reconstruction from highly incomplete frequency information. Ieee T Inform Theory 2006;52(2):489-509.

16. Lustig M, Donoho D, Pauly JM. Sparse MRI: The application of compressed sensing for rapid MR imaging. Magnetic Resonance in Medicine 2007;58(6):1182-1195.

17. Vasanawala SS, Alley MT, Hargreaves BA, Barth RA, Pauly JM, Lustig M. Improved Pediatric MR Imaging with Compressed Sensing1. Radiology 2010;256(2):607-616.

18. Candès E, Wakin M, Boyd S. Enhancing Sparsity by Reweighted l_1 Minimization. Journal of Fourier Analysis and Applications 2008;14(5):877-905.

19. Trzasko J, Manduca A. Highly Undersampled Magnetic Resonance Image Reconstruction via l_0 Homotopic Minimization. Medical Imaging, IEEE Transactions on 2009;28(1):106-121.

20. Chartrand R. Fast algorithms for nonconvex compressive sensing: MRI reconstruction from very few data. 2009 June 28 2009-July 1 2009. p 262-265.

21. Lustig M, Donoho DL, Santos JM, Pauly JM. Compressed sensing MRI. Ieee Signal Proc Mag 2008;25(2):72-82.

22. Daly PF, Cohen JS. Magnetic resonance spectroscopy of tumors and potential in vivo clinical applications: a review. Cancer Res 1989;49(4):770-779.

23. Gillies RJ, Bhujwalla ZM, Evelhoch J, Garwood M, Neeman M, Robinson SP, Sotak CH, Van Der Sanden B. Applications of magnetic resonance in model systems: tumor biology and physiology. Neoplasia 2000;2(1-2):139-151.

24. Pirzkall A, Li XJ, Oh JM, Chang S, Berger MS, Larson DA, Verhey LJ, Dillon WP, Nelson SJ. 3D MRSI for resected high-grade gliomas before RT: Tumor extent according to metabolic activity in relation to MRI. International Journal of Radiation Oncology Biology Physics 2004;59(1):126-137.

25. Kurhanewicz J, Vigneron DB, Nelson SJ. Three-dimensional magnetic resonance spectroscopic imaging of brain and prostate cancer. Neoplasia 2000;2(1-2):166-189.

26. Nelson SJ, Vigneron DB, Dillon WP. Serial evaluation of patients with brain tumors using volume MRI and 3D 1H MRSI. Nmr Biomed 1999;12(3):123-138.

27. Nelson SJ. Multivoxel magnetic resonance spectroscopy of brain tumors. Mol Cancer Ther 2003;2(5):497-507.

28. Howe FA, Opstad KS. H-1 MR spectroscopy of brain tumours and masses. Nmr Biomed 2003;16(3):123-131.

29. Bottomley PA. Spatial Localization in NMR Spectroscopy in Vivo. Annals of the New York Academy of Sciences 1987;508(1):333-348.

30. Ebel A, Soher BJ, Maudsley AA. Assessment of 3D proton MR echo-planar spectroscopic imaging using automated spectral analysis. Magnetic Resonance in Medicine 2001;46(6):1072-1078.

31. Zhu H, Barker PB. MR spectroscopy and spectroscopic imaging of the brain. Methods Molecular Biology 2011;711:203-226.

32. Mcgibney G, Smith MR, Nichols ST, Crawley A. Quantitative-Evaluation of Several Partial Fourier Reconstruction Algorithms Used in Mri. Magnetic Resonance in Medicine 1993;30(1):51-59.

33. Tsai CM, Nishimura DG. Reduced aliasing artifacts using variable-density k-space sampling trajectories. Magnetic Resonance in Medicine 2000;43(3):452-458.

34. Pohmann R, von Kienlin M, Haase A. Theoretical evaluation and comparison of fast chemical shift imaging methods. J Magn Reson 1997;129(2):145-160.

35. Zierhut ML, Ozturk-Isik E, Chen AP, Park I, Vigneron DB, Nelson SJ. (1)H Spectroscopic Imaging of Human Brain at 3 Tesla: Comparison of Fast Three-Dimensional Magnetic Resonance Spectroscopic Imaging Techniques. J Magn Reson Imaging 2009;30(3):473-480.

36. Posse S, Decarli C, Lebihan D. 3-Dimensional Echo-Planar Mr Spectroscopic Imaging at Short Echo Times in the Human Brain. Radiology 1994;192(3):733-738.

37. Mansfield P. Spatial-Mapping of the Chemical-Shift in Nmr. Magnetic Resonance in Medicine 1984;1(3):370-386.

38. Mulkern RV, Panych LP. Echo planar spectroscopic imaging. Concepts in Magnetic Resonance 2001;13(4):213-237.

39. Du W, Du YP, Fan X, Zamora MA, Karczmar GS. Reduction of spectral ghost artifacts in high-resolution echo-planar spectroscopic imaging of water and fat resonances. Magnetic resonance in Medicine 2003;49(6):1113-1120.

40. Serrai H, Senhadji L, de Certaines JD, Coatrieux JL. Time-Domain Quantification of Amplitude, Chemical Shift, Apparent Relaxation TimeT*2, and Phase by Wavelet-Transform Analysis. Application to Biomedical Magnetic Resonance Spectroscopy. Journal of Magnetic Resonance 1997;124(1):20-34.

41. Serrai H, Nadal-Desbarats L, Poptani H, Glickson JD, Senhadji L. Lactate editing and lipid suppression by continuous wavelet transform analysis: Application to simulated and 1H MRS brain tumor time-domain data. Magnetic Resonance in Medicine 2000;43(5):649-656.

42. Cancino-De-Greiff HF, Ramos-Garcia R, Lorenzo-Ginori JV. Signal de-noising in magnetic resonance spectroscopy using wavelet transforms. Concepts in Magnetic Resonance 2002;14(6):388-401.

43. Zarei S, Alireazie J, Babyn P, Kassner A, Widjaja E. MRS Feature Extraction: Time-Frequency and Wavelet Analysis. 2008 16-18 May 2008. p 1863-1866.

44. Fu Y, Serrai H. Fast magnetic resonance spectroscopic imaging (MRSI) using wavelet encoding and parallel imaging: In vitro results. Journal of Magnetic Resonance 2011;211(1):45-51.

45. Hu S, Lustig M, Chen AP, Crane J, Kerr A, Kelley DA, Hurd R, Kurhanewicz J, Nelson SJ, Pauly JM, Vigneron DB. Compressed sensing for resolution enhancement of hyperpolarized 13C flyback 3D-MRSI. J Magn Reson 2008;192(2):258-264.

46. Doneva M, Bornert P, Eggers H, Stehning C, Senegas J, Mertins A. Compressed sensing reconstruction for magnetic resonance parameter mapping. Magn Reson Med 2010.

47. Hu S, Lustig M, Chen AP, Crane J, Kerr A, Kelley DAC, Hurd R, Kurhanewicz J, Nelson SJ, Pauly JM, Vigneron DB. Compressed sensing for resolution enhancement of hyperpolarized 13C flyback 3D-MRSI. Journal of Magnetic Resonance 2008;192(2):258-264.

48. Schirmer T, Auer DP. On the reliability of quantitative clinical magnetic resonance spectroscopy of the human brain. Nmr Biomed 2000;13(1):28-36.

49. Geethanath S, Baek H, Kodibagkar VD. Retrospective analysis of application of compressive sensing to 1H MR metabolic imaging of the human brain. In: Robert CM, John BW, editors; 2010. SPIE. p 76260G.

50. Naressi A, Couturier C, Castang I, de Beer R, Graveron-Demilly D. Java-based graphical user interface for MRUI, a software package for quantitation of in vivo/medical magnetic resonance spectroscopy signals. Computers in Biology and Medicine 2001;31(4):269-286.

51. Ratiney H, Coenradie Y, Cavassila S, van Ormondt D, Graveron-Demilly D. Time-domain quantitation of 1H short echo-time signals: background accommodation. MAGMA 2004;16(6):284-296.

52. Choi C, Ganji SK, Deberardinis RJ, Dimitrov IE, Pascual JM, Bachoo R, Mickey BE, Malloy CR, Maher EA. Measurement of glycine in the human brain in vivo by (1) H-MRS at 3 T: application in brain tumors. Magn Reson Med 2011;Epub, doi: 10.1002/mrm.22857.

53. Hylton N. Dynamic contrast-enhanced magnetic resonance imaging as an imaging biomarker. J Clin Oncol 2006;24(20):3293-3298.

54. Knopp MV, Weiss E, Sinn HP, Mattern J, Junkermann H, Radeleff J, Magener A, Brix G, Delorme S, Zuna I, van Kaick G. Pathophysiologic basis of contrast enhancement in breast tumors. J Magn Reson Imaging 1999;10(3):260-266.

55. Port RE, Knopp MV, Hoffmann U, Milker-Zabel S, Brix G. Multicompartment analysis of gadolinium chelate kinetics: Blood-tissue exchange in mammary tumors as monitored by dynamic MR imaging. Jmri-Journal of Magnetic Resonance Imaging 1999;10(3):233-241.

56. Taylor JS, Tofts PS, Port R, Evelhoch JL, Knopp M, Reddick WE, Runge VM, Mayr N. MR imaging of tumor microcirculation: Promise for the new millenium. Jmri-J Magn Reson Im 1999;10(6):903-907.

57. Nunes LW, Schnall MD, Siegelman ES, Langlotz CP, Orel SG, Sullivan D, Muenz LA, Reynolds CA, Torosian MH. Diagnostic performance characteristics of architectural features revealed by high spatial-resolution MR imaging of the breast. Am J Roentgenol 1997;169(2):409-415.

58. Endrich B, Reinhold HS, Gross JF, Intaglietta M. Tissue Perfusion Inhomogeneity during Early Tumor-Growth in Rats. Journal of the National Cancer Institute 1979;62(2):387-395.

59. Sodickson DK, Manning WJ. Simultaneous acquisition of spatial harmonics (SMASH): Fast imaging with radiofrequency coil arrays. Magnetic Resonance in Medicine 1997;38(4):591-603.

60. Heidemann RM, Ozsarlak O, Parizel PM, Michiels J, Kiefer B, Jellus V, Muller M, Breuer F, Blaimer M, Griswold MA, Jakob PM. A brief review of parallel magnetic resonance imaging. Eur Radiol 2003;13(10):2323-2337.

61. Tsao J, Boesiger P, Pruessmann KP. k-t BLAST and k-t SENSE: Dynamic MRI with high frame rate exploiting spatiotemporal correlations. Magnetic Reson Med 2003;50(5):1031-1042.

62. Jung H, Sung K, Nayak KS, Kim EY, Ye JC. k-t FOCUSS: A General Compressed Sensing Framework for High Resolution Dynamic MRI. Magnet Reson Med 2009;61(1):103-116.

63. Gamper U, Boesiger P, Kozerke S. Compressed sensing in dynamic MRI. Magnet Reson Med 2008;59(2):365-373.

64. Vanvaals JJ, Brummer ME, Dixon WT, Tuithof HH, Engels H, Nelson RC, Gerety BM, Chezmar JL, Denboer JA. Keyhole Method for Accelerating Imaging of Contrast Agent Uptake. Jmri-J Magn Reson Im 1993;3(4):671-675.

65. Chen ZL, Zhang JX, Pang KK. Adaptive keyhole methods for dynamic magnetic resonance image reconstruction. Comput Med Imag Grap 2007;31(6):458-468.

66. Murase K. Efficient method for calculating kinetic parameters using T-1-weighted dynamic contrast-enhanced magnetic resonance imaging. Magnetic Resonance in Medicine 2004;51(4):858-862.

67. Hoge WS, Miller EL, Lev-Ari H, Brooks DH, Karl WC, Panych LP. An efficient region of interest acquisition method for dynamic magnetic resonance imaging. Ieee Transactions on Image Processing 2001;10(7):1118-1128.

68. Liang ZP, Lauterbur PC. An Efficient Method for Dynamic Magnetic-Resonance-Imaging. Ieee Transactions on Medical Imaging 1994;13(4):677-686.

69. Webb AG, Liang ZP, Magin RL, Lauterbur PC. Applications of Reduced-Encoding Mr-Imaging with Generalized-Series Reconstruction (Rigr). Jmri-Journal of Magnetic Resonance Imaging 1993;3(6):925-928.

70. Ji J, Lang T. Dynamic MRI with Compressed Sensing imaging using temporal correlations. I S Biomed Imaging 2008:1613-1616.

71. Wang H, Miao Y, Zhou K, Yu Y, Bao S, He Q, Dai Y, Xuan SY, Tarabishy B, Ye Y, Hu J. Feasibility of high temporal resolution breast DCE-MRI using compressed sensing theory. Med Phys 2010;37(9):4971-4981.

72. Jung H, Sung K, Nayak KS, Kim EY, Ye JC. k-t FOCUSS: a general compressed sensing framework for high resolution dynamic MRI. Magn Reson Med 2009;61(1):103-116.

73. Yankeelov TE, Luci JJ, Lepage M, Li R, Debusk L, Lin PC, Price RR, Gore JC. Quantitative pharmacokinetic analysis of DCE-MRI data without an arterial input function: a reference region model. Magn Reson Imaging 2005;23(4):519-529.

74. Smith DS, Welch EB, Li X, Arlinghaus LR, Loveless ME, Koyama T, Gore JC, Yankeelov TE. Quantitative effects of using compressed sensing in dynamic contrast enhanced MRI. Phys Med Biol 2011;56(15):4933-4946.

75. van Vaals JJ, Brummer ME, Dixon WT, Tuithof HH, Engels H, Nelson RC, Gerety BM, Chezmar JL, den Boer JA. "Keyhole" method for accelerating imaging of contrast agent uptake. J Magn Reson Imaging 1993;3(4):671-675.

76. Chen Z, Zhang J, Pang KK. Adaptive keyhole methods for dynamic magnetic resonance image reconstruction. Comput Med Imaging Graph 2007;31(6):458-468.

77. Seeger M, Nickisch H, Pohmann R, Scholkopf B. Optimization of k-space trajectories for compressed sensing by Bayesian experimental design. Magn Reson Med 2010;63(1):116-126.

78. Pruessmann KP, Weiger M, Scheidegger MB, Boesiger P. SENSE: sensitivity encoding for fast MRI. Magn Reson Med 1999;42(5):952-962.

79. Sodickson DK, Manning WJ. Simultaneous acquisition of spatial harmonics (SMASH): fast imaging with radiofrequency coil arrays. Magn Reson Med 1997;38(4):591-603.

80. Griswold MA, Jakob PM, Heidemann RM, Nittka M, Jellus V, Wang J, Kiefer B, Haase A. Generalized autocalibrating partially parallel acquisitions (GRAPPA). Magn Reson Med 2002;47(6):1202-1210.

81. Geethanath S, Gulaka PK, Kodibagkar VD. A comparative study of undersampling schemes for magnetic resonance dynamic contrast enhanced imaging. 2011; Montreal, Canada. p 2630.

82. Smith DS, Li X, Arlinghaus L, Welch EB, Gore JC, Yankeelov TE. Improved Temporal Resolution for Human Breast DCE-MRI Data Using Compressed Sensing. 2011; Montreal, Canada. p 3117.

83. Idiyatullin D, Corum C, Park J-Y, Garwood M. Fast and quiet MRI using a swept radiofrequency. J Magn Reson 2006;181(2):342-349.

84. Purcell EM, Torrey HC, Pound RV. Resonance Absorption by Nuclear Magnetic Moments in a Solid. Physical Review 1946;69(1-2):37-38.

85. Ziessow D, Lipsky SR. Nuclear magnetic resonance Fourier spectroscopy with pulse and stochastic excitation controlled by an IBM 1800 computer. J Phys E 1972;5(5):437-441.

86. Bloch F, Hansen WW, Packard M. The Nuclear Induction Experiment. Physical Review 1946;70(7-8):474-485.

87. Park J-Y, Moeller S, Goerke U, Auerbach E, Chamberlain R, Ellermann J, Garwood M. Short echo-time 3D radial gradient-echo MRI using concurrent dephasing and excitation. Magnetic Resonance in Medicine 2011.

88. Sheehan FT, Zajac FE, Drace JE. Using cine phase contrast magnetic resonance imaging to non-invasively study in vivo knee dynamics. Journal of Biomechanics 1997;31(1):21-26.

89. C. A. Corum SM, D. Idiyatullin, D. Hutter, A. Snyder, M. T. Nelson, T. Emory, J. E. Kuehn-Hajder, L. E. Eberly, G. Adriany, and M. Garwood. Breast Morphological and DCE MRI with SWIFT. 2011; Montreal, Canada.

90. Idiyatullin D, Corum C, Moeller S, Garwood M. Gapped pulses for frequency-swept MRI. J Magn Reson 2008;193(2):267-273.

91. Zhao D, Jiang L, Hahn EW, Mason RP. Tumor physiologic response to combretastatin A4 phosphate assessed by MRI. International Journal of Radiation Oncology 2005;62(3):872-880.

92. Lustig M,http://www.eecs.berkeley.edu/~mlustig/software/sparseMRI_v0.2.tar.gz

BIOGRAPHICAL INFORMATION

Sairam Geethanath graduated with a Master of Science degree in Electrical Engineering from Illinois Institute of Technology, Chicago in 2007 with specialization in biomedical imaging and signals during which time he also interned at Siemens Medical Solutions, Chicago in the department of X-ray and Angiography (2006 – 2007). He then went on to work full-time for the same company as a software engineer (2007 – 2008) before joining the joint program in biomedical engineering at University of Texas at Arlington/University of Texas Southwestern Medical Center to pursue his doctoral studies. He joined Dr. Vikram D. Kodibagkar's magnetic resonance laboratory to explore the field of MRI technology development focusing on acceleration of MRI acquisitions. His doctoral research demonstrated three novel applications of compressed sensing to magnetic resonance spectroscopy and magnetic resonance imaging to accelerate MRI acquisitions. His career interests are in inventing novel biomedical-imaging technologies to enhance information content and make an impact on basic science and clinical research.